Growth and characterization of perovskite oxide ferroelectric thin films and its applications

Thesis submitted to

COCHIN UNIVERSITY OF SCIENCE AND TECHNOLOGY

in partial fulfillment of the requirements

for the award of the degree of

DOCTOR OF PHILOSOPHY

RESHMI.R

Department of Physics
Cochin University of Science and Technology
Cochin - 682 022, Kerala, India

August 2010

Growth and characterization of perovskite oxide ferroelectric thin films and its applications

Ph.D. thesis in the field of Materials Science

Author:
Reshmi.R
Optoelectronic Devices Laboratory
Department of Physics
Cochin University of Science and Technology
Cochin - 682 022, Kerala, India.
Email: rreshmi@gmail.com

Supervisor:
Dr. M.K. Jayaraj
Associate Professor
Optoelectronic Device Laboratory
Department of Physics
Cochin University of Science and Technology
Cochin 682 022, Kerala, India.
Email: mkj@cusat.ac.in

Front cover: Heterostructure of LSCO/BST/LSCO
Back cover: Flexible ferroelectric memory

August 2010

Dr. M. K. Jayaraj
Associate Professor
Department of Physics
Cochin University of Science and Technology
Cochin 682 022, India.

5^{th} August 2010

Certificate

Certified that the work presented in this thesis entitled "Growth and characterization of perovskite oxide ferroelectric thin films and its applications"is based on the authentic record of research carried out by Reshmi.R under my guidance in the Department of Physics, Cochin University of Science and Technology, Cochin 682 022 and has not been included in any other thesis submitted for the award of any degree.

Dr. M. K. Jayaraj
(Supervising Guide)

Phone : +91 484 2577404 extn 33 Fax: 91 484 2577595 Email: mkj@cusat.ac.in

Declaration

Certified that the work presented in this thesis entitled "Growth and characterization of perovskite oxide ferroelectric thin films and its applications"is based on the original research work done by me under the supervision and guidance of Dr. M. K. Jayaraj, Associate Professor, Department of Physics, Cochin University of Science and Technology, Cochin-682 022 and has not been included in any other thesis submitted previously for the award of any degree.

Reshmi.R

Cochin-22
5^{th} August 2010

.

Kindred Spirits,
I promise that I shan't forget,
this sliver in time
your souls that I've met

.

Guru Brahma; Guru Vishnu
Guru devo Maheshwara
Guru Sakshath Parabhrama
Thasmai Shree Guravae namaha

[*Guru is indeed the Creator in the form Lord Brahma ; Sustainer as Lord Vishnu and Destroyer as Lord Shiva; He is the limitless Brahman; I salute to such a Guru!*]

Acknowledgments

This thesis is a part of years of experience and different person associated with this venture deserve special mention. It is with pleasure i record the acknowledgment to convey my deep sense gratitude for each and every one.

I would like to express my overwhelming gratitude to my research guide, Dr. M. K. Jayaraj, for his expertise shown in guiding my work and the willingness to share his knowledge and experience. He has given immense freedom for us in developing ideas and he is always willing to hear and acknowledge sincere efforts. I am indebted to him for making it possible for me to work in diverse fields in the lab. He has given me ample opportunity to collaborate and work with different institutes. I especially thank him for his prompt reading and careful analysis of my thesis. I am sure i will be benefited with the expertise and knowledge I gained working with Jayaraj sir.

I express my sincere thanks to Prof. M.R.Anantharaman, Head, Department of Physics and all the former Heads of the Department - Prof. V. C. Kuriakose, Prof. Ramesh Babu Thayyullathil , Prof. Godfrey Louis- for permitting me to use the research facilities in the Department. I would like to thank my doctoral committee member Prof. K. P. Vijayakumar and all the other teachers in Department of Physics. I gratefully acknowledge the help and inspiration from Jayalekshmi teacher who have inspired me both in academic and personal development. I take this opportunity to extend a special thanks to Hheinz-Christoph Neitzert, University of Salerno,Italy for all his advice and help

I gratefully acknowledge the supports and helps received from Dr V.Natarjan, NPOL, Dr.M.T.Sebastian, NIIST and Dr. Kumar of C-MET, during my research period. I extend my thanks to Dr. Sripathi and Dr Ganeshan of IUC-DAE Indore for permitting me to take the XPS and AFM measurements. I would like to extend my thanks to V.R.Palkar and her team at TIFR for ferroelectric measurements. Thanks to Gurulinga at IISc for SEM measurements.

I am thankful to all the office and library staff of the Department of Physics and the technical staff at USIC for all the help and cooperation.

I thank Kerala State Council for Science Technology and Environment, Kerala; Naval Physical Oceanographic Laboratory, Thrikkakra and Department of Science and Technology; Government of India for financially supporting me during this endeavor. I acknowledge the financial support of ESF - European Science Foundation - to attend the international conference during the period of my research work.

It is my pleasure to acknowledge the advice and love received from my senior researchers in the lab Aldrin, Nisha and Rahana. They have shown utmost love and care in both my personal and academic matters. I would like to express my sincere appreciation to my colleagues in the Optoelectronic Devices Laboratory Ajimsha, Anoop, Saji, Mini, Anila teacher and Joshy sir for all the help they had extended. We had valuable research discussions and enjoyed parties and entertainment. I find immensely enjoyable working with my dear friends - Arun, Krishnaprasad, Sanal, Sasank, Vikas and Sathish bai. The discussions, experiments, driving classes, late night movies, parties, milk shakes have all bonded us as life time friends. My heartfelt thanks to Sreeja and Subha for the help, care and love they have showered on me. I express my regards to Rakhy, Hasna, James sir

and Saritha. I would like to acknowledge my heartfelt thanks to my friends Ratheesh and Pradeep for accompanying me to take measurements.

I take this occasion to thank Asha for the friendship and discussions we had . I would also like to thank her for the preparations of samples she had given me for ferroelectric studies. No words can replace my indebted gratitude to my dear friend Aneesh for his selfless support and ever encouraging words. He is indeed a kindred soul always lending a helping hand for all my ventures. I would like to express my deep rooted love and affection to Vanaja madam who i find a kindred soul. She was always there, lending an ear for me when i need the most. A word of love for my lil friends Anooja and Anjala for the special bond we shared.

I treasure my friendship with Prince sir, Sukesh, Vinitha, Ragitha, Anlin, Sanjay, Anuraj, Sarathlal, Manu, Jafer, Saritha, Jem, Christie, Jijin, Najla, Jobina, Shitha and Shonima, Shijeesh, Aebey, Vasudevan and Jerrin whom I got acquainted with at OED.

I remember with gratitude the support and good will extended to me by my friends Jayakrishnan, Deepa, Vijutha, Gopi, Baiju, Shaji; Chitra, Sini and Jisha.

I record my deep and utmost gratitude to my achan and amma their love and care during the entire period of my research work. I would like to thank ammamman Gokulan, Rajan, Chitrabhanu and my ammayi Malammayi, Geethammayi and Rajiamma for their enduring support and encouragement. I would like to thank my brothers Appu, Santhosh, Dileep, Anoop, Sarath, Dinesh and Siddu for the love and care. I remember my in laws especially Manju for their constant encouragement and love in this endeavor.

To Manoj for his imperishable support and tolerating my eccentricities

To Gichus for rising to the occasion and not bothering his mother

Finally I thank all my well wishers and friends who have supported me in this venture.
Above all, I thank God Almighty.

Reshmi.R

Contents

List of Figures

List of Tables

Preface

Oxide materials attract intensive studies and show potential for wide application since they cover a range of electrical property from insulator to high T_c semiconductors and from ferroelectric to ferromagnetic. Research on high T_c superconducting thin films has brought a rapid development of the fabricating technique of oxide films which have promoted the application of oxide thin films.

The drive towards miniaturization of electronic devices has motivated scientists to focus on ways to improve the properties of dielectric and ferroelectric oxide thin film. An ideal capacitor based on these ferroelectric oxides should have high dielectric constant, high dielectric break down field strength, low leakage current density and low dissipation factor. Apart from electronic application ferroelectric films are of interest to various micro electromechanical and optical applications. An important objective of research in dynamic random access memories (DRAM) technology is to miniaturize the memory cells and simultaneously increase the charge stored in the available area. To derive maximum storage efficiency the method is to increase the area of capacitor, reduce the thickness and use thin films

of high dielectric constant ferroelectric materials. The materials of interest in the present study for the development of memory devices are the ferroelectric $Ba_xSr_{(1-x)}TiO_3$ (BST) and $PbZr_{(1-x)}Ti_xO_3$ (PZT) for FeRAM applications.

With the development of ceramic processing and thin film technology, many new applications have emerged. The new available techniques to produce high quality thin films ferroelectrics are plasma sputtering, ion beam sputtering, metal organic vapour chemical deposition (MOCVD), sol-gel, spin coating metal organic decomposition (MOD) and pulsed laser deposition (PLD). With PLD epitaxial films can be deposited at low substrate temperature and high deposition rates over a range of target phases and composition with few experimental parameters to optimize.In the present work pulsed laser ablation and rf magnetron sputtering was employed for the deposition of ferroelectric films.

One of the problems with ferroelectric memories is the tendency to lose its ability to store data after a certain number of read/write cycles. This phenomena is called fatigue. The prime reason for the fatigue in ferroelectric thin films is the degradation of the ferroelectric/electrode interface. To reduce the degradation, a thin layer of conducting oxide is deposited between the metal electrode and ferroelectric thin film.Some of the oxides used for reducing the fatigue behavior of ferroelectric films are RuO_2, IrO_2, $SrRuO_3$, (La,Sr)COO_3 (LSCO) and $YBa_2Cu_3O_7$ (YBCO). The selected oxide electrode should have lattice parameters that match the substrate. Also the electrode should have a work function that is commensurate with the work function of the ferroelectric phase so that it acts as a sink for oxygen vacancies. Thereby the charge defect concentration at the ferroelectric/electrode interface can be controlled. In the present study the

effect of oxide electrode (La,Sr)COO_3 (LSCO) on the electrical properties of the ferroelectric materials is studied.

Chapter 1 gives an introduction to ferroelectricity and piezoelectricity. This includes orgin of ferroelectricity and piezoelectricity, ferroelectric domains and hysteresis loop.The oxygen octahedron of the general perovskite is described. The major class of oxide ferroelectric materials and their characteristics are discussed in detail. A brief introduction to the need for oxide electrodes is also discussed. A detailed description of memories using these ferroelectric oxides is also discussed. The literature review on the major class of oxides BST and PZT is also given towards the end of the chapter.

Chapter 2 describes in detail the thin film growth techniques and characterization tools employed in the present work. Thin film growth was accomplished using pulsed laser deposition (PLD) and sputtering techniques. The basic operation and specifications of all those characterisation tools are described in this chapter.

Chapter 3 describes the pulsed laser ablation of PZT/PLZT thin films. The objective of the study is to lower the deposition temperature of PZT for MEMS application. PZT and PLZT thin films were deposited by pulsed laser deposition on PtSi substrates with pure perovskite phase at a substrate temperature 600^0C . The Pb excess targets were used for compensating the Pb loss in PZT thin films. $PbTiO_3$ and ZnO buffer layers were deposited to lower the deposition temperature.Pervoskite phase was formed in all thin films at much lower temperature. ZnO buffer layer has lowered the deposition temperature to 300^0C. Stoichiometry is confirmed by composition analysis of the samples. The leakage current 200nA/cm^2 through the sample show good insulating nature.The variation of dielectric constant with voltage show butterfly loop for all the ferroelectric samples. The

switchable field is low (10kV/cm) for films deposited with oxide electrode LSCNO.

Chapter 4 describes the need of a Pb free material for ferroelectric application. The chapter describes the deposition of $Ba_{0.7}Sr_{0.3}TiO_3$ (BST) thin films by rf magnetron sputtering .The optical properties of barium strontium titanate (BST) thin films are important due to wide bandgap, high refractive index and low absorption coefficient and hence finds application in electro-optic devices and non-linear optical systems. BST thin films were deposited by RF magnetron sputtering on fused silica and $Si/SiO_2/TiO_2/Pt$(PtSi) substrates. The present study shows that there is an optimum value for oxygen to argon ratio for the growth of BST thin films. It is found that oxygen to argon ratio of 35/65 shows better structural and optical properties. XPS confirms that maximum oxygen content is for films grown under these optimised conditions. The band gap of the film under optimised condition is 3.51eV which is near bulk value. The refractive index (2.01) and packing density (0.85) was also maximum for films grown at this optimised conditions. Electrical charecterisation of the films were carried out by fabricating PtSi/BST/Au devices. The leakage current of the device showed a good insulating behavior. The variation of dielectric constant with voltage shows the tunable nature of the device. The low loss (0.04) and high figure of merit of tunable BST ferroelectric thin films suggests they can be used for microwave applications.

Chapter 5 describes the growth and charecterisation of BST thin films for gigabit memory applications by PLD. The films were deposited using both the third harmonics and fourth harmonics of Nd:YAG laser.The films deposited on substrates using 266nm were found to show better properties than those with 355nm. The electrical characterization of the device

Pt/BST/Au is studied and the conduction mechanism shows SCLC nature at intermediate fields. The polarization vs electric field plot shows ferroelectric nature. BST thin films deposited on LSCO/LSCNO, oxide pervoskite electrodes, were found to be crystalline without any post deposition heat treatment. Thus LSCO/LSCNO serve as a template as well as bottom electrode for the BST thin film capacitors. PtSi/LSCO/BST/LSCO devices showed little dispersion with frequency. The loss was found to be minimum (0.02) for films deposited on oxide template. The low leakage current (100nA/cm^2) shows that the films are suitable for gigabit memory device applications.The films showed ohmic nature at low field and a Pool Frenkel emission at high fields with an electron trapping energy of 1.3eV.The capacitance voltage characteristics shows high tunability with low dielectric loss. The ferroelectric phase is seen in the films at room temperature. The figure of merit for the structure is also high making BST thin films a promising material for frequency agile application.

Chapter 6 describes the pulsed laser deposition of Eu doped BST thin films. The main objective of the work is to study the possibility of rare earth doping into BST to find application in luminescence and nonlinear optics. Eu doped BST thin films were successfully deposited by pulsed laser ablation. The room temperature photoluminescence spectrum reveals the characteristic lines of rare earth Eu^{3+} in all the thin films. The photoluminescence spectrum showed the transitions of Eu^{3+} at 550nm ($^5D_1$ - $^7F_2$), 615nm ($^5D_0$ - $^7F_2$) and 669nm ($^5D_0$ - $^7F_3$) on excitation with 408nm. The nonlinear optical properties were investigated by a single beam Z-scan set up. The films show excellent nonlinear optical property. The nonlinear absorption coefficient and nonlinear refractive index is found to be 242 m/ GW and -1.508 x 10^{-6} m^2/GW at 532nm. The real and imaginary

part of third order susceptibility was found to be 2.58 x 10^{-17} m^2/V^2 and 1.16 x10^{-16} m^2/V^2 respectively. The large nonlinear optical absorption in BST:Eu thin films was attributed to local field and small grain size. The thin film shows good optical limiting property with a threshold input fluence of 125μJ. The films show a high dielectric constant of 600 at 1Khz.The ferroelectric properties of the PtSi/BST:Eu/Au structure exhibits butterfly loop with a coercive field of 25kV/cm. This indicated that the BST:Eu thin films can be used both for ferroelectric, luminescence application as well as for nonlinear optical limiting application. Chapter 7 summarizes the main results in the thesis and the scope for future works.

Part of the thesis has been published in the following internationally referred journals

1. Influence of oxygen to argon ratio on the structural optical and electrical properties of rf magnetron sputtered $Ba_{0.7}Sr_{0.3}TiO_3$ thin films **Reshmi, R**, M. K. Jayaraj, M.T.Sebastian (submitted to Journal of Electrochemical society)

2. High tunability of pulsed laser deposited $Ba_{0.7}Sr_{0.3}TiO_3$ thin films on perovskite oxide electrode**R. Reshmi**, A.S.Asha, P.S Krishnaprasad , M. K. Jayaraj, M.T.Sebastian (Accepted in Jr Alloys and Compounds)

3. Photoluminescence of Eu^{3+} doped $Ba_{0.7}Sr_{0.3}TiO_3$ thin film for optoelectronic application**R. Reshmi**,M. K.Jayaraj, K.Jithesh, M.T.Sebastian 157, H783 (2010)

4. Effect of buffer layers on the properties of laser ablated PZT thin films, **Reshmi.R,** V.Natarajan, M K Jayaraj (accepted in Integrated Ferroelectrics)

5. Linear and nonlinear optical properties of rare earth doped of BST thin films, **R. Reshmi**, R. Sreeja, M. K. Jayaraj, J. James and M. T. Sebastian, Applied Physics B: Lasers and Optics,96, 433 (2009)

Other publication to which author has contributed

1. Dependence of Size of Liquid Phase Pulsed Laser Ablated ZnO Nanoparticles on pH of the Medium, P.M. Aneesh, Arun Aravind, **R. Reshmi**, R. S. Ajimsha and M. K. Jayaraj, Transactions of Materials Research Society of Japan (In press)

2. Size dependent optical nonlinearity of Au nanocrystals, R. Sreeja, P.M. Aneesh, Arun Aravind, **R. Reshmi**, Reji Philip and M. K. Jayaraj, Journal of Electrochemical society, 156 (10), K167 (2009)

3. Polycrystalline coating of hydroxyapatite on TiAl6V4 implant material grown at lower substrate temperatures by hydrothermal annealing after pulsed laser deposition ,K. K. Saju, **R. Reshmi,** N. H. Jayadas, J. James, M. K. Jayaraj, *Proceedings of the Institution of Mechanical Engineers, Part H: Journal of Engineering in Medicine.* 223 (8), 1049 (2009)

4. Formation of hydroxyapatite coating on titanium at 200^0C through pulsed laser deposition followed by hydrothermal treatment. Manoj

Komath , P Rajesh , C.V Muraleedharan , H K Varma , R Reshmi and M.K Jayaraj (under review in MRS).

5. Determination of third-order optical absorptive nonlinearity of ZnO nanoparticles by Z-scan technique, R. Sreeja, R. Reshmi, Manu George and M. K. Jayaraj, *Proceedings of SPIE - The International Society for Optical Engineering* 7155, art. no. 715521 (2008)

6. Electrical and optical properties of $ZnGa_2O_4$ thin films deposited by pulsed laser deposition, K Mini Krishna, M.Nisha, **R Reshmi**, R Manoj, A.S.Asha,M.K.Jayaraj, Materials Forum 29 (2005) 243.

7. Pulsed laser deposition of $ZnGa_2O_4$ phosphor thin films, **R.Reshmi**, K.Minikrishna, R.Manoj, M.K. Jayaraj, Surface and Coating Technology,198 (2005) 345

Conference Presentations

1. Electrical studies of pulsed laser deposited BST thin films on Pt and LSCNO electrode. **Reshmi. R** Asha. A.S ,P.S.Krishnaprasad, M.K.Jayaraj, M.T.Sebastian, DAE-BRNS 5th National Symposium on Pulsed Laser Deposition of Thin Films and Nanostructured Materials (PLD 2009), Chennai, India

2. Ferroelectric Properties of BST and PZT Films Grown on a Novel LSCNO Electrode, **R. Reshmi**, A.S. Asha, M.T Sebastian, M.K.Jayaraj, IUMRS International Conference in Asia 2008 (IUMRS-ICA 2008), Nagoya, Japan

3. Laser assisted growth of Eu3+ doped $Ba_{0.7}Sr_{0.3}TiO_3$ thin film for optoelectronic and ferroelectric application. **R.Reshmi**, M.K.Jayaraj, M.T.Sebastian, National Conference on Pulsed Laser Deposition, held at Rajkot, 2007

4. Characterisation of pulsed laser deposited PZT and PLZT thin films on oxide pervoskite electrodes. **R.Reshmi** , M.K.Jayaraj, National Conference on Pulsed Laser Deposition, held at Rajkot,2007.

5. PLD and sputtering deposition of ferroelectric materials for memory applications (Invited talk) Salerno University, Salerno, Italy 2007

6. Effect of Oxygen Pressure on the Optical Properties of RF Sputtered BST Thin Films **Reshmi.R,** M.T.Sebastian, M.K.Jayaraj-NCSE-2006 Thrissur.

7. Synthesis of gold nanoparticles by laser ablation in liquid media, P. M. Aneesh, Arun Aravind, R. Sreeja, R. Reshmi and M. K. Jayaraj, Second International Conference on Frontiers in Nanoscience and Technology (*Cochin Nano* - 2009), Kochi, India

8. Gold nanoparticles by liquid phase pulsed laser ablation for biological and optical limiting applications, P. M. Aneesh, R.Sreeja, Arun Aravind, R. Reshmi and M. K. Jayaraj, 2nd International conference Bangalore Nano-08, Bangalore, India

9. Various nanostructures of ZnO grown by LP-PLA and chemical methods, P. M. Aneesh, Arun Aravind, R. Reshmi and .M. K. Jayaraj, 2nd International conference Bangalore Nano- 08, Bangalore, India

10. Size dependent optical absorptive nonlinearity of au nano clusters in water, P. M. Aneesh, R. Sreeja, Arun Aravind, R Reshmi, M. K. Jayaraj, Photonics 2008, Delhi, India

11. Optical Emission Spectroscopic Characterization Of Laser Ablated PZT Plasma Plume. S. Sasankakumar, N.V Joshy, R.Reshmi. M.K.Jayaraj. Conference on Laser Ablation 2007, Tenerife, Spain.

12. Optical absorption studies on $LiMn_2O_4$ films prepared by pulsed laser deposition. M. Rajive Tomy, R. Reshmi, K. Raveendranath, S. Jayalekshmi, M.K. Jayaraj. Conference on Laser Ablation 2007, Tenerife, Spain.

13. Growth of ZnO nanostructures by pulsed laser ablation, M. K. Jayaraj, R. S. Ajimsha, R. Reshmi, R. Sreeja, P. M. Aneesh, National Conference, Pondicherry University, Pondicherry, India (Invited Talk)

Chapter 1

Introduction to ferroelectrics

Hysteresis loops come in all sizes and shapes, and,
similar to a fingerprint identify the
material in a very special way
G.H Haertling

The phenomenon of ferroelectricity was discovered in 1921 by J. Valasek who was investigating the dielectric properties of Rochelle salt ($NaKC_4H_4O_6.4H_2O$). The name ferroelectricity refers to certain magnetic analogies, though it has no connection with iron (ferrum) at all. Ferroelectricity has also been called Seignette electricity, as Seignette or Rochelle Salt (RS) was the first material found to show ferroelectric properties such as a spontaneous polarization on cooling below the Curie point, ferroelectric domains and a ferroelectric hysteresis loop [1].

Oxide materials has wide range of applications since these oxides exhibit properties ranging from insulator to high T_c superconductors and from ferroelectric to ferromagnetics. Research on high T_c superconducting thin

films has brought a rapid development on the growth technique and have promoted the application of oxide thin films for device fabrication.

The potential for device application drove a tremendous volume of research beginning in the mid 1940's when $BaTiO_3$ was discovered to have a high dielectric constant (1000-3000) and possess the largest ferroelectric response then known to exist. Since then, many other ferroelectric ceramics including lead titanate ($PbTiO_3$), lead zirconate titanate (PZT), lead lanthanum zirconate titanate (PLZT), and relaxor ferroelectrics like lead magnesium niobate (PMN) have been developed and utilized for a variety of applications. But the interests diminished in 1960's and 1970's when industrial demands for the ease of processing and device durability dictated the use of alternate materials and approaches. Fatigue and aging associated with polycrystalline bulk materials were detrimental to many applications [2].

The development of ceramic processing and thin film technology lead to the emergence of new applications of ferroelectrics. A renewed interest in ferroelectric thin films has arisen with the new growth techniques like plasma sputtering, ion beam sputtering, metal organic vapour chemical deposition (MOCVD), sol-gel, spin coating, metal organic decomposition (MOD) and pulsed laser deposition (PLD) to produce high quality thin films of ferroelectrics. The PLD technique has matured rapidly with the discovery of high temperature superconducting oxides in 1986 [3]. These oxides have a perovskite based structure similar to many ferroelectric materials and have been deposited as epitaxial films by PLD. Epitaxial films can be deposited by PLD at low substrate temperature and high deposition rates over a range of target phases and composition with few experimental parameters to optimize.

The most promising application of ferroelectric ceramics have been in the areas such as dielectric ceramics for capacitors, ferroelectric thin films for non volatile memories, piezoelectric materials for medical ultrasound imaging and actuators, and electro-optic materials for data storage and displays. The potential commercial and defense related applications of thin ferroelectric film with thickness 0.2-5μm are widespread and include acoustic wave transducers [4, 5], electro optic switches [6] radiation hard, NVRAM [7] and pyrosensors [8]. Ferroelectrics have recently gained attention as potential smart materials and as active sensors in smart devices [9]. Ferroelectric composition mostly contain a volatile component (Pb,Bi,Li or K) and small deviations from stoichiometry can lead to films that comprise undesirable non ferroelectric phase. Control over the process is required to preclude loss of volatile components and formation of metastable phases [2].

1.1 Ferroelectric phase transition

A ferroelectric phase transition is a structural phase transition which results in the ability of the crystal to sustain a spontaneous polarization caused by the relative displacement of the ions of each unit cell of the crystal [1].

The ferroelectric phase transition occurs at a temperature T_c analogous to the curie temperature of a ferromagnet. Above the Curie temperature the crystal is usually a centrosymmetric paraelectric. Below the curie temperature the crystal is no longer centrosymmetric which results in ferroelectric behavior.

In the ferroelectric phase at least one set of ions in the crystal sits in a double well potential where either of the two positions is equally energiti-

cally favorable. Above T_c the particle in a double well have enough kinetic energy to move back and forth over the barrier that separates the wells so that the time average position of the atom is midway between the wells. Figure 1.1 shows the thermodynamic potential of the system as function of the atom position [9].

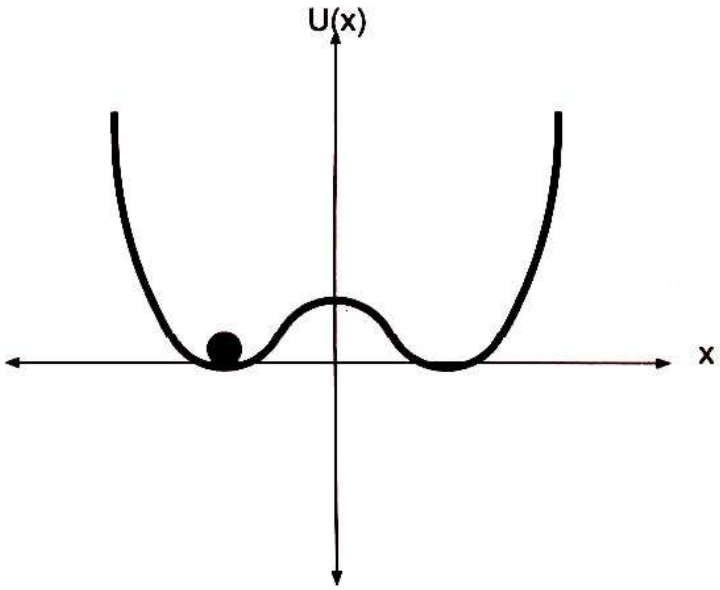

Figure 1.1: Thermodynamic potential as a function of atom position for a ferroelectric material below its curie temperature.

If the shape of the well stays the same above T_c but ion kinetic energy k_BT becomes large , the transition is an order disorder phase transition. If the minima of the well actually move together to form a singe well above T_c then the transition is displacive. These are the extrema of the phase transition phenomena most ferroelectric phase transition are combination

of displacive and order disorder transitions.

Ferroelectric phase transitions can be described mathematically with some success by Landau theory often called Landau-Devonshire theory as credit to Devonshire who developed it specifically for the ferroelectric case. Phase transitions in ferroelectric are usually second-order transitions meaning that the distortions of the crystal lattice occur continuously with temperature. When the transition are discontinuous (first-order) they are usually close to second- order transitions and are still described well by Landau-Devonshire theory.

In Landau-Devonshire theory the Helmhotz free energy of the system is described by a power seriers in the order parameter [1]. For a ferroelectric crystal the order parameter is the polarization, η where $0 \leq \eta \leq 1$

$$F(\eta, T, E) = A\eta^2 + B\eta^4 + C\eta^6 + D \tag{1.1}$$

where D is a constant. A has the form A_0(T-T_c) where T_c is the curie temperature. If the transition is first order there is hysteresis in the temperature dependence. This form for A is a result of mean field theory which is often used in ferromagnetism and analogously can be used in ferroelectrics as well. B and C are likely to be temperature dependent as well. The order (first or second) of the transition depends on the sign of B with C being necessarily positive for stability. At thermal equilibrium the free energy of any systems is minimized.

$$\frac{\partial F}{\partial \eta}_{T,x} = 0 \tag{1.2}$$

$$0 = 2A\eta + 4B\eta^3 + 6C\eta^5 \tag{1.3}$$

If B is positive, the last term is negligible. Then

$$\eta^2 = 2A_0\frac{T_c - T}{4B}\eta(0)^2 = 2A_0\frac{T_c}{4B}\eta(T) = \eta(0)\sqrt{\frac{T_c - T}{T_c}} \tag{1.4}$$

This describes the change in the order parameter as a function of temperature in the second order continuous phase transition. If B is negative the transition is first order and discontinuous.

1.2 Domains and Ferroelectric polarization

Ferroelectric behavior arises from the fact that in the ferroelectric phase at least one set of ions in the crystal has a double well potential as shown in the figure 1.1. A local region where all of the ions in the crystal sit on the same side of the well is called domain[9].

If a ferroelectric phase transition takes place in an ideal crystal with an infinitely slow decrease in temperatures (to maintain thermal equilibrium in the crystal) then a single domain would form in the crystal. All ions in the crystal would be thermodynamically coupled and hence sit on the same side of the double well , the probability of the ion residing in one side or the other being equal. In real crystals different regions form ferroelectric phase independently resulting in domains with different directions of polarization

$$\overline{D} = \epsilon_0\overline{E} + \overline{P} \tag{1.5}$$

which relates the electric displacement $\overline{D}$ and electric field $\overline{E}$ to the polarization $\overline{P}$. The dielectric polarization $\overline{P}$ is due to both the polarizability of the material due to the applied field,$\overline{P_E}$ and from the spontaneous alignment of dipoles in the materials,$\overline{P_s}$.

$$\overline{P_E} = \chi \overline{E} \tag{1.6}$$

The free charge density must satisfy poissons equation

$$\nabla . \overline{D} = \rho \tag{1.7}$$

so that

$$\nabla . \overline{E} = \frac{1}{\epsilon \epsilon_0} (\rho - \nabla . \overline{P_s}) \tag{1.8}$$

In an infinite ideal ferroelectric crystal ,

$\nabla \ . \ \overline{E} = \frac{\rho}{\epsilon \epsilon_0}$ as in ordinary dielectrics. For a real crystal, P_s goes to zero at the crystal surface and may differ from the bulk crystal value at defect sites. For these reasons

$$\nabla . \overline{P_s} \tag{1.9}$$

acts as a polarizing field opposed to the dielectric polarization. It is this depolarizing field which can be compensated by the flow of free charge in the crystal. The energy associated with the depolarization of the crystal is zero for a totally compensated crystal in equilibrium. Domains form in fresh crystals to compensate for depolarization energy before free charge compensation takes place.

In a fresh crystal the net polarisation of the crystal should be zero due to the many domains of random polarization. In a nonconducting finite crystal a complex branched domain system is predicted to eliminate the electric field due to the surface. In real crystals even a low conductivity can compensate the surface effects and allow for a simpler columnar domain structure to form [1].

Polarization of ferroelectric crystals is accomplished by aligning the cells in the material in the same direction by the application of a field. This is done by increasing the size of domains in the desired direction while decreasing the size of domains in all the other direction until the crystal is one domain pointing in the direction of field.

Domain walls in ferroelectric are only a few unit cells wide with the polarization going to zero at the center of the wall.The domain width is dependant on the thickness of the crystal. If the thickness of the crystal decreases so that the domain width approaches the thickness of the domain wall the depolarizing field can no longer be compensated and there is a minimum film thickness for which ferroelectricity to be a stable state [1].The occurrence of a finite thickness has considerable implications for applications of ferroelectrics because it limits the useful thickness of these materials.

The primary property of a ferroelectric is the reversibility of its spontaneous polarization accomplished by reversing the direction of the applied field. Polarization reversal is demonstrated by a hystersis loop in the plot of polarization versus applied electric filed (P-E). This is measured using a Sawyer Tower circuit.

The coercive field E_c is the field at which half of the polarisation has been reversed. The remnant polarisation P_r is the polarisation which remains when the field is removed. A high polarisation and a low well defined coercive field results in a square shaped loop and the crystal is ideal for ferroelectric application.

Defects in ferroelectric crystals are evident from P-E plot. When the polarisation is reversed the polarisation due to defects will not reverse or may reverse at a different field than the rest of the crystal. if the defects do

reverse the value of coercive field is affected. if it doesnt reverse, the whole loop is biased along field axis.

1.3 Ferroelectric domains and hysterisis loop

A ferroelectric material is characterized by reversible spontaneous polarization arising from non centro symmetric arrangements of ions in its unit cell which produces a permanent electric dipole moment. Adjacent dipoles also tend to orient themselves in the same direction to form a region called ferroelectric domains. Ferroelectricity is commonly observed in ABO_3 perovskite structures and hence do not exhibit any spontaneous polarization (paraelectric phase). As the temperature is lowered below the curie point phase transformation take place from paraelectric state to ferroelectric state. The center ion is displaced from its body center position and cubic unit cell deforms to one of the non centrosymmentric structures such as tetragonal rhombohedral or monoclinic structure. The polarization response with the electric field of these materials is highly nonlinear and exhibits a hysteris loop as shown in figure 1.2.

Ferroelectrics are a subgroup of the pyroelectric materials which are in turn a subgroup of piezoelectric materials. These materials have a characteristic temperature -transition temperature- at which the material makes a structural phase change from a polar phase (ferroelectric) to a non polar called paraelectric phase [10].

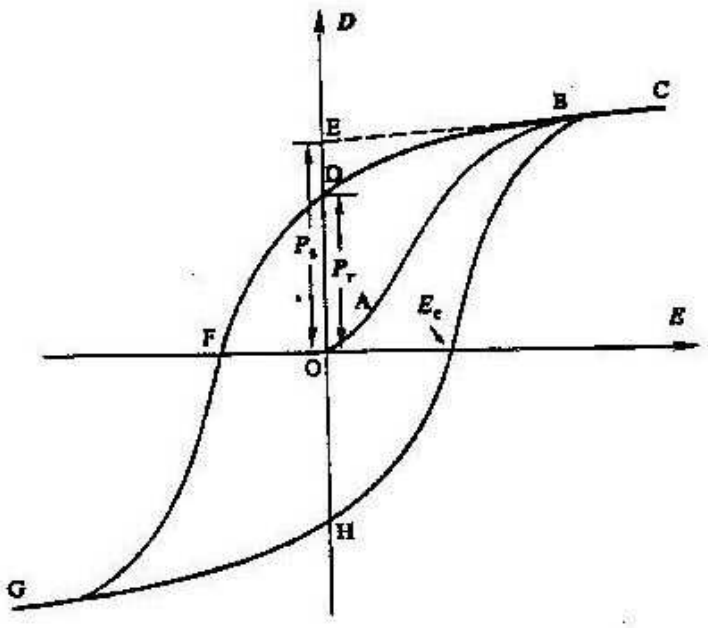

Figure 1.2: Polarization vs. Electric Field (P-E) hysteresis loop for a typical ferroelectric crystal

As the applied field is increased ferroelectric domains which are favorably oriented with respect to the applied field grow at the expense of other domains. This continues till the total domain growth and reorientation of all the domains has occurred in a direction favorable to the external field. At this stage the material is assumed to possess saturated polarization (P_{sat}). If the electric field is removed at this point some of the domains do not reorient into a random configuration and thus leaving the material still polarized. This polarization is the remnant polarization (P_r). The strength of the electric field required to return the polarization to zero is the coercive field (E_c).

The drive towards miniaturization in electronic devices has motivated scientists to focus on ways to improve the properties of dielectric and ferroelectric oxide thin film. The fabricated capacitors based on these oxide thin film are useful for the development of dynamic random access memories (DRAM)[11] or microwave devices [12]. An ideal capacitor based on these ferroelectric oxides should have high dielectric constant, high dielectric break down field strength, low leakage current density and low dissipation factor. Apart from electronic application ferroelectric films are of interest to various micro electromechanical and optical applications.

1.4 Oxygen octahedra

A very important group of ferroelectric is that known as the perovskite from the mineral perovskite $CaTiO_3$. The perfect perovskite structure is an extremely simple one with general formula ABO_3 where A is a monovalent or divalent metal and B is a tera or pentavalent one (figure 1.3.

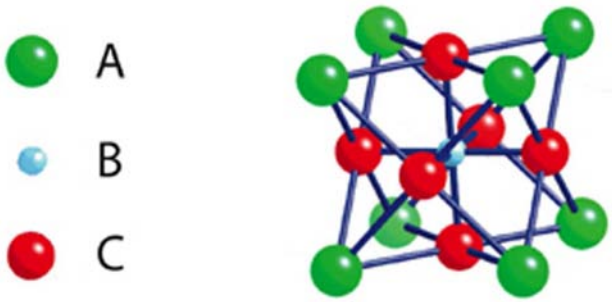

Figure 1.3: Perovskite structure with general formula ABO_3

The perovskite structure is cubic with A atoms at the cube corners, B atoms at the body centers and the oxygen at the face centers. The structure can also be regarded as a set of BO_6 octahedra arranged in a simple cubic pattern and linked togather by shared oxygen atoms with A atoms occupying the spaces between.

The first ferroelectric perovskite to be discovered was $BaTiO_3$. This rose the interest in ferroelectrics as it was earlier believed that H bond crystals alone show ferroelectricity.

Much simpler in their ferroelectric soft mode behaviour are the near ferroelectric $KTaO_3$ and $SrTiO_3$ and the actual ferroelectric $PbTiO_3$. Lead titanate in addition has a single ferroelectric phase whereas $BaTiO_3$ undergoes successive transitions to three different ferroelectric phases as the temperature is lowered. The great fascination of the perovskite structure is that it readily undergoes structural transitions involving non polar phonons (tilt in oxygen octahedron) in addition to both ferro and antiferroelectric transitions.

The O_6 group in particular can be thought of as a hard unit in the sense that it is little distorted from regular octahedron symmetry. In the cubic phase the O_6 octahedron are parallel but the bond angles at their corners are soft and tilting is easy. The simpleset tilt are those in which all octahedra tilt in alternating fashion about the same axis. There are three such possibilities a

two fold symmetry (diad-axis) tilt

three fold (triad axis)tilt

four fold (tetrad axis)tilt

The triad axis tilt then requires 3 equal non zero components and the diad axis tilt then requires two equal non zero components. However un-

equal tilt components and many other arrangement are possible. The off centering of the B cation is a relatively independent process that can occur in any structure built from hard octahedra. It is this off centering which leads to the presence of dipoles and to ferroelectric and antiferroelectric behaviour.

The types of ferroelectric materials have been grouped according to their structure. The four main types of structures include the corner sharing oxygen octahedra, compounds containing hydrogen bonded radicals, organic polymers and ceramic polymer composites. A large class of ferroelectric crystals are made up of mixed oxides containing corner sharing octahedra of O^{2-} ions (as shown in figure 1.4). The corner sharing oxygen octahedra discussed includes the perovskite type compounds, tungsten bronze type compounds, bismuth oxide layer structured compounds, and lithium niobate and tantalate [13].

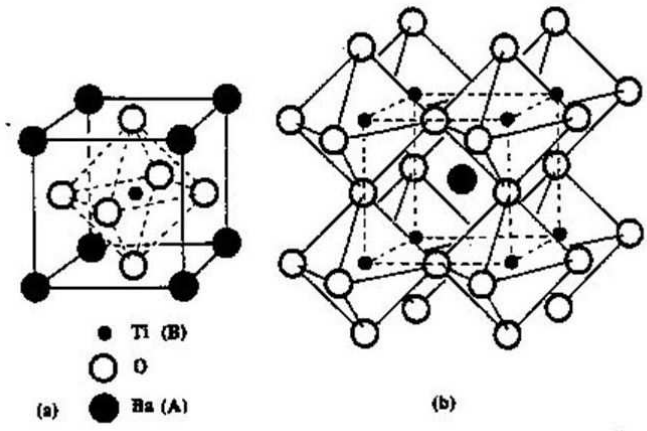

Figure 1.4: (a) A cubic ABO_3 ($BaTiO_3$) perovskite-type unit cell and (b) three dimensional network of corner sharing octahedra of O^{2-} ions

All most all the materials (except KNO_3) described by the general formula ABO_3 possess the perovskite crystal structure. The A element is a large cation situated at the corners of the unit cell (monovalent or divalent metal) and the B element is a smaller cation located at the body center (tetravalent or pentavalent metal). The oxygen atoms are at the face centers [1]. In the ferroelectric phase, perovskite structure assumes one of the three Bravis lattice: tetragonal, orthorhombic or rhombohedral.

In tetragonal symmetry a cubic cell stretches along one side (c axis) and shrinks along the other two sides (a axis) forming a rectangular prism. The spontaneous polarization aligns itself parallel to the longest side. The orthorhombic structure is formed by stretching the face diagonal along which the polarization aligns. In a rhombohedral structure cube is stretched along a body diagonal and polarization alignes in that direction.

In a paraelectric phase, the perovskite structure has cubic symmetry - neither stretched nor distorted. Ferroelectric materials for 64 and 256 Mb RAM [10]. It is the off centering of the B cataion that leads to ferroelectric and antiferroelectric behaviour. The B cations have two stable positions relative to the neighboring ions. A potential barrier separates one from the other. The ion can exchange position if enough energy is supplied to the system for the ion to overcome the barrier.

Some of the important compounds crystallizing in perovskite phase is discussed in detail.

1.4.1 Barium Titatate ($BaTiO_3$)

Barium titanate ($BaTiO_3$ / BT) has a paraelectric cubic phase above its Curie point of 130^oC. In the temperature range of 130^oC to 0^oC the ferroelectric tetragonal phase with a c/a ratio of ~ 1.01 is stable. The sponta-

neous polarization is along one of the [001] directions in the original cubic structure. Between 0^oC and -90^oC, the ferroelectric orthorhombic phase is stable with the polarization along one of the [110] directions in the original cubic structure. On decreasing the temperature below -90^oC the phase transition from the orthorhombic to ferroelectric rhombohedral phase leads to polarization along one of the [111] cubic directions. The spontaneous polarization on cooling $BaTiO_3$ below the Curie point T_c is due to changes in the crystal structure. As shown in figure 1.5a the paraelectric cubic phase is stable above 130^oC with the center of positive charges (Ba^{2+} and Ti^{4+} ions) coinciding with the center of negative charge (O^{2-}). On cooling below the Curie point T_c, a tetragonal structure (figure 1.5b) is evolved where the center of Ba^{2+} and Ti^{4+} ions are displaced relative to the O^{2-} ions, leading to the formation of electric dipoles. Spontaneous polarization developed is the net dipole moment produced per unit volume for the dipoles pointing in a given direction [14].

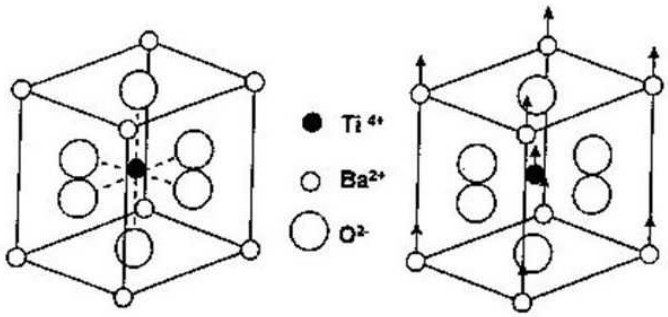

Figure 1.5: The crystal structure of $BaTiO_3$ (a) above the Curie point the cell is cubic; (b) below the Curie point the structure is tetragonal with Ba^{2+} and Ti^{4+} ions displaced relative to O^{2-} ions

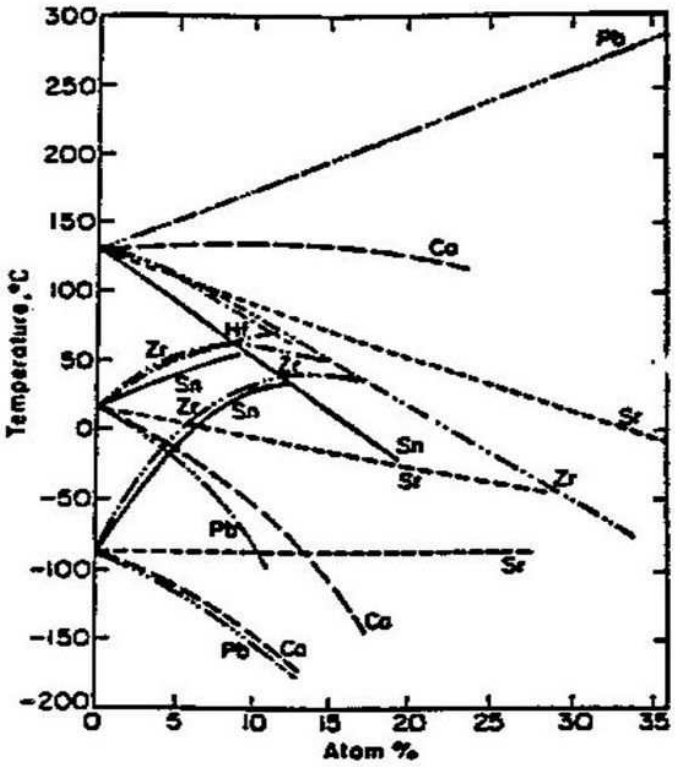

Figure 1.6: The effect of isovalent substitutions on the transition temperatures of $BaTiO_3$ ceramic [15]

Various A and B site substitutions in different concentrations have been tried to see their effect on the dielectric and ferroelectric properties of $BaTiO_3$. Sr^{2+} substitutions to the A site have been found to reduce the Curie point linearly towards room temperature. The substitution of Pb^{2+} for Ba^{2+} raises the Curie point. The simultaneous substitution into both A and B sites with different ions can be used to tailor the properties of $BaTiO_3$. The effect of various isovalent substitutions on the transition

temperatures of $BaTiO_3$ ceramic are shown in figure 1.6 [15–18].

The dielectric properties of $BaTiO_3$ are found to be dependent on the grain size [19–21]. Figure 1.7 shows the variation of dielectric constant with temperature for $BaTiO_3$ ceramics with a fine ($\sim$1 μm) and coarse ($\sim$50μm) grain size. Large grained $BaTiO_3$ ($\geq$1μm) shows an extremely high dielectric constant at the Curie point.

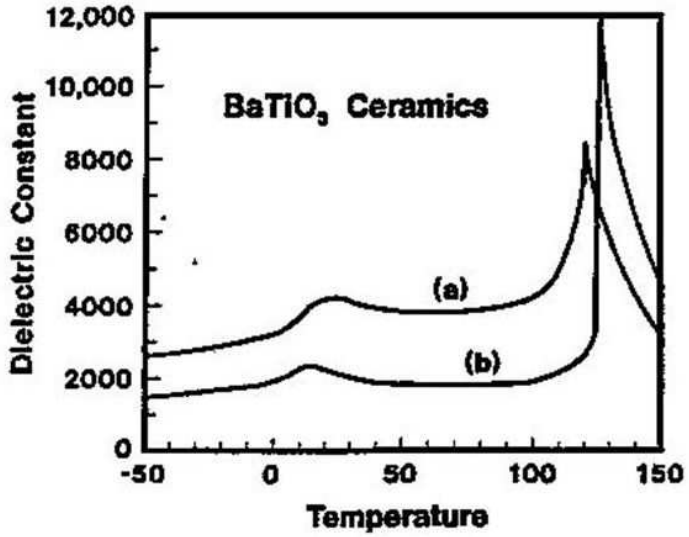

Figure 1.7: The variation of the relative permittivity (ϵ_r) with temperature for BaTiO3 ceramics with (a) $\sim$1μm grain size and (b) $\sim$50μm grain size [22].

This is because of the formation of multiple domains in a single grain, the motion of whose walls increases the dielectric constant at the Curie point. For a $BaTiO_3$ ceramic with fine grains ($\sim$1 μm), a single domain forms inside each grain. The movement of domain walls are restricted by the grain boundaries, thus leading to a low dielectric constant at the Curie

point as compared to coarse grained $BaTiO_3$ [22]. The room temperature dielectric constant (ϵ_r) of coarse grained ($\sim$10 μm) $BaTiO_3$ ceramics is found to be in the range of 1500-2000. On the other hand, fine grained ($\sim$1 μm) $BaTiO_3$ ceramics exhibit a room temperature dielectric constant between 3500-6000. The grain size effect on the dielectric constant at room temperature has been explained by the work of Buessem et. al. [23] and Arlt et. al [24]. Buessem and coworkers proposed that the internal stresses in fine grained $BaTiO_3$ must be much greater than the coarse grained ceramic, thus leading to a higher permittivity at room temperature.Arlt studied the domain structures in $BaTiO_3$ ceramics and showed that the room temperature ε_r reached a peak value at a critical grain size of $\sim 0.7\mu$m.

As the $BaTiO_3$ ceramics have a very large room temperature dielectric constant, they are mainly used multilayer capacitor applications. The grain size control is very important for these applications.

1.4.2 Barium Stronium Titanatae ($Ba_xSr_{1-x}TiO_3$)

$Ba_xSr_{1-x}TiO_3$(BST) is the solid solution between barium titanate ($BaTiO_3$) and strontium titanate ($SrTiO_3$) over the entire range of concentration.The dielectric and ferroelectric properties of $Ba_xSr_{(1-x)}TiO_3$ depend on Sr content. At room temperature $Ba_xSr_{(1-x)}TiO_3$ is ferroelectric, when x is in the range of 0.7-1 and is paraelectric when x is in the range 0-0.7[25]. As a result the electrical and optical properties of BST can be tailored over a broad range for various electronic applications [26].

The utilization of the $BaTiO_3$ - $SrTiO_3$ solid solution allows the Curie temperature (ferroelectricparaelectric transition temperature, Tc) of $BaTiO_3$ can be shifted from 120^0C to around room temperature for $Ba_xSr_{(1-x)}TiO_3$ films. For Sr addition into $BaTiO_3$, the linear drop of T_c is ca. 3.4^0C per

mol%. Therefore, 30mol% Sr (x = 0.3) would bring the T_c down to room temperature. BST films are not only paraelectric at the dynamic random access memory (DRAM) operating temperature range (0–70^0C ambient and 0–100^0C on chips) [27], but also achieve maximum permittivity around the operating temperature. On the other hand, the volatilities of the BST components are lower than Pb-based ferroelectric materials, thereby making it relatively easier to introduce into fabrication facilities [27, 28]. BST films are polycrystalline. Their properties heavily depend on composition, stoichiometry, microstructure (grain size and size distribution), film thickness, characteristics of electrode, and homogeneity of the film. The BST thin film growth method significantly affects the composition, stoichiometry, crystallinity, and grain size of the film and, consequently, its dielectric properties [29].

Barium strontium titanate (Ba,Sr)TiO_3 (BST) thin films are being widely investigated as alternative dielectrics for ultra large scale integrated circuits (ULSIs) DRAM storage capacitors [29–32] due to its

1. high dielectric constant (ϵ_r >200)
2. low leakage current
3. low temperature coefficient of electrical properties
4. small dielectric loss
5. free from fatigue or aging problems
6. high compatibility with device processes
7. linear relation of electric field and polarization

8. low Curie temperature

. However, whether BST thin film can be successfully applied largely depends on more thorough understanding the materials properties. The deposition techniques and electrical properties of BST films have received increasing interest. According to those investigations the electrical and dielectric properties and reliability of BST films heavily depend upon the deposition process, post-annealing process, composition, base electrodes, microstructure, film thickness, surface roughness, oxygen content and film homogeneity.

A variety of techniques such as rf-sputtering [33–35] , laser ablation [36] and solgel processing [37] have been used to deposit BST thin films. Above methods are highly competitive, each having advantages and disadvantages in terms of homogeneity, processing temperature, and processing costs. Because of the multicomponent nature of BST materials precise microscopic control of stoichiometry is essential for obtaining uniform single phase films. The basic parameters for applying capacitor thin films on DRAMs are dielectric constant, leakage current density and reliability. The targets for ideal Gbit era DRAM dielectrics include the followings [27]: (i) SiO_2 equivalent thickness <0.2 nm for Gbit; (ii) leakage current density <1< 10^{-7} Acm^{-2} at 1.6V; (iii) life time 10 years at 85^0C and 1.6V; (iv) stability 10^{15} cycles at > 100 MHz; and (v) general compatibility to semiconductor processing.

1.4.3 Lead Titanate ($PbTiO_3$)

Lead titanate ($PbTiO_3$/PT)is a ferroelectric material having a structure similar to $BaTiO_3$ with a high Curie point (490^oC). On decreasing the

temperature through the Curie point a phase transition from the paraelectric cubic phase to the ferroelectric tetragonal phase takes place. Lead titanate ceramics are difficult to fabricate in the bulk form as they undergo a large volume change on cooling below the Curie point. It is the result of the cubic (c/a = 1.00) to tetragonal (c/a = 1.064) phase transformation leading to a strain of >6%. Hence, pure $PbTiO_3$ ceramics crack and fracture during fabrication. The spontaneous strain developed during cooling can be reduced by modifying the lead titanate with various dopants such as Ca, Sr, Ba, Sn, and W to obtain a crack free ceramic.

1.4.4 Lead Zirconate Titanate($\mathbf{Pb(Zr_xTi_{(1-x)})O_3}$)

Lead Zirconate Titanate (PZT) is a binary solid solution of $PbZrO_3$ an antiferroelectric (orthorhombic structure) and $PbTiO_3$ a ferroelectric (tetragonal perovskite structure). PZT has a perovskite type structure with the Ti^{4+} and Zr^{4+} ions occupying the B site at random. The PZT phase diagram is shown in figure 1.8. At high temperatures PZT has the cubic perovskite structure which is paraelectric. On cooling below the Curie point line, the structure undergoes a phase transition to form a ferroelectric tetragonal or rhombohedral phase. In the tetragonal phase, the spontaneous polarization is along the <100> set of directions while in the rhombohedral phase the polarization is along the <111> set of directions [38].

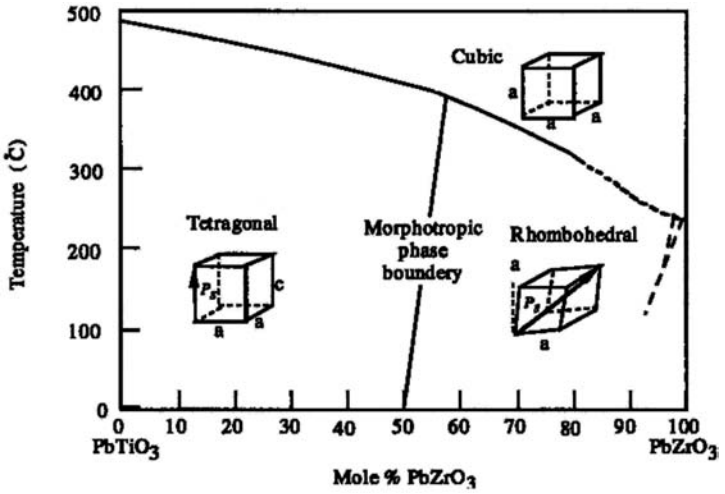

Figure 1.8: The PZT phase diagram

As shown in figure1.8 most physical properties such as dielectric and piezoelectric constants show an anomalous behavior at the morphotropic phase boundary (MPB). The MPB separating the two ferroelectric tetragonal and orthorhombic phases has a room temperature composition with a Zr/Ti ratio of $\sim$ 52/48. PZT ceramics with the MPB composition show excellent piezoelectric properties. The poling of the PZT ceramic is also easy at this composition because the spontaneous polarization within each grain can be switched to one of the 14 possible orientations (eight [111] directions for the rhombohedral phase and six [100] directions for the tetragonal phase). Below the Zr/Ti ratio of 95/5 the solid solution is antiferroelectric with an orthorhombic phase. On the application of an electric field to this composition a double hysteresis loop is obtained. This is because of the strong influence of the antiferroelectric $PbZrO_3$ phase [15].

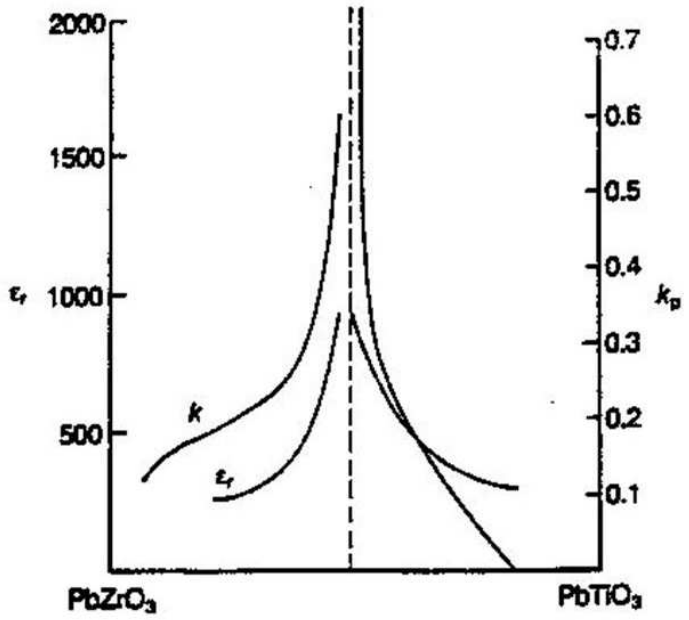

Figure 1.9: The effect of composition on the dielectric constant and electromechanical coupling factor kp in PZT ceramics

In order to suit some specific requirements for certain applications, piezoelectric ceramics can be modified by doping them with ions which have a valence different than the ions in the lattice. Piezoelectric PZT ceramics having the composition at the MPB can be doped with ions to form "hard" and "soft" PZT. Hard PZT are doped with acceptor ions such as K^+, Na^+ (for A site) and Fe^{3+}, Al^{3+}, Mn^{3+} (for B site), creating oxygen vacancies in the lattice [39, 40]. Hard PZT usually have lower permittivities, smaller electrical losses and lower piezoelectric coefficients. These are more difficult to pole and depole, thus making them ideal for rugged applications. On the other hand, soft PZT are doped with donor ions such as

La^{3+} (for A site) and Nb^{5+}, Sb^{5+} (for B site) leading to the creation of A site vacancies in the lattice [41–44]. The soft PZT have a higher permittivity, larger losses, higher piezoelectric coefficient and are easy to pole and depole. They can be used for applications requiring very high piezoelectric properties.

1.4.5 Lead Lanthanum Zirconate Titanate $(\mathbf{Pb_{1-x}La_x})(\mathbf{Zr_{1-y}Ti_y})_{1-x/4}\mathbf{O_3}$

$(Pb_{1-x}La_x)(Zr_{1-y}Ti_y)O_3$ PLZT is a transparent ferroelectric ceramic formed by doping La^{3+} ions on the A sites of lead zirconate titanate (PZT). The PLZT ceramics have the same perovskite structure as $BaTiO_3$ and PZT. The transparent nature of PLZT has led to its use in electro-optic applications. Before the development of PLZT, the electro-optic effect was seen only for single crystals. The two factors that are responsible for getting a transparent PLZT ceramic include the reduction in the anisotropy of the PZT crystal structure by the substitution of La^{3+} and the ability to get a pore free ceramic by either hot pressing or liquid phase sintering.

The general formula for PLZT is given by $(Pb_{1-x}La_x)(Zr_{1-y}Ti_y)_{1-x/4}O_3V^B{}_{0.25x}O_3$ and $(Pb_{1-x}La_x)_{1-0.5x}(Zr_{1-y}Ti_y)V^A{}_{0.5x}O_3$. The first formula assumes that La^{3+} ions go to the A site and vacancies (V^B) are created on the B site to maintain charge balance. The second formula assumes that vacancies (V^A) are created on the A site. The actual structure may be due to the combination of A and B site vacancies.

The room temperature phase diagram of PLZT system is shown in figure 1.10. The different phases in the diagram are a tetragonal ferroelectric phase (FE_{Tet}), a rhombohedral ferroelectric phase (FE_{Rh}), a cubic re-

laxor ferroelectric phase (FE_{Cubic}), an orthorhombic antiferroelectric phase (AFE) and a cubic paraelectric phase (PE_{Cubic}) [45].

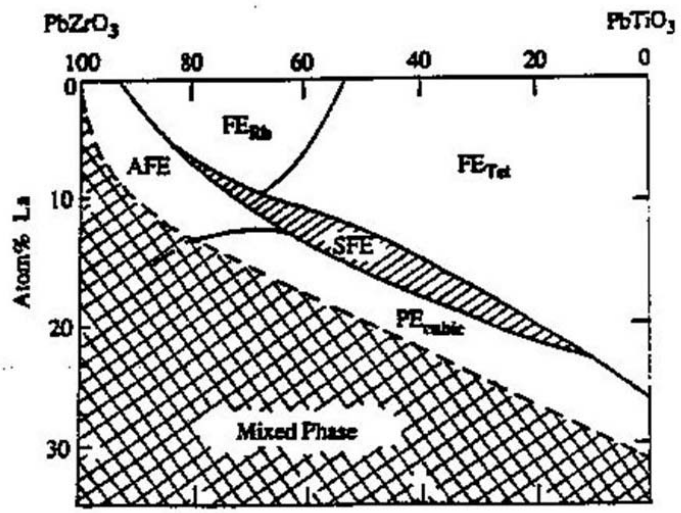

Figure 1.10: Room temperature phase diagram of the PLZT system. The regions in the diagram are, a tetragonal ferroelectric phase (FE_{Tet}); a rhombohedral ferroelectric phase (FE_{Rh}); a cubic relaxor ferroelectric phase (FE_{Cubic}); an orthorhombic antiferroelectric phase (AFE); and a cubic paraelectric phase (PE_{Cubic}).

The electro-optic applications of PLZT ceramics depends on the composition. Figure 1.11 shows the hysteresis loops for various PLZT compositions from the phase diagram. PLZT ceramic compositions in the tetragonal ferroelectric (FE_{Tet}) region show hysteresis loops with a very high coercive field (E_C). Materials with this composition exhibit linear electro-optic behavior for $E < E_C$. PLZT ceramic compositions in the rhombohedral ferroelectric (FE_{Rh}) region of the PLZT phase diagram have loops with a low coercive field. These PLZT ceramics are useful for optical memory

applications [45].

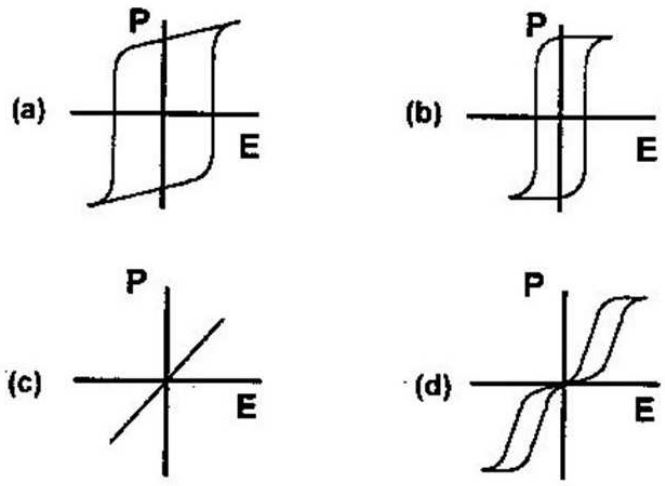

Figure 1.11: Representative hysteresis loops obtained for different ferroelectric compositions (a) FE_{Tet} (b) FE_{Rh} (c) FE_{Cubic} and (d) AFE regions of the PLZT phase diagram.

PLZT ceramic compositions with the relaxor ferroelectric behavior are characterized by a slim hysteresis loop (figure 1.11). They show large quadratic electro-optic effects which are used for making flash protection goggles to shield them from intense radiation. This is one of the biggest applications of the electro-optic effect shown by transparent PLZT ceramics. The PLZT ceramics in the antiferroelectric region show a hysteresis loop expected from an antiferroelectric material. These components are used for memory applications [45–48].

Material process issues in PZT

A good ferroelectric film has a high remnant polarization ie a large amount of charge can be stored in a small area and a small coercive field ie it can be polarized at low voltages. For use in transparent devices a high optical transmittance is also needed. Most defects in PZT is due to vacancies, usually lead and oxygen. PbO is volatile and PZT can accommodate large amounts of lead and oxygen vacancies which can interact with one another [49]. Low resistivity is also attributed to lead loss in PZT films.Lead loss is avoided by adding 2 to 10% excess lead in the starting material [50, 51]. Oxygen vacancies is inhibited by including donor dopants in PZT.

Lead loss causes PZT to behave like a p-type semiconductor. The lead vacancies (V_{Pb}) act as acceptors and cause the Fermi level to move towards the valence band [52]. When it is thermodynamically more favorable to create an oxygen vacancy (V_0) to compensate the lead vacancy than it is to further modulate the Fermi level, oxygen vacancies form concomitantly with lead vacancies and the materials exhibits fatigue and conductivity. Figure 1.12 shows the relationship between oxygen and lead vacancies and the Fermi level in the PZT band gap.

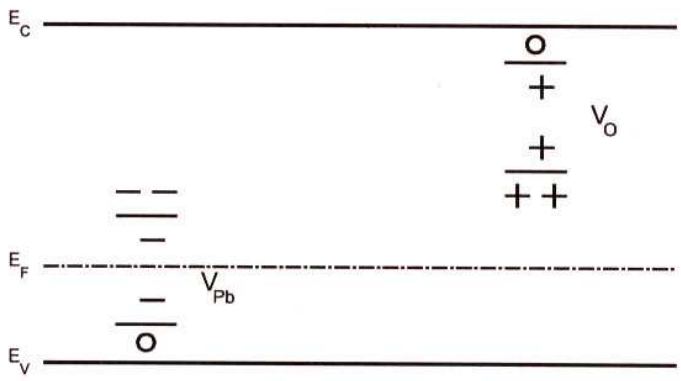

Figure 1.12: Energy level due to lead and oxygen vacancies in the PZT band gap

The migration of oxygen vacancies during polarisation causes fatigue [1]. Intentional donar doping has been shown to counteract fatigue in ferroelectric capacitors by the suppression of the formation of oxygen vacancies. Fatigue occurs when upon repeated switching of a crystal the polarisation becomes clamped while the coercive field increases and become less well defined. Fatigue causes a longer switching time for the crystal. The fatigue can be reduced or eliminated by choosing oxide electrodes.

It is common practise to include donar dopants in PZT to improve electrical and optical properties. The most common A site donar dopants are trivalent lanthanum (La) and yttrium (Y). Lanthanum donar dopants in PZT compensate the lead vacancy acceptors thereby inhibiting the formation of oxygen vacancies. Figure1.13 shows La donar sites in the band gap.(Pb,La)(Zr,Ti)O_3 (PLZT) is valued for its exceptional electro optical properties and its increased transparency compared to PZT [51]. But PLZT has a smaller amount of polarization and a less squareness hysteresis loop

when compared to PZT with the same Zr/Ti ratio [49].

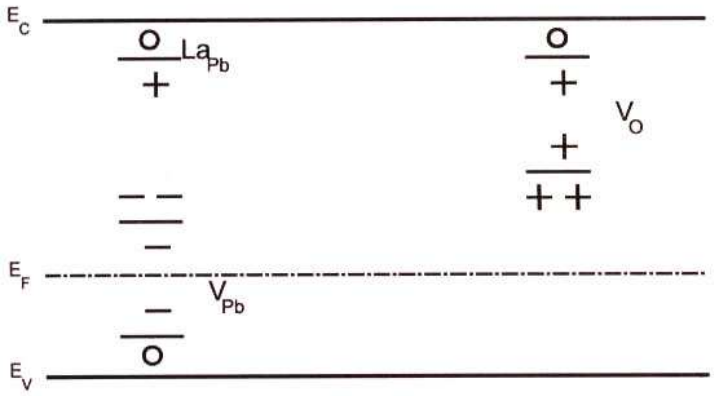

Figure 1.13: La donors levels in the band gap of PZT compensate lead vacancies leading to the suppression of compensation induced oxygen vacancies

Common B-site donar dopants are pentavalent niobium (Nb) and the tantalum (Ta) which substitute for quadrivalent Zr or Ti. A thin layer of $PbTiO_3$ (PT) grown before the deposition of PZT or PLZT has been shown to assist in the crystallisation in the perovskite phase since $PbTiO_3$ always crystallise in the perovskite phase. Very thin layer of $PbTiO_3$ will facilitate the growth of the perovskite phase and have little effect on the dielectric properties of the film but increasing the thickness of $PbTiO_3$ buffer layer causes a decrease in the dielectric constant due to the lower dielectric constant of $PbTiO_3$ layer compared to the PZT.

1.4.6 Lead Magnesium Niobate ($Pb(Mg_{1/3}Nb_{2/3})O_3$

Relaxor ferroelectric are a class of lead based perovskite type compounds with the general formula $Pb(B_1,B_2)O_3$ where B_1 is a lower valency cation

(like Mg^{2+}, Zn^{2+}, Ni^{2+}, Fe^{3+}) and B_2 is a higher valency cation (like Nb^{5+}, Ta^{5+}, W^{5+}). Pure lead magnesium niobate (PMN or $Pb(Mg_{1/3}Nb_{2/3})O_3$) is a representative of this class of materials with a Curie point at -10^o C. The main differences between relaxor and normal ferroelectrics is shown in Table 1.1.

Table 1.1: Differences between normal and relaxor ferroelectrics.[53]

Property	Normal Ferroelectric	Relaxor Ferroelectric
Dielectric temperature dependence	Sharp 1^{st} or 2^{nd} order transition at Curie point T_c	Broad diffused phase transition at Curie maxima
Dielectric frequency dependence	Weak Frequency dependence	Strong frequency dependence
Dielectric Behavior in paraelectric range ($T > T_c$)	Follows Curie - Weiss law	Follows Curie - Weiss square law
Remnant polarization (P_R)	Strong P_R	Weak P_R
Scattering of light	Strong anisotropy	Very weak anisotropy to light
Diffraction of x-rays	Line splitting due to deformation from paraelectric to ferroelectric phase	No x-ray line splitting

Table 1.2: Major families of ferroelectric oxides [54]

Materials	**Characteristics**	**Applications**
$BaTiO_3$,BST, $SrTiO_3$	Dielectric, Pyroelectric, Ferroelectric , electro-optic	DRAM capaciors,sensors, Phase shifters , SHG
$PbTiO_3$ PT, $Pb(ZrTi)O_3$, PZT, $(Pb,La)(Zr,Ti)O_3$ PLZT	Dielectric, Pyroelectric, Ferroelectric, Piezoelectric, electro-optic,	Pyrodetectors, transducers, Non volatile memory, SHG, optical memory
$SrBi_2Ta_2O_9$	Ferroelectric	Non volatile memory
$Pb(Mg_{1/3}Nb_{2/3})O_3$ PMN-PT	Dielectric , electro-optic	Capacitor memory, waveguide devices
$LiNbO_3$, $LiTaO_3$	Piezoelectric devices, electro-optic	Pyrodetectors, waveguide applications, SHG, optical modulators
$KNbO_3$, K(Ta, Nb)O_3	Pyroelectric, electro-optic	Waveguided devices, frequency doublers, holographic storage , pyro- detector

Relaxor ferroelectrics like PMN can be distinguished from normal ferroelectrics such as $BaTiO_3$ and PZT, by the presence of a broad diffused and dispersive phase transition on cooling below the Curie point. The dif-

fused phase transitions in relaxor ferroelectrics are due to the compositional heterogeneity seen on a microscopic scale.

Major families of ferroelectric oxides with their important properties and application are listed in table 1.2.

1.5 Application

Ferroelectric thin films have attracted attention for applications in many electronic and electro-optic devices. Some of the important ferroelectric materials being used for making thin films include the perovskite type materials such as $BaTiO_3$,$(Ba_xSr_{1-x})TiO_3$, $PbTiO_3$, $Pb(Zr_xTi_{1-x})O_3$ and $Pb(Mg_{1/3}Nb_{2/3})O_3$. Applications of ferroelectric thin films utilize the unique dielectric, piezoelectric, pyroelectric, and electro-optic properties of ferroelectric materials. Some of the most important electronic applications of ferroelectric thin films include nonvolatile memories, thin films capacitors, pyroelectric sensors, and surface acoustic wave (SAW) substrates. The electro-optic devices being studied include optical waveguides and optical memories and displays.

There are three important ferroelectric thin film non volatile random access memory (NVRAM) concepts. Two are based on nondestructive readout (NDRO) approach which avoids repolarisation of the ferroelectric after a read operation. In one of these designs a ferroelectric thin film controls the source to drain current through the FET. However the charge injection from the ferroelectric semiconductor interface can be a limiting problem.

The second NDRO approach is less developed. It uses a polarisation depend photoinduced current from a capacitor to read the memory cell. This

concept would be especially useful for more advanced memory application such as high capacity parallel processor or an optical image comparator.

The final NVRAM approach has received more widespread attention. It uses the remanent polarisation of a ferroelectric capacitor to store information. The polarisation state is read by measuring the current drawn through the capacitor by an applied volatge pulse. Since this read operation can reverse the polarisation state it is known ad destructive read out (DRO) device.

1.5.1 Novel microelectronic devices

Novel devices make use of the large dielectric constant or the desirable piezoelectric and electrooptic properties of ferroelectric thin film materials. In ultra large scale integrated (ULSI) circuits the decreasing area for capacitors requires a concomitant but unattainable decrease in layer thickness of standard dielectrics. Use of a large dielectric constant material would allow thicker films and ferroelectric materials having high dielectric constant is employed for such applications.

High dielectric constant ferroelectric materials could also be used in microwave monolithic integrated circuits (MMIC). For example on chip bypass capacitor. Another potential microwave application of ferroelectric thin film is for phase shifting. A DC bias applied across the ferroelectric layer controls the dielectric constant and hence its phase velocity through MIM structure. The large peizoelectric properties of ferroelectric thin films can be useful for the fabrication of surface acoustic wave devices (SAW). Interdigital transducers (IDTs) with finger like pattern on the surface can be used to launch acoustic wave into the underlying material at resonant frequencies. Similar IDTs can act as receivers for the launched acoustic

waves. This structure can function as a high frequency filter or be used to diffract an optical signal in an acoustic devices. The strong electro optical coupling of many ferroelectric materials provide a number of application in thin film form. Optical wave guides fabricated in ferroelectric thin films could be used in directional couplers, Mach-Zehndar intensity modulators and total internal reflection switches.

1.5.2 Sensors and Actuators

The research area of micro electro mechanical systems (MEMS) has been receiving much attention lately. In MEMS, sensors and actuators are constructed on a microscale using lithographic techniques developed for integrated circuit fabrication. A number of devices have been conceived and studied that utilize the peizoelectric and pyroelectric properties of ferroelectric materials. Devices require epitaxial growth, coherent interfaces with an underlying semiconductor substrate and lower processing temperatures. High quality epitaxial films may offer advantages in terms of sensitivity and reduced leakage current under dc bias.

1.5.3 Smart materials and adaptive structures

Smart materials are able to alter their performance in response to their environment or an external stimulus. By designing they should perform this function automatically although separate sensing component may provide the stimulus. An example is the use of adaptive optics to compensate for turbulence in the atmosphere

1.5.4 Thin film Capacitors

The high dielectric permittivity of ferroelectric ceramics such as $BaTiO_3$,BST, PMN and PZT make them very useful for capacitor applications. The MLC (multilayer ceramic capacitors) have a very high volumetric efficiency (capacitance per unit volume) because of the combined capacitance of thin ceramic tapes of thickness $\sim$ 10-20 μ m stacked one on top of the other. The volumetric efficiency of the MLC capacitor can be further increased if the thickness of the ceramic sheets can be made lower ($<$ 10 μ m). Thin film technology can be used to make dielectric layers as thin as 1 μ m. $BaTiO_3$ and PMN are the two important materials being looked at for thin film MLC applications [55].

1.6 Ferroelectric RAM memory

There are worldwide considerable efforts to develop nonvolatile random access memories. Portable electronic equipment such as the personal digital assistant, cellular phones or digital cameras need secure and fast data transfer in combination with nonvolatile storage. Another main development route is that of contact less smart cards with multiple functions including e.g. personal banking, transport access and medical data. The market for non-volatile random access memories (NVRAMs) has been drastically increased over the last years, although by far not reaching the market volume of (volatile) dynamic random access memories (DRAMs). The required performance of NVRAMs, such as, storage density, endurance, write and access time or power consumption are related to a particular application. Therefore it is not astonishing that a number of different NVRAMs technologies exist to fulfill all requirements.

1.6.1 History of FeRAM

Ferroelectric RAM was proposed and published in 1952. Development of FeRAM began in the late 1980s. Work was done in 1991 at NASA's Jet Propulsion Laboratory on improving methods of read out, including a novel method of non-destructive readout using pulses of UV radiation [56]. Much of the current FeRAM technology was developed by Ramtron, a fabless semiconductor company. One major licensee is Fujitsu, who operate what is probably the largest semiconductor foundry production line with FeRAM capability. Since 1999 they have been using this line to produce standalone FeRAMs, as well as specialized chips (e.g. chips for smart cards) with embedded FeRAMs within. Fujitsu produces devices for Ramtron. By 2005, Ramtron reported that they were evaluating prototype samples of an 8 megabit FeRAM manufactured using Texas Instruments'(TI) FeRAM process. Fujitsu and Seiko-Epson were in 2005 collaborating in the development of a 180 nm FeRAM process. FeRAM research projects have also been reported at Samsung, Matsushita, Oki, Toshiba, Infineon, Hynix, Symetrix, Cambridge University, University of Toronto and the Interuniversity Microelectronics Centre , Belgium.

1.6.2 Working of FeRAM

The reversible sponatnoues polarization of ferroelectric materials make them attractive for memory applications. An ideal memory device has low power consumption fast read and write access times and infinite rewritability. Memory devices should also be scalable. A ferroelectric non volatile (NV) memory must be able to maintain its orientation in the absence of

applied power for more than ten years in order to compete with modern devices [57].

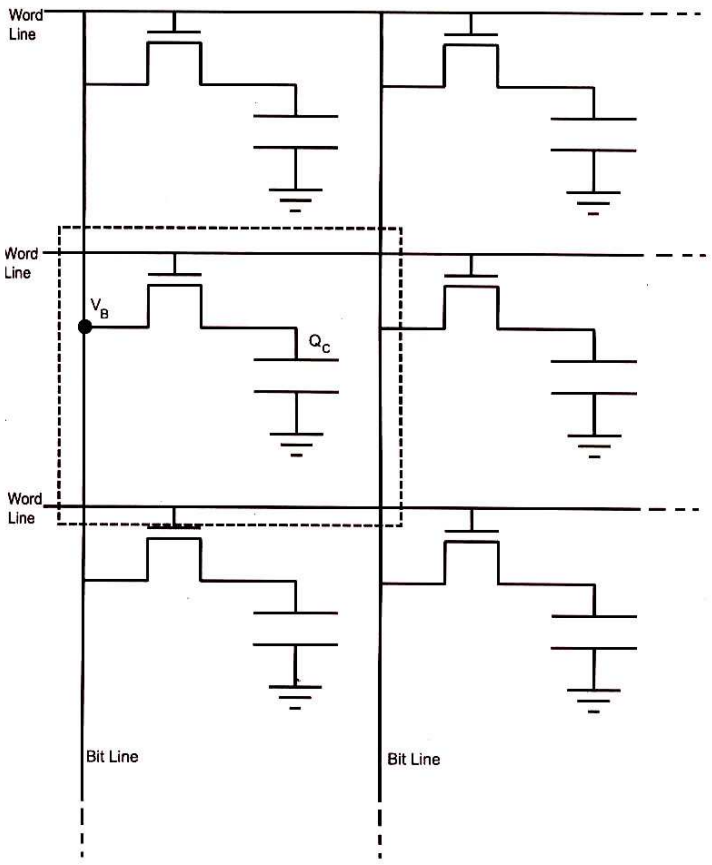

Figure 1.14: FRAM circuit diagram with one memory cell indicated

Designs for ferroelectric memory have two basic types; capacitor type memories have ferroelectric capacitor in series with field effect transistor (FRAM) and transistor type memories have a ferroelectric material as the

gate dielectric of the ferroelectric field effect transistor (FEFET) [34]. Non volatile ferroelectric random access memory (NVFRAM) are the first ferroelectric devices to be commercially available [58].

Memory arrays of capacitor type FRAM have advantages over current magnetic hard disks and floppy disks. FeRAM have no moving parts, more reliable and have faster read/write access time. Moreover the ferroelectric materials have dielectric constants up to 500 times larger than current memory dielectrics so more charge can be stored in a smaller surface area [57].

FRAM is based on the DRAM structure in which a capacitor is connected in series with a transistor. Figure 1.14 shows a circuit diagram of a FRAM devices. The success of DRAM is largely due to its small cell size. DRAM and FRAM store one bit on one capacitor and one transistor [59].

Data are stored in an array of capacitors each connected to the sources of a metal oxide semiconductor (MOS) transistor. The drains of the transistors are connected to the bit lines and the gates are connected to the word lines. Data are written to the capacitors by applying a voltage to the word lines to turn on the transistors. those which connects each capacitor to its bit line. Then a voltage greater than the ferroelectric capacitors positive coercive voltage or a voltage greater than the capacitors negative coercive voltage is applied to the bit line to write 1 or 0 to the cell, respectively.

To read the cell the transistors are turned on and the capacitors discharge onto the bit line. At the end of each bit line a sense amplifer determines whether the cell was written with 1 or a 0 and then rewrites the cell by applying the appropriate voltage. DRAM is volatile, the capacitors must be refreshed occasionally to maintain the memory (charge).

The advantage of using a ferroelectric capacitor in DRAM cell is the nonvolatility of the ferroelectric polarization. An FRAM is non volatile memory that is as small as a DRAM cell with no moving parts. When a material has a higher dielectric constant more charge can be stored in a smaller area.

Like DRAM, FRAM is a destructive read out (DRO) device, which means that the information stored in the cell is lost when the cell is read and must be written after it is read. Reading an FRAM cell requires that the polarization on the capacitor be reversed. This means that FRAM devices will be read and rewritten more often than nondestructive read out (NDRO) devices. The quality of the capacitor is integral to the device properties.

It is also important that the devices be symmetric that is the positive and negative coercive voltages have approximately the same value, which remains constant in time. Since the device is written with a 1 or 0 with a voltage pulse that is greater than the coercive voltage, the coercive voltage must remain the same over time in order to properly polarize the device with that pulse. Hence only capacitors which exhibit low fatigue and imprint properties can be used in FRAM devices. The two coercive voltage points should be symmetrical and less than 2.5V in order to operate from standard memory voltage power supply's [57].

A schematic representation of FeRAM is shown in the figure 1.15.Ferroelectric capacitors are usually integrated on to a CMOS processed chip in a back end process to keep from contaminating the CMOS facility. All the process involved in the patterning and deposition of ferroelectric capacitors have to be safe for CMOS devices [58] and must not damage the ferroelectric layer [34].

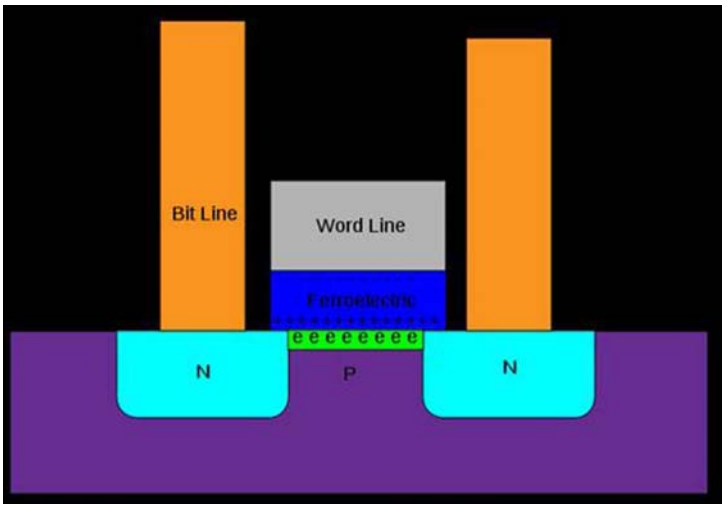

Figure 1.15: Schematic representation of FeRAM

1.6.3 Comparison with other systems

Density

The main factor that determinate the memory system's cost is the density of the components used to make it up. Smaller components, and less of them, means that more cells can be packed onto a single chip, which in turn means more can be produced from a single silicon wafer. This improves yield, which is directly related to cost.

The lower limit to this scaling process is an important point for comparison, generally the technology that scales to the smallest cell size will end up being the least expensive per bit. FeRAM and DRAM are constructionally similar, and can generally be built on similar lines at similar sizes. In both cases the lower limit seems to be defined by the amount of charge needed to trigger the sense amplifiers. For DRAM, this appears to be a

problem at around 55 nm, at which the charge stored in the capacitor is too small to be detected. It is not clear if FeRAM can scale to the same size, as the charge density of the PZT layer may not be the same as the metal plates in a normal capacitor.

An additional limitation on size is that materials tend to stop being ferroelectric when they are too small [60, 61]. This effect is related to the ferroelectric's "depolarization field". There is ongoing research on addressing the problem of stabilizing ferroelectric materials; one approach, for example, uses molecular adsorbates.

To date, the commercial FeRAM devices have been produced at 350 nm and 130 nm.

Power Consumption

The key advantage of FeRAM over DRAM is the low power consumption which could be understood from read and write cycles. In DRAM, the charge deposited on the metal plates leaks across the insulating layer and the control transistor, and disappears. In order for a DRAM to store data for anything other than a microscopic time, every cell must be periodically read and then re-written, a process known as refresh. Each cell must be refreshed many times every second (65ms) [62] and this requires a continuous supply of power.

In contrast, FeRAM only requires power when actually reading or writing a cell. The vast majority of power used in DRAM is used for refresh, indicating power usage about 99% lower than DRAM.

Another non-volatile type memory is Flash RAM, and like FeRAM it does not require a refresh process. Flash works by pushing electrons across a high-quality insulating barrier where they get "stuck" on one terminal of

a transistor. This process requires high voltages, which are built up in a charge pump with time. This means that FeRAM could be expected to be lower power than Flash, at least for writing, as the write power in FeRAM is only marginally higher than reading. For a "mostly-read" device the difference might be slight, but for devices with more balanced read and write the difference could be expected to be much higher.

Performance

DRAM performance is limited by the rate at which the charge stored in the cells can be drained (for reading) or stored (for writing). Generally this ends up being defined by the capability of the control transistors, the capacitance of the lines carrying power to the cells, and the heat that power generates.

FeRAM is based on the physical movement of atoms in response to an external field, which happens to be extremely fast, settling in about 1 ns. In theory, this means that FeRAM could be much faster than DRAM. However, since power has to flow into the cell for reading and writing, the electrical and switching delays would likely be similar to DRAM overall. It does seem reasonable to suggest that FeRAM would require less charge than DRAM, because DRAMs need to hold the charge, whereas FeRAM would have been written to before the charge would have drained. That said, there is a delay in writing because the charge has to flow through the control transistor, which limits current somewhat.

In comparison to 'Flash' the advantages are much more obvious. Whereas the read operation is likely to be similar in performance, the charge pump used for writing requires a considerable time to "build up" current, a process that FeRAM does not need. Flash memories commonly need about

1 ms to write a bit, whereas even current FeRAMs are at least 100 times that data rate.

Existing 350 nm devices have read times of the order of 50-60 ns. Although slow compared to modern DRAMs, which can be found with times of the order of 2 ns, common 350 nm DRAMs operated with a read time of about 35 ns, so FeRAM performance appears to be comparable given the same fab [62].

1.6.4 Recent trends in ferroelectric materials

FeRAM remains a relatively small part of the overall semiconductor market. Flash memory is currently the overwhelmingly dominant NVRAM technology, and this situation seems likely to continue for at least the rest of the decade. The much larger sales of flash memory compared to the alternative NVRAMs support a much larger research and development effort. Flash memory is produced using semiconductor linewidths of 30 nm at Samsung (2007) while FeRAMs are produced in linewidths of 350 nm at Fujitsu and 130 nm at Texas Instruments (2007). Flash memory cells can store multiple bits per cell (currently 2 in the highest density NAND flash devices), and the number of bits per flash cell is projected to increase to 4 or even to 8 as a result of innovations in flash cell design. The areal bit densities of flash memory are consequently much higher than FeRAM, and thus the cost per bit of flash memory is orders of magnitude cheaper than FeRAM.

The density of FeRAM arrays might be increased by improvements in FeRAM foundry process technology and cell structures, such as the development of vertical capacitor structures (in the same way as DRAM) to reduce the area of the cell footprint. However, reducing the cell size may cause the

data signal to become to too weak to be detectable. Theoretically, it should be possible to embed FeRAM cells using two additional masking steps during conventional CMOS semiconductor manufacture. Flash typically requires nine masks. This could make possible for example, the integration of FeRAM on microcontrollers, where a simplified process would reduce costs. However, the materials used to make FeRAMs are not commonly used in CMOS integrated circuit manufacturing. Both the BST/PZT ferroelectric layer and the noble metals used for electrodes raise CMOS process compatibility and contamination issues.

The FM22L16 is the semiconductor industrys highest density FRAM, a 4-Mbit, 3V, parallel nonvolatile RAM that breaks new technological ground. It is manufactured on TIs advanced 130nm CMOS process. The FM22L16 is a 256Kx16 nonvolatile memory that reads and writes like a standard static RAM. A ferroelectric random access memory or FRAM is nonvolatile, which means that data is retained after power is removed. It provides data retention for over 10 years while eliminating the reliability concerns, functional disadvantages and system design complexities of battery-backed SRAM (BBSRAM). Fast write timing and high write endurance make FRAM superior to other types of memory.

The FM22L16 includes a low voltage monitor that blocks access to the memory array when virtual device driver (VDD) drops below a critical threshold. The memory is protected against an inadvertent access and data corruption under this condition. The device also features software-controlled write protection. The memory array is divided into 8 uniform blocks, each of which can be individually write protected.

Chapter 2

Thin film deposition techniques and characterization tools

In this chapter various techniques that were used in the process of thin film deposition is detailed . Ferroelectric films studied in the present work were prepared using rf magnetron sputtering and pulsed laser deposition.The electrodes for the capacitors were deposited using electron beam and thermal evaporation method. Various thin film characterisation methods, that were used to optimise film properties, are discussed.

2.1 Introduction

A thin film is defined as a low-dimensional material created by condensing, one-by-one, atomic/molecular/ionic species of matter. The thickness is typically less than a few micrometers. Thin films differ from thick films.

A thick film is defined as a low-dimensional material created by thinning a three-dimensional material or assembling large clusters/aggregates/ grains of atomic/molecular/ionic species [63]. Thin film technology is one of the oldest arts and one of the newest sciences. Thin films have been used for more than a half century in making electronic devices, optical coatings, hard coatings, and decorative parts.

The birth of thin films of all materials by any deposition technique starts with a random nucleation process followed by nucleation and growth stages. Nucleation and growth stages are dependent upon various deposition conditions, such as growth temperature, growth rate, and substrate chemistry. The nucleation stage can be modified significantly by external agencies, such as electron or ion bombardment. Film microstructure, associated defect structure, and film stress depend on the deposition conditions at the nucleation stage. The basic properties of film, such as film composition, crystal phase and orientation, film thickness, and microstructure, are controlled by the deposition conditions.

The chemical composition of deposited films is governed by the substrate temperature and/or the deposition atmosphere. Under low substrate temperatures, the chemical composition of deposited films coincides with that of the source materials. Under high substrate temperatures, the chemical composition of deposited films differs from the source materials due to the re-evaporation of high vapor pressure materials from the films during the deposition.

Thin films exhibit unique properties that cannot be observed in bulk materials. The atomic growth process results in unique material properties from like size effects, including quantum size effects, characterized by the thickness, crystalline orientation, and multi-layer aspects.

2.2 Experimental techniques

The properties of thin films are governed by the deposition method. Almost all thin film deposition and processing method employed to characterize and measure the properties of films requires either a vacuum or some sort of reduced pressure ambient. Deposition technologies can be divided into two groups: Chemical Vapor Deposition (CVD) and Physical Vapor Deposition (PVD) processes.

Chemical vapor deposition (CVD) is the process of chemically reacting a volatile compound of a material to be deposited, with other gases, to produce a nonvolatile solid that deposits on a suitably placed substrate [64]. Because CVD processes do not require vacuum or unusual levels of electric power, they were practiced commercially prior to PVD. But they are subject to thermodynamic and kinetic limitations and constrained by the flow of gaseous reactants and products.

PVD processes (often just called thin film processes) are atomistic deposition processes in which material is vaporized from a solid or liquid source in the form of atoms or molecules. The evaporated material gets transported in a low pressure or plasma environment to the substrate where it condenses and forms thin layer of film. PVD can be used to deposit films of elements, alloys as well as compounds. In reactive deposition, compounds are formed by the reaction of depositing material with the ambient gas environment such as nitrogen or oxygen. PVD includes techniques like thermal evaporation, sputtering, pulsed laser deposition.

2.2.1 Thermal evaporation

Vacuum thermal evaporation controllably transfer atoms from a heated source to a substrate located a distance away, where film formation and growth proceed atomistically. Thermal energy is imparted to atoms in a liquid or solid source such that their temperature is raised to the point where they either efficiently evaporate or sublime. Whereas metals essentially evaporate as atoms and occasionally as clusters of atoms, the same is not true of compounds. Very few inorganic compounds evaporate without molecular change and, therefore, the vapor composition is usually different from that of the original solid or liquid source. As a consequence the stoichiometry of the film deposit will generally differ from that of the source [64, 65]. Disadvantages of resistively heated evaporation sources include contamination by crucibles, heaters, and support materials and the limitation of relatively low input power levels. This makes it difficult to deposit pure films or evaporate high-melting-point materials at appreciable rates.

Electron beam (e-beam) heating eliminates these disadvantages and has, therefore, become the preferred vacuum evaporation technique for depositing films. In principle, this type of source enables evaporation of virtually all materials over a wide range of practical deposition rates. The evaporant is placed in either a water-cooled crucible or in the depression of a water-cooled copper hearth. The purity of the evaporant is assured because only a small amount of material melts or sublimes so that the effective crucible is the unmelted skull material next to the cooled hearth. For this reason there is no contamination of the evaporate by crucible. Multiple source units are available for sequential deposition of more than one material.

Electrodes for ferroelectric capacitors for the present study were deposited using e-beam evaporation.

2.2.2 Sputtering

Sputtering is one of the most versatile techniques used for the deposition of transparent conductors when device quality films are required. Sputtering process produces films with better controlled composition, provides films with greater adhesion and homogeneity and permits better control of film thickness. The sputtering process involves the creation of gas plasma usually an inert gas such as argon [66] by applying voltage between a cathode and anode. The target holder is used as cathode and the anode is the substrate holder. Source material is subjected to intense bombardment by ions. By momentum transfer, particles are ejected from the surface of the cathode and they diffuse away from it, depositing a thin film onto a substrate. Sputtering is normally performed at a pressure of 10^{-2} - 10^{-3} torr.

Normally there are two modes of powering the sputtering system; dc and rf biasing. In dc sputtering system a direct voltage is applied between the cathode and the anode. This method is restricted for conducting targets only. Rf sputtering is suitable for both conducting and non-conducting targets; a high frequency generator (13.56 MHz) is connected between the electrodes of the system. Magnetron sputtering is a process in which a magnetic field is applied at the sputtering target surface. Magnetron sputtering is particularly useful when high deposition rates and low substrate temperatures are required [67].

Both reactive and non-reactive forms of dc, rf and magnetron sputtering have been employed for the deposition of compound semiconductors.

In reactive sputtering, the reactive gas is introduced into the sputtering chamber along with argon to deposit thin films. For example to deposit metal oxide thin films pure metal target is sputtered in a mixture of argon and oxygen atmosphere. The deposition rates and properties of the films strongly depend on the sputtering conditions such as the partial pressure of the reactive gas, the sputtering pressure, substrate temperature and substrate to target spacing.

The process of rf sputter deposition is made possible due to the large difference in mass, and hence mobility, of electrons and inert gas ions. Because electrons are many times less massive than ions, electrons attain much greater velocities and travel much further than ions during each cycle of the applied rf voltage waveform. Since electrons travel much further, they eventually accumulate on the target, substrate and chamber walls such that the plasma is the most positive potential in the system. These induced negative voltages or "sheath voltages", cause acceleration of positive ions toward the negatively charged surfaces, which subsequently leads to sputtering events. The volume adjacent to a surface tends to be relatively free of electrons because of the negatively charged surface. This leads to a "dark space" because electrons are not available to excite gas atoms [68]. A schematic diagram of the rf sputtering system used for the film growth is shown in figure 2.1.

The target is selectively sputtered by controlling the relative surface areas of the target and the substrate holder. If space charge limited current is assumed, the ion current flux, J can be estimated by the Child - Langmuir equation 2.1 [69],

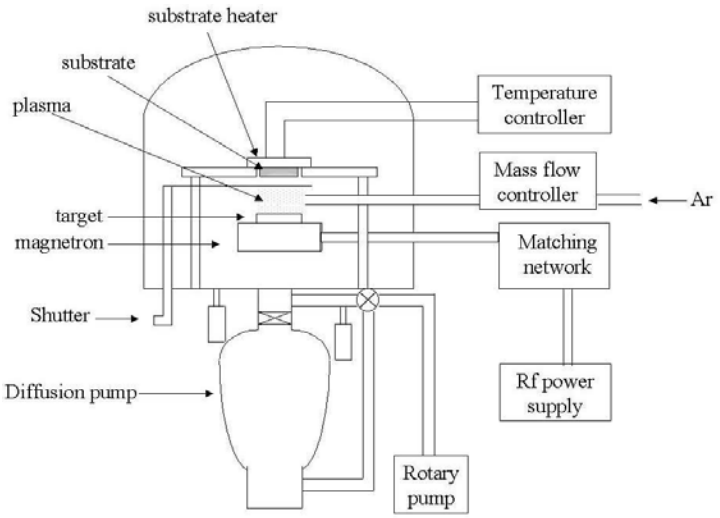

Figure 2.1: Schematic sketch of rf sputter deposition system

$$J = \frac{KV^{3/2}}{D^2 m_{ion}} \tag{2.1}$$

Where D is the dark space thickness, V is the sheath voltage, m_{ion} is the ionic mass and K is the proportionality constant. Since the positive ion current must be equal at both the electrodes,

$$\frac{A_A V_A^{3/2}}{D_A^2} = \frac{A_B V_B^{3/2}}{D_B^2} \tag{2.2}$$

Where A_A and A_B are the surface areas of electrodes A and B respectively. It should be noted that this step differs from the assumption of treating the positive ion current densities equal. If the positive ion current densities were equal, there would be a much greater positive ion current

flowing during one half cycle of the applied voltage waveform than the other due to the much greater area of the grounded substrate electrode. Therefore, because this system is assumed to be in steady state, the total positive ion current per half cycle should be the relevant quantity.

The glow discharge itself is a region where large quantities of positive and negative charge exist and can be modelled as a wire. Since most of the voltage in the glow discharge is dropped across the dark space, and they have small conductivities, they can be modelled as capacitors such that the capacitances,

$$C \propto \frac{A}{D} \tag{2.3}$$

Furthermore, an ac voltage will divide across two series capacitors such that,

$$\frac{V_A}{V_B} = \frac{C_B}{C_A} \tag{2.4}$$

From equations 2.1, 2.2, 2.4

$$\frac{V_A}{V_B} = [\frac{A_B}{A_A}]^2 \tag{2.5}$$

Equation 2.5 tells that smaller area will see larger sheath voltage, whereas larger area will see a smaller sheath voltage by a power of 2. The usefulness of this result is that $A_B > A_A$ must hold to selectively sputter the target. This is done in practice by grounding the substrate holder to the entire chamber resulting in a very large A_B. For this reason it is extremely important that the substrate holder and the system are well grounded to ensure that resputtering of the growing film does not occur.

Sputtering yield is defined as the quantity of the material sputtered per ion (atoms/ion or grams/ion) [70]. To measure the sputtering yield accurately, we need to measure three experimental parameters namely the crater volume (cm^3) formed by sputtering, the ion current (A) and the sputtering time (sec).

Main features observed for the sputtering techniques are

1. Sputtering yield is different for different elements. Sputtering yield increases as the reciprocal of the binding energy of the surface atoms.

2. Sputtering yield decreases as the surface damage increases i.e. the sputtering yield of rough surface is lower than that of smooth surface.

3. As the mass of the sputtering species increases, the sputtering yield increases.

4. Light mass ions penetrate deeper into the target than heavier mass ions.

5. As sputtering energy increases, the sputtering yield increases up to 10 -100 keV. At higher energies, the sputtering yield again decreases since the ions penetrate into the target.

6. Since smaller particles penetrate further into the target, the energy when the yield starts to decrease is lower for lighter particles.

7. For multicomponent samples, the light weight particle is usually preferentially sputtered if the binding energies of the components are similar. The sputtering rate of each component increases as the reciprocal of the binding energy and mass of that component.

8. Sputtering of oxide targets result in preferential depletion of oxygen.

9. Sputtering yield of metal oxide is less than the sputtering yield of corresponding metals.

10. For oxide samples, sputtering in an oxygen rich environment decreases the sputtering yield; the sputtering yield does not vary in other environments (e.g. CO, N_2) indicating that adsorption without chemical bonding is not enough to reduce the sputtering yield.

Sierra Applied Sciences, (USA) make magnetron was used for the rf sputtering of BST thin films. The vacuum system consists of a six-inch diameter diffusion pump backed by a rotary pump (make - HindHivac, Bangalore). The rf supply was connected to the magnetron through a capacitive matching network (make-Huttinger Electronic, Germnay). The flow of argon gas and oxygen into the vacuum chamber was controlled using mass flow controllers (make Aalborg, USA).

2.2.3 Pulsed laser deposition (PLD)

The laser is a source of energy in the form of monochromatic and coherent photons, enjoying ever increasing popularity in diverse and broad applications. In many areas such as metallurgy, medical technology and electronic industry, the laser has become an irreplaceable tool. In material science also lasers play a significant role either as a passive component for process monitoring or as an active tool by coupling its radiation energy to the material being processed, leading to various applications such as localized melting during optical pulling, laser annealing of semiconductors, surface cleaning by desorption and ablation, laser induced rapid quench to improve surface

hardening and most recently pulsed laser deposition for growing thin films [2].

Pulsed laser deposition (PLD) is clearly emerging as one of the premier thin film deposition technologies. PLD has gained a great deal of attention in the past few years for its ease of use and success in depositing materials of complex stoichiometry. PLD was the first technique used to successfully deposit the superconducting $YBa_2Cu_3O_{7-d}$ thin film. Since that time, many materials that are normally difficult to deposit by other methods, especially multi-element oxides, have been successfully deposited by PLD. In the case of multielemental compounds such as high temperature superconductors, ferroelectrics and for electro optic materials, this technique is extremely successful. This technique offers many potential applications, from integrated circuits and optoelectronics to micro mechanics and medical implants [71].

The best quality films can be deposited by controlling the substrate temperature (T), the relative and absolute arrival rates of atoms (R) and the energy of the depositing flux (E). PLD offers the best control over these parameters than other vacuum deposition techniques [2]. A schematic diagram of a simple PLD technique is shown in figure 2.2. In its simplest configuration, a high-power laser situated outside the vacuum deposition chamber is focused by means of external lenses onto the target surface, which serves as the evaporation source. PLD relies on a photon interaction to create an ejected plume of material from any target. The vapor (plume) is collected on a substrate placed at a short distance from the target. Though the actual physical processes of material removal are quite complex, one can consider the ejection of material to occur due to rapid explosion of the target surface due to superheating. Unlike thermal evapora-

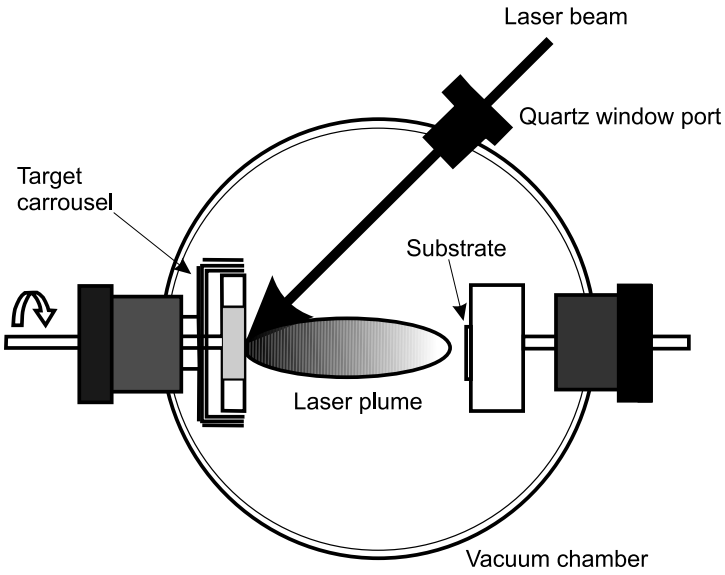

Figure 2.2: Schematic diagram of a PLD setup

tion, which produces a vapor composition dependent on the vapor pressures of elements in the target material, the laser-induced expulsion produces a plume of material with stoichiometry similar to the target.

The main advantage of PLD derives from the laser material removal mechanism. It is generally easier to obtain the desired film stoichiometry for multi-element materials using PLD than with any other deposition techniques. Typical plasma temperature measured by emission spectroscopy during initial expansion is 10,000 K, which is well above the boiling point of most materials (3000 K). Heating of the plasma to these temperatures is thought to occur by inverse-Bremsstrahlung absorption of the laser light in a free - free transition of electron ion pair. This high temperature would evaporate the surface layer of the target thereby replicating exact compo-

sition in the thin films.

Mechanisms of PLD

Pulsed laser deposition is a very complex physical phenomenon involving laser-material interaction under the impact of high-power pulsed radiation on solid target, and formation of plasma plume with highly energetic species. The thin film formation process in PLD generally can be divided into the following four stages.

1. Interaction of laser radiation with the target material.
2. Dynamics of the ablated materials.
3. Deposition of the ablated materials on the substrate.
4. Nucleation and growth of the thin film on the substrate surface.

In the first stage, the laser beam is focused onto the surface of the target. At sufficiently high flux densities and short pulse duration, all elements in the target are rapidly heated up to their evaporation temperature. Materials are dissociated from the target surface and ablated out with stoichiometry as in the target. The instantaneous ablation rate is highly dependent on the fluences of the laser shining on the target. The ablation mechanisms involve many complex physical phenomena such as collisional, thermal, and electronic excitation, exfoliation and hydrodynamics.

During the second stage the emitted materials tend to move towards the substrate according to the laws of gas-dynamic and show the forward peaking phenomenon. The spot size of the laser and the plasma temperature has significant effects on the deposited film uniformity. The target-to-substrate

distance is another parameter that governs the angular spread of the ablated materials. A mask placed close to the substrate could reduce the spreading.

The third stage is important to determine the quality of thin film. The ejected high-energy species impinge onto the substrate surface and may induce various type of damage to the substrate. These energetic species sputter some of the surface atoms and a collision region is formed between the incident flow and the sputtered atoms. Film grows after a thermalized region is formed. The region serves as a source for condensation of particles. When the condensation rate is higher than the rate of particles supplied by the sputtering, thermal equilibrium condition can be reached quickly and film grows on the substrate surface at the expenses of the direct flow of the ablation particles and the thermal equilibrium obtained.

The effect of increasing the energy of the adatoms has a similar effect of increasing substrate temperature on film growth [2]. Typical power densities involved in PLD are approximately 50MWcm^{-2} for a reasonable growth rate. ($>$ 1 A^0/shot) If plasma is formed during laser target interaction in vacuum or in air then an explicit laser - plasma interaction occurs. Due to which ions in the plasma are accelerated to as much as 100 - 1000 eV [2]. Nucleation and growth of crystalline films depends on many factors such as the density, energy, ionization degree, and the type of the condensing material, as well as the temperature and the physico-chemical properties of the substrate. The two main thermodynamic parameters for the growth mechanism are the substrate temperature T and the supersaturation D$_m$. They can be related by the following equation

$$D_m = kTln(R/R_e) \tag{2.6}$$

where k is the Boltzmann constant, R is the actual deposition rate, and R_e is the equilibrium value at the temperature T.

The nucleation process depends on the interfacial energies between the three phases present - substrate, the condensing material and the vapor. The critical size of the nucleus depends on the driving force, i.e. the deposition rate and the substrate temperature. For the large nuclei, a characteristic of small supersaturation, they create isolated patches (islands) of the film on the substrate, which subsequently grow and coalesce together. As the supersaturation increases, the critical nucleus shrinks until its height reaches to atomic diameter and its shape is that of a two-dimensional layer. For large supersaturation, the layer-by-layer nucleation will happen for incompletely wetted foreign substrates.

The crystalline film growth depends on the surface mobility of the adatom (vapor atoms). Normally, the adatom will diffuse through several atomic distances before sticking to a stable position within the newly formed film. The surface temperature of the substrate determines the adatom's surface diffusion ability. High temperature favours rapid and defect free crystal growth, whereas low temperature or large supersaturation crystal growth may be overwhelmed by energetic particle impingement, resulting in disordered or even amorphous structures.

The mean thickness (N_{99}) at which the growing thin and discontinuous film reaches continuity, is given by the equation 2.7

$$N_{99} = A(1/R)^{1/3} exp^{-1/T} \tag{2.7}$$

where R is the deposition rate (supersaturation related) and T is the temperature of the substrate and A is a constant related to the materials

[2]. In the PLD process, due to the short laser pulse duration (10 ns) and hence the small temporal spread ($\leq$10 ms) of the ablated materials, the deposition rate can be enormous (10 nm/s). Consequently a layer by layer nucleation is favoured and ultra-thin and smooth film can be produced. In addition the rapid deposition of the energetic ablation species helps to raise the substrate surface temperature. In this respect PLD tends to demand a lower substrate temperature for crystalline film growth.

In the present study the fourth harmonics (266nm) of Nd:YAG laser (Spectra Physics model GCR 150) is used for ablation.

2.3 Characterization tools

The optimisation of the preparation conditions is the main task in order to get device quality films. This has to be carried out on the basis of detailed structural, compositional, morphological, optical and electrical properties of the films obtained at different growth conditions. In the following sections the techniques used for the film characterizations are discussed briefly.

2.3.1 Film Thickness measurements

Thickness is one of the most important thin film parameter to be characterized since it plays an important role in the film properties unlike a bulk material. Microelectronic applications generally require the maintenance of precise and reproducible film metrology (i.e., thickness as well as lateral dimensions). Various techniques are available to characterize the film thickness which are basically divided into optical and mechanical methods, and are usually nondestructive but sometimes destructive in nature.

Film thickness may be measured either by in-situ monitoring the rate of deposition or after the film deposition.

The stylus profiler takes measurements electromechanically by moving the sample beneath a diamond tipped stylus. The high precision stage moves the sample according to a user defined scan length, speed and stylus force. The stylus is mechanically coupled to the core of a linear variable differential transformer (LVDT). The stylus moves over the sample surface. Surface variations cause the stylus to be translated vertically. Electrical signals corresponding to the stylus movement are produced as the core position of the LVDT changes. The LVDT scales an ac reference signal proportional to the position change, which in turn is conditioned and converted to a digital format through a high precision, integrating, analog-to-digital converter [72]. The film whose thickness has to be measured is deposited with a region masked. This creates a step on the sample surface. Then the thickness of the sample can be measured accurately by measuring the vertical motion of the stylus over the step.

The thicknesses of the thin films prepared for the work presented in this thesis were measured by a stylus profiler (Dektak 6M). Several factors which limit the accuracy of stylus measurements are [64]

1. Stylus penetration and scratching of films (makes problem in very soft films)

2. Substrate roughness. Excessive noise is introduced into the measurement as a result of substrate roughness and this creates uncertainty in the position of the step.

3. Vibration of the equipment. Proper shock mounting and rigid supports are essential to minimise background vibrations.

In modern instruments the leveling and measurement functions are computer controlled. The vertical stylus movement is digitized and data can be processed to magnify areas of interest and yield best profile fits. Calibration profiles are available for standardization of measurements.

2.3.2 Structural Characterization

X-ray diffraction

Electrical and optical properties of the thin films are influenced by the crystallographic nature of the films. X-ray diffraction (XRD) studies were carried out to study the crystallographic properties of the thin films. A given substance always produces a characteristic x-ray diffraction pattern whether that substance is present in the pure state or as one constituent of a mixture of substances. This fact is the basis for the diffraction method of chemical analysis. The particular advantage of x-ray diffraction analysis is that it discloses the presence of a substance and not in terms of its constituent chemical elements. Diffraction analysis is useful whenever it is necessary to know the state of chemical combination of the elements involved or the particular phase in which they are present. Compared with ordinary chemical analysis the diffraction method has the advantage that it is much faster, requires only very small quantity of the sample and is non destructive [69].

The basic law involved in the diffraction method of structural analysis is the Bragg's law. When monochromatic x-rays impinge upon the atoms in a crystal lattice, each atom acts as a source of scattering. The crystal lattice acts as series of parallel reflecting planes. The intensity of the reflected beam at certain angles will be maximum when the path difference between

two reflected waves from two different planes is an integral multiple of λ. This condition is called Bragg's law and is given by the relation 2.8,

$$2dsin\theta = n\lambda \tag{2.8}$$

where n is the order of diffraction, λ is the wavelength of the x-rays, d is the spacing between consecutive parallel planes and θ is the glancing angle (or the complement of the angle of incidence)[73].

X-ray diffraction studies give a whole range of information about the crystal structure, orientation, average crystalline size and stress in the films. Experimentally obtained diffraction patterns of the sample are compared with the standard powder diffraction files published by the International Centre for Diffraction Data (ICDD).

The average grain size of the film can be calculated using the Scherrer's formula 2.9 [69],

$$d = \frac{0.9\lambda}{\beta cos\theta} \tag{2.9}$$

where, λ is the wavelength of the x-ray and β is the full width at half maximum intensity in radians. The lattice parameter for crystallographic systems in the present study can be calculated from the following equations using the (hkl) parameters and the interplanar spacing d.

Cubic system,

$$\frac{1}{d^2} = \frac{h^2 + k^2 + l^2}{a^2} \tag{2.10}$$

Tetragonal system,

$$\frac{1}{d^2} = \frac{h^2 + k^2}{a^2} + \frac{l^2}{c^2} \tag{2.11}$$

Hexagonal system,

$$\frac{1}{d^2} = \frac{4}{3}(\frac{h^2 + hk + k^2}{a^2}) + \frac{l^2}{c^2} \tag{2.12}$$

X-ray diffraction measurements of the films in the present studies were carried out using Rigaku automated x-ray diffractometer. The filtered copper K_α (λ =1.5418A^0) radiation was used for recording the diffraction pattern

Raman Spectroscopy

Raman spectroscopy is a technique that can detect both organic and inorganic species and measure the crystallanity of solids. Raman spectroscopy is based on the Raman effect, first reported by Raman in 1928 [74]. If the incident photon imparts part of it's energy to the lattice in the form of a phonon it emerges as a lower energy photon. This down converted frequency shift is known as Stokes-shifted scattering. Anti stokes shifted scattering results when the photon absorbs a phonon and emerges with higher energy. The anti-Stokes mode is much weaker than the Stokes mode and it is the Stokes-mode scattering that is usually monitored. In Raman spectroscopy a laser beam, referred to as the pump, is incident on the sample. The weak scattered light or the Raman signal is passed through a double monochromator to reject the Raleigh scattered light and the Raman shifted wavelengths are detected by a photodetector. Various properties of the semiconductors, mainly composition and crystal structure can be determined. The Stokes line shifts and broadening becomes asymmetric for microcrystalline Si with grain sizes below 10 nm [75]. The lines become very broad for amorphous semiconductors, allowing distinction to be made between single crystal, polycrystalline, and amorphous materials.

In the present work, Raman studies was carried out with micro Raman (Jobin Yvon Horiba) with argon ion laser (488 nm) as the excitation source .

2.3.3 Composition analysis

The stoichiometry of the deposited film were studied using the compositional analysis and some of the characterization tools used in the present investigation are described below.

EDX

EDX/EDAX or energy dispersive x-ray analysis is a technique used for identifying the elemental composition of the specimen, on an area of interest thereof. The EDX analysis system works as an integrated feature of a scanning electron microscope (SEM), and can not operate on its own without the latter [76, 77].

During EDX analysis, the specimen is bombarded with an electron beam inside the scanning electron microscope. The bombarding electrons collide with the specimen atom's own electrons, knocking some of them off in the process. A position vacated by an ejected inner shell electron is eventually occupied by a higher-energy electron from an outer shell. To be able to do so, however, the transferring outer electron must give up some of its energy by emitting an x-ray. The amount of energy released by the transferring electron depends on which shell it is transferring from, as well as which shell it is transferring to. Furthermore, the atom of every element releases x-rays with unique amounts of energy during the transferring process. Thus, by measuring the energy of the x-rays emitted by a specimen during electron

beam bombardment, the identity of the atom from which the x-ray was emitted can be established. The output of an EDX analysis is an EDX spectrum, which is a plot of how frequently an x-ray is received for each energy level.

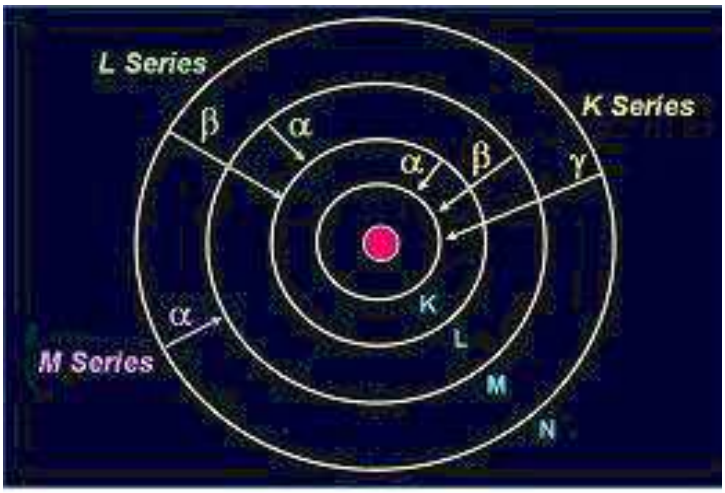

Figure 2.3: The emission of x-rays

An EDX spectrum normally displays peaks corresponding to the energy levels for which the most x-rays had been received. Each of these peaks are unique to an atom, and therefore corresponds to a single element. The higher the intensity of a peak in a spectrum, the more concentrated the element is in the specimen. An EDX spectrum plot not only identifies the element corresponding to each of its peaks, but the type of x-ray to which it corresponds as well. For example, a peak corresponding to the amount of energy possessed by x-rays emitted by an electron in the L-shell going down to the K-shell is identified as a K_α peak. The peak corresponding to

x-rays emitted by M-shell electrons going to the K-shell is identified as a K_β peak as shown in figure 2.3

The composition analysis of BST and PZT thin films were carried out using EDX technique

XPS

X-ray photoelectron spectroscopy (XPS)is also known as electron spectroscopy for chemical analysis or ESCA. In XPS, radiation from an x-ray source strikes the sample. The deep inner shell electrons are excited and both core and valence band electrons are ejected with characteristic energy and release of x-ray photoelectrons [76].

Depending on the atomic structures, the wavelength of the x-ray will be different. Electrons emitted from atoms within a few atomic layers of the surface escape and the respective energy analyzed. Results provide quantitative and qualitative information about oxidation states of surface and near-surface atoms, surface impurities, and fundamental interactions between surface species. Standard XPS provides excellent chemical information but restricted spatial data. If, however, a lens with a narrow acceptance angle is placed at the energy analyzer's entrance, small area XPS (SAXPS) provides an image of surface features with a resolution of 280 pm. (figure 2.4).

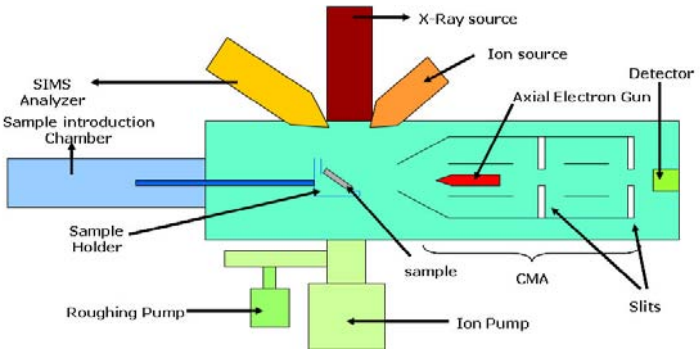

Figure 2.4: Schematic sketch of XPS system

If the x-ray source is monochromatic, the electron's kinetic energy is used to measure its binding energy from the relation x-ray energy minus binding energy equals kinetic energy. The most common source creates x-rays by bombarding either Al or Mg targets with high energy electrons to produce 1486.6eV and 1253.6eV photons, respectively. Increasingly, synchrotron radiation (the tangential photon flux formed when high energy charged particles are deflected) is the source of choice. The photon energy, ranging from infrared to x-ray, is resolved by a monochromator into a monoenergetic, high flux beam that provides much greater experimental flexibility than a fixed frequency x-ray source.

XPS with Al K_α radiation source (1486.6 eV) was used to study the oxygen content in sputtered BST thin films.

2.3.4 Surface analysis

Surface morphology is an important property since roughness of the thin film surface play an important role during device fabrication. Atomic force

microscopy (AFM) and scanning electron microscopy (SEM) used in the present study is described below

AFM

Scanning probe microscopy (SPM) is a fundamentally simple technology that is capable of imaging and measuring surfaces on a fine scale and of altering surfaces at the atomic level. There are three elements common to all probe microscopes.

1. A small, sharp probe. The interactions between the surface and the probe are used to study the surface.

2. A detection system which monitors the product of the probe-surface interaction (e.g., a force, tunneling current, change in capacitance, etc.).

3. Scanning technique: Either the probe or sample is raster-scanned with nanoscale precision. By monitoring the interaction intensity, any surface variation translates to topographical information from the surface and generates a three-dimensional image of the surface.

The most commonly used SPMs are atomic force microscope (AFM) and scanning tunneling microscope (STM). AFM is the most widely used local probe devices. It gives quick access to a wide range of surface properties, including mechanical, electrical, magnetic, and other properties, with good spatial resolution. In AFM, the probe tip is affixed on a cantilever beam. The probe interacts with the surface and the resulting force deflects the beam in a repulsive manner, as described by Hooke's Law. In the same manner that a spring changes dimensions under the influence of forces, the

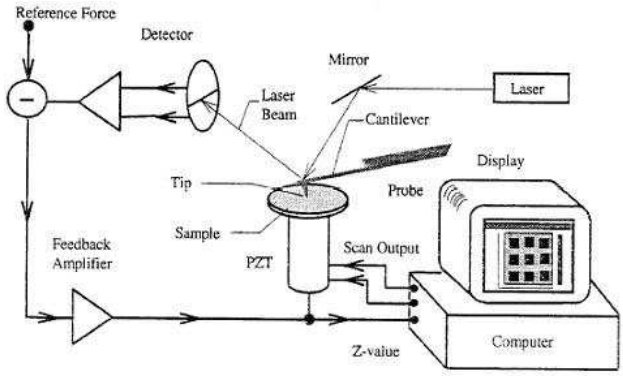

Figure 2.5: Schematic diagram of atomic force microscope.

attractive and repulsive forces between atoms of the probe and the surface can also be monitored when brought extremely close to each other. Hence, the net forces acting on the probe tip deflect the cantilever, and the tip displacement is proportional to the force between the surface and the tip. As the probe tip is scanned across the surface, a laser beam reflects off the cantilever. By monitoring the net (x, y, and z) deflection of the cantilever, a three-dimensional image of the surface is constructed (Figure 2.5).

The AFM typically operates in either of two principal modes: constant-force mode (with feedback control) and constant-height mode (without feedback control). Once the deflection of the cantilever has been detected in the AFM, it can generate the topographic data set by operating in one of the two modes viz constant-height or constant-force mode. In constant-height mode, the spatial variation of the cantilever deflection can be used directly to generate the topographic data set because the height of the scanner is fixed as it scans. In constant-force mode, the deflection of the cantilever can be used as input to a feedback circuit that moves the scanner

up and down in the z-axis, responding to the topography by keeping the cantilever deflection constant. In this case, the image is generated from the scanner's motion. With the cantilever deflection held constant, the total force applied to the sample is constant. The biggest advantage of AFM is that most samples can be investigated in their natural state, including biological samples (even in an aqueous environment), which is otherwise impossible by electron microscopy methods.

SEM

The scanning electron microscope (SEM) is a microscope that uses electrons rather than light to form an image. There are many advantages for using the SEM instead of a light microscope [76]. The SEM has a large depth of field, which allows a large amount of the sample to be in focus at the same time. The SEM also produces images of high resolution, which means that closely spaced features can be examined at a high magnification. Preparation of the samples is relatively easy since most SEMs only require that sample should be conductive.The combination of higher magnification, larger depth of focus, greater resolution, and ease of sample observation makes SEM one of the most heavily used instruments in the research field. The electron beam comes from a filament, made of various types of materials.

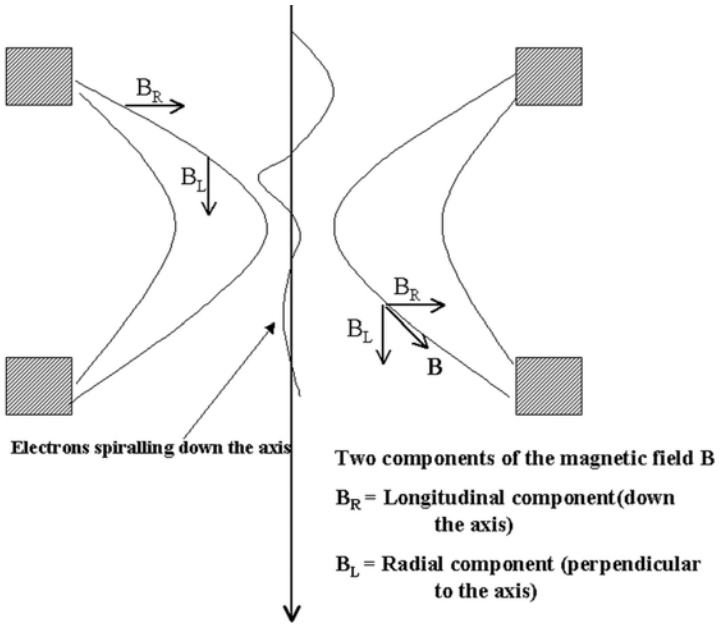

Figure 2.6: The focusing of electrons in SEM

The most common is the tungsten hairpin gun. This filament is a loop of tungsten that functions as the cathode. A voltage is applied to the loop, causing it to heat up. The anode, which is positive with respect to the filament, forms powerful attractive forces for electrons. This causes electrons to accelerate toward the anode. The anode is arranged, as an orifice through which electrons would pass down to the column where the sample is held. Other examples of filaments are lanthanum hexaboride filaments and field emission guns.

The streams of electrons that are attracted through the anode are made to pass through a condenser lens, and are focused to very fine point on the sample by the objective lens (figure 2.6). The electron beam hits the

sample, producing secondary electrons from the sample. These electrons are collected by a secondary detector or a backscatter detector, converted to a voltage, and amplified. The amplified voltage is applied to the grid of the CRT that causes the intensity of the spot of light to change. The image consists of thousands of spots of varying intensity on the face of a CRT that correspond to the topography of the sample.

In the present study, JEOL JSM 5600 was used for SEM analysis. Cross sectional SEM is also taken for thin films deposited on oxide substrates.

2.3.5 Optical analysis

Optical band gap

An important technique for measuring the band gap of a semiconductor is by studying the absorption of incident photons by the material. In this, photons of selected energy are directed to the sample and the relative transmission of the various photons is observed. Since photons with energies greater than the band gap energy are absorbed while photons with energies less than band gap energy are transmitted, the experiment gives an accurate measure of band gap [78].

According to Bardeen et al. [79] for the parabolic band structure, the relation between the absorption coefficient (α) and the band gap of the material is given by,

$$\alpha = [\frac{A}{h\nu}](h\nu - E_g)^{\gamma} \tag{2.13}$$

where, γ =1/2 for allowed direct transitions, γ =2 for allowed indirect transitions, γ =3 for forbidden indirect transitions and γ =3/2 for forbidden direct transitions. A is the parameter which depends on the transition

probability. The absorption coefficient can be deduced from the absorption or transmission spectra using the relation,

$$I = I_0 e^{-(\alpha)t} \tag{2.14}$$

where, I is the transmitted intensity and I_0 is the incident intensity of the light and t is the thickness of the film. In the case of direct transition, $(\alpha \text{ h } \nu)^2$ will show a linear dependence on the photon energy ($h\nu$). A plot of $(\alpha \text{ h } \nu)^2$ against $h\nu$ will be a straight line and the intercept on energy axis at $(\alpha \text{ h } \nu)^2$ equal to zero will give the band gap.

Determination of optical constants

The optical constants, the refractive index (n) and the extinction coefficient (k) of the films are calculated using the methoed developed by Manificer et al. [80] for weakly absorbing films

The following method can be used for determining the optical constants. If the incident light has unit amplitude then the amplitude of the transmitted wave is

$$A = \frac{t_1 t_2 e^{-2\pi n^* t \ \lambda}}{1 + r_1 r_2 e^{-4\pi n^* t \ \lambda}} \tag{2.15}$$

Where t_1, t_2 , r_1 and r_2 are the transmission and reflection coefficients of the front and rear surfaces of the film respectively and are given by

$$t_1 = \frac{2n_0}{n_0 + n} t_2 = \frac{2n}{n_1 + n} r_1 = \frac{n_0 - n}{n_0 + n} r_2 = \frac{n - n_1}{n_1 + n} \tag{2.16}$$

n_0 , n and n_1 are the refractive indices of the substrate, film and the medium respectively

Transmission coefficient of the layer is

$$T = \frac{n_1}{n_0} A^2 \tag{2.17}$$

If we consider the case of normal incidence and weak absorption (where $k^2 \ll (n - n_0)^2$ and $k^2 \ll (n - n_1)^2$.

Transmission coefficient is given by

$$T = \frac{16 n_0 n_1 n^2 \alpha_1}{c_1^2 + c_2^2 \alpha_1^2 + 2 c_1 c_2 \alpha_1 cos 4\pi t\ \lambda} \tag{2.18}$$

$$c_1 = (n + n_0)(n + n_1) \tag{2.19}$$

$$c_2 = (n - n_0)(n_1 - n) \tag{2.20}$$

$$\alpha_1 = (-4\pi k t/\lambda) = e^{-\alpha t} \tag{2.21}$$

Here α is the absorption coefficient of the thin film, t is the thickness, k is the extinction coefficient and λ is the wavelength of light.

The extreme values of T are

$$T_{max} = \frac{16 n_0 n_1 n^2 \alpha_1}{(c_1 + c_2 \alpha_1)^2} \tag{2.22}$$

$$T_{min} = \frac{16 n_0 n_1 n^2 \alpha_1}{(c_1 - c_2 \alpha_1)^2} \tag{2.23}$$

where

$$n = [N + (N^2 - n_0^2 n_1^2)^{1/2}]^{1/2} \tag{2.24}$$

$$N = n_0^2 + n_1^2 + 2 n_0 n_1 [\frac{T_{max} - T_{min}}{T_{max} T_{min}}] \tag{2.25}$$

Knowing T_{max}, T_{min}, n_0 and n_1 at the same wavelength refractive index(n) of the film can be calculated. The refractive index of BST thin films were calculated using the above relation.

Diffuse reflectance spectroscopy

The measurement of diffused radiation reflected from a surface constitutes the area of spectroscopy known as diffuse reflectance spectroscopy. Diffuse reflectance spectrometry concerns one of the two components of reflected radiation from an irradiated sample, namely specular reflected radiation, R_s and diffusely reflected radiation, R_d . The former component is due to the reflection at the surface of single crystallites while the latter arises from the radiation penetrating into the interior of the solid and re-emerging to the surface after being scattered numerous times. These spectra can exhibit both absorbance and reflectance features due to contributions from transmission, internal and specular reflectance components as well as scattering phenomena in the collected radiation. Based on the optical properties of the sample, several models have been proposed to describe the diffuse reflectance phenomena. The Kubelka-Munk model put forward in 1931 is widely used and accepted in diffuse reflectance infrared spectrometry. The intensity of the reflected light depends on the scattering coefficient s and the absorption coefficient k. The reflectance data can be converted to absorbance by Kubelka-Munk equation [81, 82]. Kubelka-Munk equation is as

$$Log[(\frac{1-r)^2}{2r}] = Logk - Logs \tag{2.26}$$

Where r = $\frac{R(sample)}{R(standard)}$

Here the standard used is $BaSO_4$. R (standard) is taken as unity. R (sample) is the diffuse reflectance of the sample

(R= I_{sam}/I_{ref}).

Equation 2.26 Implies,

$$\frac{(1-R)^2}{2R} = \frac{k}{s} \tag{2.27}$$

The band gap is estimated from the plot of $((k/s).h\nu)^2$ vs $h\nu$ ($h\nu$ is the photon energy) by extrapolating the graph to the x axis. DRS was recorded using Jasco V 570 spectrophotometer in the present studies.

Photoluminescence

Luminescence in solids is the phenomenon in which electronic states of solids are excited by photons from an external source and the excited states release energy as electromagnetic radiation. When short wavelength radiation illuminate a solid and result in the emission of higher wavelength, the phenomenon is called photoluminescence (PL) [83]. PL is divided into two major types: Intrinsic and extrinsic depending on the nature of electronic transition producing it.

Intrinsic luminescence are of three kinds

1. band to band luminescence
2. exciton luminescence
3. cross-luminescence.

Band to band luminescence: Luminescence owing to the band-to-band transition, ie to the recombination of an electron in the conduction band with a hole in the valance band, can be seen in pure crystal at relatively high temperature. This has been observed in Si,Ge and IIIb-Vb compounds such as GaAs.

Exciton luminescence: An exciton is a composite particle of an excited electron and a hole interacting with one another. It moves in a crystal

conveying energy and produces luminescence owing to the recombination of the electron and the hole. There are two kinds of excitons: Wannier exciton and Frenkel exciton. The Wannier exciton model express an exciton composed of an electron in the conduction band and a hole in the valence band bound together by couloumb interaction. The expanse of the wave function of the electron and hole in Wannier exciton is much larger than the lattice constant. The exciton in IIIb-Vb and IIb-VIb compounds are examples for Wannier exciton. The Frenkel exciton model is used in cases where expanse of electron and hole wave function is smaller than lattice constant. The excitons in organic molecular crystals are examples of Frenkel exciton.

Cross luminescence: Cross luminescence is produced by the recombination of an electron in the valance band with a hole created in the outer most core band. This is observed in number of alkali and alkaline-earth halides and double halides. This takes place only when the energy difference between the top of valance band and that of conduction band is smaller than the band gap energy. This type of luminescence was first observed in BaF_2.

Extrinsic luminescence: Luminescence caused by intentionally incorporated impurities, mostly metallic impurities or defects is classified as extrinsic luminescence. Most of the observed type of luminescence of practical application belongs to this category. Intentionally incorporated impurities are activators and materials made luminescent in this way are called phosphors. Extrinsic luminescence in ionic crystals and semiconductors is classified into two types: unlocalized and localized. In the unlocalized type, the electrons and holes of the host lattice participate in the luminescence process, while in localized type the luminescence excitation and emission process are confined in a localized luminescence center.

Two types of luminescence spectra can be distinguished: excitation and emission. In the case of an excitation spectrum the wavelength of the exciting light is varied and the intensity of the emitted light at a fixed emission wavelength is measured as a function of the excitation wavelength. The excitation spectrum gives information on the position of excited states just as the absorption spectrum does, except that the former reveals only the absorption bands that result in the emission of light. The observed differences between the absorption and excitation spectra can yield useful information. An emission spectrum provides information on the spectral distribution of the light emitted by a sample. The time resolved PL measurements are a powerful tool for the determination of the radiative efficiency. The radiative efficiency specifies the fraction of excited states, which de-excite by emitting photons [83].

The emission and excitation spectra for the BST:Eu thin films are recorded using Jobin Yvon Fluorimeter -3 spectroflurometer.

Nonlinear absorption

A single beam Z-scan technique was employed (figure2.7) for nonlinear absorption and nonlinear refraction measurements at room temperature.

A single Gaussian laser beam in tight focus geometry as depicted in figure 2.7 was used to measure the absorption and refraction of a medium in the far field as a function of the sample position z measured with respect to the focal plane. A beam splitter was used to get the transmitted and the reference beam simultaneously. If part of the light intensity transmitted across the nonlinear material is measured through an aperture in front of the detector(closed Z-scan), the magnitude and sign of the nonlinear refrac-

tive index is obtained. If all the transmitted beam is detected without the aperture (open aperture Z-scan), the nonlinear absorption can be obtained.

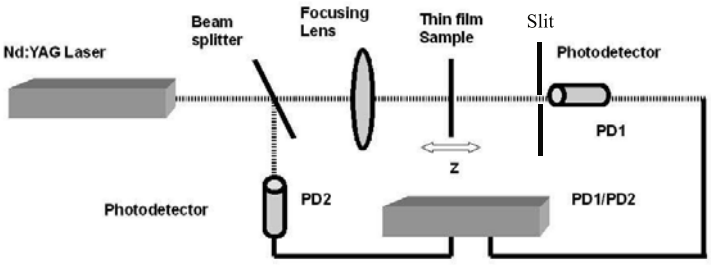

Figure 2.7: Single beam Z-scan set up

The open aperture Z-scan curve comprises a normalised transmittance as a result of nonlinear absorption. The experimental data is fitted with the theoretical values. The theoretical equation for normalised transmittance T, for two photon absorption at a given position of the sample z, is given by equation 2.28 [84].

$$T(z, S = 1) = (1/\sqrt{\pi}) q_0(Z, 0) \int [ln(1 + q_0(Z, 0)) e^{-\tau^2}] d\tau \tag{2.28}$$

Where q_0(Z,t) is the fitting parameter given by equation (2.29), S=1 for open aperture

$$q_0(Z, t) = \frac{\beta I_0(t) L_{eff}}{(1 + z^2/z_0^2)} \tag{2.29}$$

β is the nonlinear absorption coefficient, z_0 is the Raleyigh parameter, I_0(t) is the on axis irradiance at the focus L_{eff} is the effective focal length given by equation (2.30).

$$L_{eff} = \frac{(1 - e^{-L\alpha})}{\alpha} \tag{2.30}$$

where L is the sample length and α is the linear absorption coefficient. The experimental curve is theoretically fitted by equation(2.28)and the nonlinear absorption coefficient β is calculated. The imaginary part of third order nonlinear susceptibility $\mathrm{Im}\chi^{(3)}$ is calculated using the equation(2.31) [84]

$$\beta = \frac{3kIm\chi^3}{2\epsilon_0 c n_0} \tag{2.31}$$

Where k = $2\pi/\lambda(\lambda = 532\text{nm})$ ϵ_0 is free space dielectric constant, n_0 is linear refractive index and c the velocity of light.

The on axis phase shift at the focus, $\Delta\phi_0$, can be obtained through the best theoretical fit from the normalised closed aperture transmittance T(z,$\Delta\phi_0$) at the sample position z, by the equation (2.32) [84].

$$T(z, \Delta\phi_0) \approx [1 + \frac{4\Delta\phi_0 x}{(x^2+9)(x^2+1)}] \tag{2.32}$$

where x = $\mathrm{z/z_0}$. The nonlinear refractive index γ and the real part of third order optical nonlinear susceptibility $\mathrm{Re}\chi^{(3)}$ can be given by the following equations (2.33) and (2.34) [84].

$$\gamma = \frac{\lambda\Delta\phi_0}{2L_{eff}I_0} \tag{2.33}$$

$$Re\chi^{(3)} = 2(n_0)^2\varepsilon_0 c\gamma \tag{2.34}$$

where λ = 532nm is the wavelength of laser used, ϵ_0 is free space dielectric constant, n_0 is linear refractive index and c the velocity of light.

In the present study second harmonics of Q switched Nd:YAG laser at 532 nm having a repetition rate of 10 Hz was used as the light source. The focal length of the lens used was 25cm. Using a translation stage the

sample was moved in a spatially varying intensity region on either side of the focused laser beam. The transmitted and reference energies can be measured using probe heads PD_1 and PD_2 of the energy ratio meter. The entire setup is automated using LabVIEW.

2.3.6 Electrical measurements

Thin film capacitors were characterized by various electrical measurements. This includes leakage current, capacitance as a function of frequency and voltage and polarization measurements from hysteresis loop traced by the ferroelectric thin films. Metal as well as oxide electrode are sputter deposited through shadow mask to form thin film capacitors.

Leakage current

The leakage current of the samples were found from the current - voltage (I-V) curve, where the current is measured at a specified voltage. The leakage current is an important characteristic of thin film ferroelectric capacitors, it directly limits the charge retention and it influences the ferroelectric hysteresis loop. The leakage current is also a sensitive electrical probe of the material quality of hetrostructure as it is strongly dependent on material aspects of the ferroelectric film and of electrode-ferroelectric interfaces [15]. Capacitor with low leakage current is ideal for microelectronic device application.

The leakage current for ferroelectric oxide thin films is expressed as

$$J = AT^2 exp \frac{-q((\phi)_b - (qV/4\pi\epsilon_0\epsilon\omega))^{1/2}}{KT} \tag{2.35}$$

J is the leakage current density, A the effective Richardson constant, T the temperature, q the electronic charge, ϕ_b the Schottky barrier height,

V the applied voltage, ϵ_0 the free space dielectric constant, ϵ the dielectric constant of BST, ω the depletion layer width, K the Boltzmann constant.

The current voltage measurements of BST and PZT thin films were carried out using a Keithley‘s source measure unit (Model SMU 236).

Capacitance measurements

The capacitance was measured by fabricating hetrostructures with ferroelectric thin films. Capacitance can be directly measured from an impedance analyser.

The dielectric constant is found using the relation

$$\epsilon = \frac{Cd}{A\epsilon_0} \tag{2.36}$$

Where C is the capacitance in farads, ϵ the free space dielectric constant ($8.85\text{x}10^{-12}\text{Fm}^{-1}$), A is the area of the capacitor and d is the thickness of the ferroelectric thin film. The area of the electrode is 0.25cm^2. In the present study the capacitance - frequency (C-f) and capacitance - voltage (C-V) is measured using an impedence analyser 4192 A HP in the frequency range 1KHz - 1MHz for a bias voltage $\pm$8V .

Polarization measurements

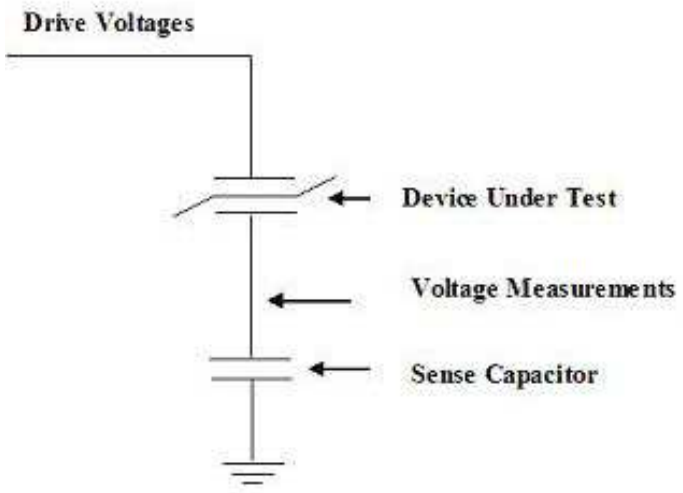

Figure 2.8: Basic Sawyer Tower test configuration for polarization measurements

The hysteresis measurement of the fabricated capacitors were carried out using RT66A ferroelectric tester from Radiant Technologies (Albuquerque, NM). The polarization hysteresis loop can be obtained with the traditional sawyer-tower circuit mode or with a virtual ground mode [85]. The sawyer-tower circuit is composed of linear sense capacitor (Cs) connected in series with Device Under Test (DUT). In this circuit the two capacitors have the same charge on them, and the polarization is obtained by measuring the voltage across the sense capacitor as shown in the figure 2.8. Even though the circuit is simple, the value of the sense capacitor has to be accurate and must have much higher capacitance than the ferroelectric capacitor to obtain accurate results.

The standard way of measuring the hysteresis loop is the virtual ground mode. In the virtual ground measuring system the sense capacitor in the Sawyer Tower circuit is replaced with the measurement circuit shown in figure2.9. In this configuration, the transimpedance amplifier maintains the precision return terminal at a virtual ground potential. All of the charge that follows through the sample as a result of the applied drive voltage is collected by the integrator circuit. The voltage generated on the output of the integrator is then measured and translated into the test results that are displayed by the software. The precision drive and return circuitry are matched with respect to speed and current sinking ability. Thus the precision testers reject errors that might occur when the drive makes a transition faster than the transimpedance amplifier can follow. Therefore a large range of capacitance values over a large range of speeds can be measured accurately.

There are basically two advantages of using the virtual ground measuring system rather than the Sawyer Tower measuring system. In Sawyer Tower measuring system the sense capacitor is susceptible to develop back voltage. When the drive voltage makes the transition to the maximum test voltage and then returns to zero volts, the charge collected in the sense capacitor generates a voltage known as the back voltage, which is applied in the opposite direction to the last drive voltage used to program the DUT. The back voltage may be minimized by the proper selection of the sense capacitor value. If the sense capacitor value is large (10 times) compared to the sample, the voltage across the sense capacitor generated by the charge flow through the sample is small and therefore the back voltage is minimized.

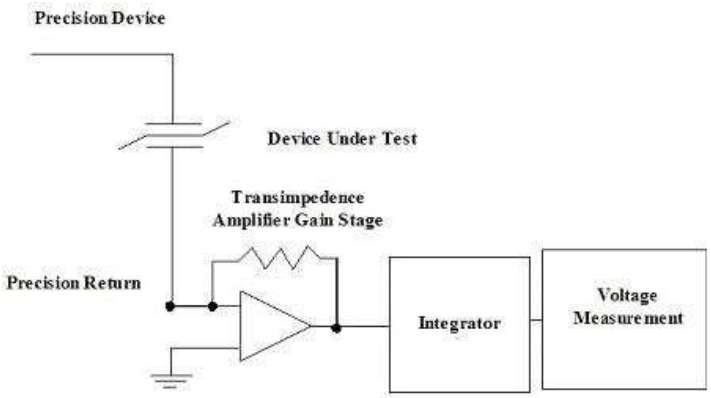

Figure 2.9: Virtual ground measuring system

In the virtual ground measuring system the DUT is never subject to back voltage because the measurement side of the sample that is connected to the return input of the system is "virtually grounded". In the Sawyer Tower measuring system the parasitic capacitance of the measurement circuitry adds in parallel to the sense capacitance value. The accuracy of the Sawyer Tower measurement depends directly on the accuracy of the value of the sense capacitor known. Therefore the parasitic capacitance value can introduce inaccuracy in the measurement if the value of the sense capacitor is not large compared to the parasitic capacitance. But in virtual ground mode the parasitic capacitance is associated with the return terminal. As this terminal is never allowed to gain voltage greater than zero volts the charge build up by the parasitic capacitance is zero. Therefore the parasitics that are associated with the return circuitry is essentially eliminated

Chapter 3

Pulsed laser deposition of PZT and PLZT

A lower growth temperature of PZT films is favored for integration of these films for MEMS application. This chapter gives a detailed account of the work carried for the growth of PZT films at relatively lower substrate temperature. The deposition of PZT on PtSi substrates itself is a challenging task since Pb is highly volatile. The targets used were 2% and 10% excess Pb added to the PZT for maintaining the stoichiometry of the films.La is substituted as donar dopant in PZT to form PLZT. Effect of buffer layer on the structural and electrical properties is also investigated.The use of ZnO buffer layers has reduced the temperature of crystallisation of PZT to 300^0C. The electrical characterizations of the devices is discussed in detail.

3.1 Introduction

Pb-based ferroelectric thin film such as Pb(Zr,Ti)O_3 (PZT)and (Pb,La) (Zr,Ti) O_3 (PLZT) are widely attracted because of their excellent ferroelectric , dielectric, pyroelectric and piezoelectric properties. Piezoelectric lead zirconate titanate (PZT) thin films have been employed extensively in micro actuators for micro electro mechanical system (MEMS). Recently PLZT has got attention because of its potential to integrate with the semiconductor devices. The synthesis of PZT ferroelectric film is difficult. Recently the films of pure perovskite phase were successfully prepared with electrical properties comparable to that of ceramic form but its dielectric constant is inferior to bulk ceramic. The problem originate from the difficulty in the control of composition which is due to the inherent Pb^{2+} ion loss occurring during the thin film deposition. The techniques which have been successful for deposition of PZT on single crystal cannot be applied directly to grow PZT films on silicon or Pt coated substrate. A large portion of pyrochlore phase is always present in thin films grown by sol gel, chemical solution method, laser ablation and sputtering[86–88].

The popular thin film deposition techniques for PZT/PLZT are sol-gel, sputtering, metal-organic chemical vapor deposition (MOCVD) and pulsed laser deposition. For preparing ferroelectric PZT films, magnetron sputtering has conventionally been used. This method has some disadvantages such as low deposition rate and large variation in composition. These disadvantages are overcome in other methods like sol-gel technique, MOCVD and laser ablation. Sol-gel has the advantages of high purity, uniform film thickness and easy control of composition and crystallinity. But a sol-gel derived PZT thin film has problems such as low deposition rate and rela-

tively high crystallization temperature. The PLD technique possesses overwhelming advantage of easiness in control of stoichiometric composition in thin film deposition. It is suitable for growing multicomponent oxide thin films. Further in contrast with sol-gel and MOCVD which require special source materials , the laser ablation can use the ceramic target as a source material[87].

The PZT films of good electrical characteristics can be obtained on Si substrates using PLD technique such as sequential deposition of ZrO_2, TiO_2 and PbO layers [89], direct ablation of PZT target with excess PbO [86], depositing a perovskite buffer layers or post annealing of low temperature deposited films [87].

Most defects in PZT films are due to vacancies of lead and oxygen. PbO is volatile and PZT can accommodate large amounts of lead and oxygen vacancies which can interact with one another. Lead loss is avoided by adding 2% and 10% excess lead to the ablation targets . Oxygen vacancy formation is inhibited by including donor dopants in PZT [90, 91].

In this chapter pulsed laser deposition of PZT/PLZT thin films are described. The chapter is divided into two parts. Section 3.3 focuses on the pulsed laser deposition of PZT/PLZT for obtaining pure perovskite phase. The effect of buffer layer on the microstructure of PZT/PLZT is discussed. Section 3.4 details the electrical characterization of PZT/PLZT ferroelectric devices.

3.2 Experimental Details

The PZT and PLZT targets for PLD is synthesised using solid state reaction of PbO, TiO_2 and ZrO_2. La donar dopant is added to PZT during

material preparation. PZT thin films were ablated using fourth harmonics of Nd:YAG laser (266nm). The repetition frequency was 10Hz with a pulse width of 8-9ns. The laser fluence was kept at $2J/cm^2$.

The target was fixed at an angle 45^0 to the direction of laser beam and it was rotated at a constant rpm during the laser deposition, so that pitting of the target surface by the laser beam will be uniform.The focused energy of the high-energy laser ionises the target material and the 'plume" produced spreads out in the forward direction towards the substrates and it is slightly divergent. The substrate is placed at a distance 4cm to the target surface.The gas (oxygen) is bled into the vacuum chamber continuously at a fixed flow rate, while the chamber is simultaneously pumped to maintain a constant background pressure during deposition. The flow of oxygen ambient gas is controlled by using a mass flow controller.The substrate temperature (T_s) was varied from 300^0C - 600^0C. The oxygen partial pressure in the chamber is 0.15mbar.

The crystallinity of thin films was determined by x ray diffraction (XRD) using CuK_α radiation(λ =1.5418A^0). Thickness of the samples were measured using Dektak 6M surface profiler. The electrical characterization of thin films were carried out using I-V and C-V measurements. The ferroelectric behavior of the films were carried out using Sawyer Tower circuit.

3.3 Pure perovskite phase formation of PZT/PLZT thin films

Figure 3.1 shows the XRD pattern of PZT target used for ablation. The XRD pattern clearly indicates a tetragonal perovskite phase. La substi-

tuted target is also prepared by solid state reaction for depositing PLZT thin films. These targets synthesized in the laboratory have been used for the growth of thin films by PLD.

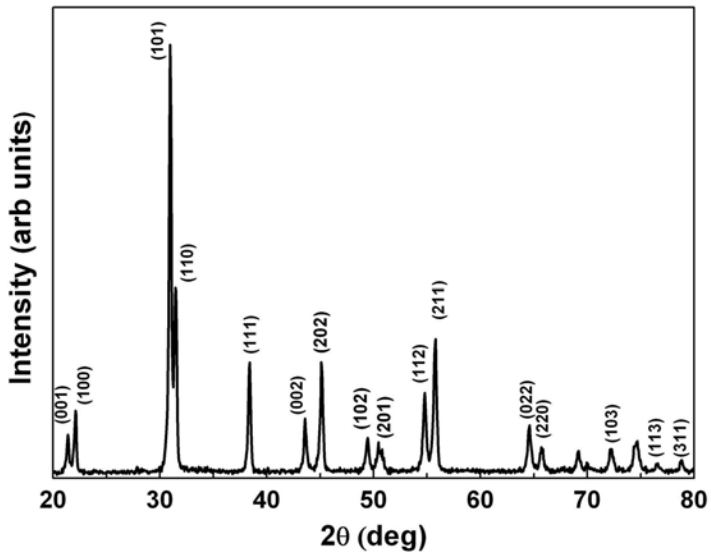

Figure 3.1: The XRD pattern of PZT target

The XRD pattern of the PZT thin films grown by PLD is shown below(figure 3.2).

The PZT thin films were amorphous when deposition was carried out at substrate temperature $T_s < 500^0$C. At a substrate temperature of 500^0C only pyrochlore phase was formed. Pure perovskite phase is obtained at $T_s = 600^0$C without any post deposition treatment.

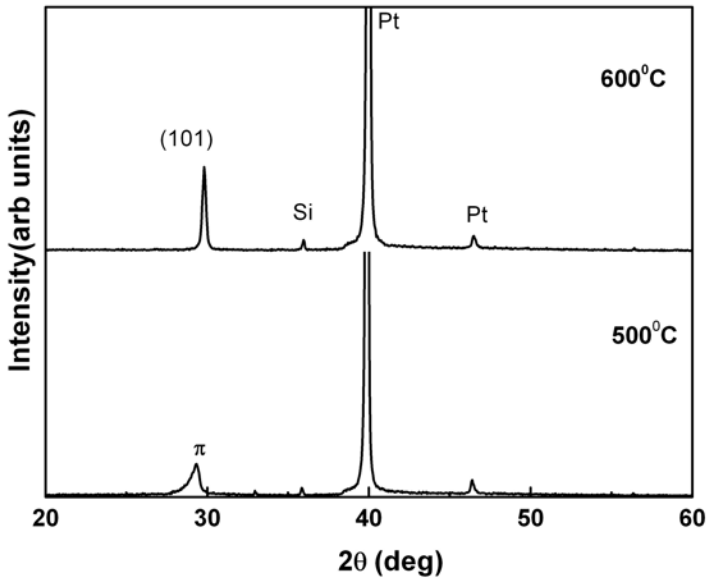

Figure 3.2: The XRD pattern of PZT thin films grown by PLD at different substrate temperature using stoichiometric target (π represents the pyrochlore phase).

Composition analysis of the thin film samples were carried out by EDX measurements. It shows that the films were deficient of Pb^{2+} ions. The Pb/(Ti+Zr) ratio is found to be 0.548 for films deposited at $T_s = 600^0$C even though these films are pure perovskite. During the deposition process much of the lead is lost owing to reduced sticking and accommodation coefficients at elevated substrate temperatures [87]. Hence the PZT target compensated with excess PbO for maintaining stoichiometry in the films. PZT target with 2% and 10% excess Pb is used for depositing PZT thin films were used as the target. XRD pattern of the targets confirms the

tetragonal perovskite phase in the starting material. $Pb_{1.02}Zr_{0.5}Ti_{0.5}O_3$ (P2ZT) and $Pb_{1.1}Zr_{0.5}Ti_{0.5}O_3$) (P10ZT) were used for the growth of thin films by PLD.

XRD pattern of P2ZT and P10ZT on PtSi substrates at different substrate temperature shows the same pattern as that of PZT. The films deposited at $T_s = 600^0$C is crystalline perovskite wheras films deposited at $T_s = 500^0$C showed pyrochlore phase. All the films deposited below 500^0C were amorphous.

The composition analysis of these films shows that the films are stoichiometric when the target is compensated with 2% excess Pb. The ratio Pb/(Zr+Ti) is nearly 1 for films deposited at a substrate temperature of 600^0C.

It is a common practise to include donor dopants in PZT to improve electrical and optical properties. The most common A site dopants are trivalent lanthanum (La). Lanthanum donor dopants in PZT compensate the lead vacancy thereby inhibiting the formation of oxygen vacancies [92]. PLZT thin films are ablated using the fourth harmonics of Nd:YAG laser. The conditions are same as that for the deposition of PZT thin films.

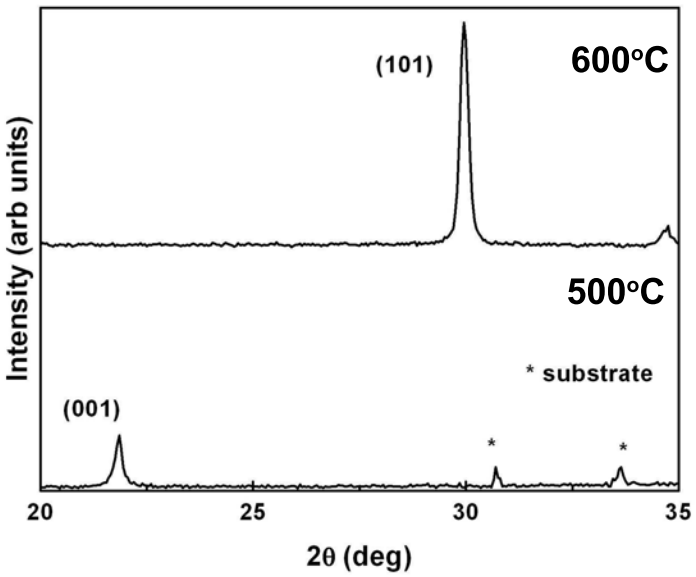

Figure 3.3: The XRD pattern of PLZT thin films on PtSi substrates for various substrate temperatures (* represents substrates and π represents the pyrochlore phase).

From the XRD (figure 3.3) it can be seen that the films grown at T_s = 500^0C have perovskite phase with (001) orientation. But when the substrate temperature was increased to 600^0C, the films showed perovskite phase with (101) orientation. (001) is the oxygen rich phase of perovskite is observed in PLZT thin films. The substrate temperature can be lowered to 500^0C for growing perovskite PLZT thin films. The constituents in the thin film materials can affect the formation of the perovskite structure, the substrate materials will also imposed marked influence on the crystallisation characteristics. The platinum surface of PtSi substrates can possibly

trigger the formation of the perovskite phase at lower temperature [87].

Composition analysis is carried out for PLZT films by EDX is shown in table 3.1. The results shows that the ratio (Pb+La)/(Zr+Ti) is 0.42. Here also there is lead deficiency for films grown at high substrate temperature.

The thickness of all the PZT thin films were around 1 micron.

Table 3.1: The composition and the condition for pervoskite formation

Sample	Pb/(Ti+Zr)	Substrate Temperature for perovskite formation
PZT	0.84	600
P2ZT	0.90	600
P10ZT	0.22	600
PLZT	0.413	500

3.3.1 Effect of buffer layers on the growth of perovskite PZT/PLZT

It is difficult to crystallise PZT thin films in tetragonal perovskite structure directly grown on PtSi substrates. The presence of pyrochlore phase will result in lower polarisation. A thin layer of $PbTiO_3$ deposited prior to the deposition of PZT and PLZT has been shown to assist in the crystallization of the perovskite phase. The $PbTiO_3$ (PT) always crystallites in the perovskite phase which promote the growth of perovskite phase of PZT/PLZT. Very thin layer of $PbTiO_3$ facilitate growth of perovskite phase and have effect on the dielectric properties of the film [93]. The PZT thin films have high dielectric constant for possible pyroelectric detectors. But the dielectric constant of PT is lower. It is possible to decrease the dielectric constant

of PZT by using a thin layer of PT as buffer. The PT buffer layer can assist in perovskite formation; at the same time decreases the dielectric constant which is suitable for pyroelectric application. The formation of perovskite phase of PZT at lower substrate temperature with $PbTiO_3$ thin layer as observed by XRD studies is shown in figure 3.4.

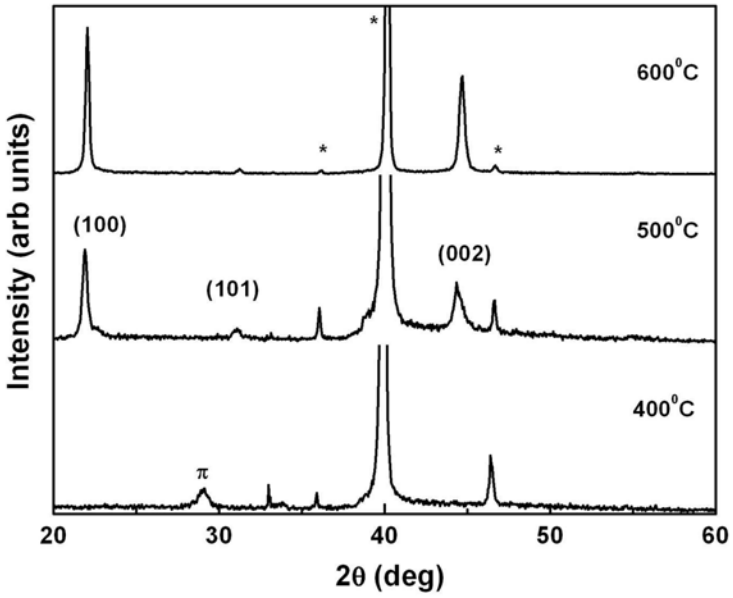

Figure 3.4: The XRD pattern of PZT thin films grown by PLD using the fourth harmonics 266nm with a thin buffer layer of $PbTiO_3$ on PtSi substrates (* represents substrates and π represents the pyrochlore phase)

With the introduction of buffer layer the substrate temperature for the growth of perovskite PZT has been reduced to 500^0C. Pure perovskite phase is obtained with $PbTiO_3$ buffer layer. The thickness of the $PbTiO_3$ layer

is 80nm.

The XRD pattern of PLZT thin films deposited on PtSi substrate with $PbTiO_3$ buffer layer is shown in figure 3.5.

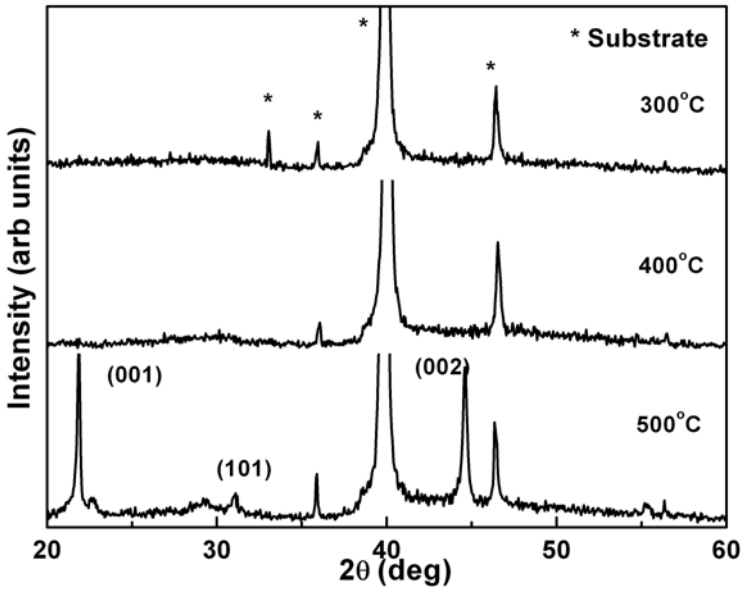

Figure 3.5: The XRD pattern of PLZT thin films on PtSi substrates with $PbTiO_3$ buffer layer

In the case of PtSi/PT/PLZT structure the growth temperature for the perovskite phase is same as that of films grown on PtSi substrates without buffer layer . However the introduction of buffer layer has promoted the growth of (101) oriented PLZT films.

For many device applications substrates that are compatible with both ferroelectric thin films and semiconductor devices are sought where po-

tential direct integration of ferroelectric with semiconductor is envisioned. ZnO is emerging as an important wide bandgap semiconductor material for devices operating in the ultraviolet. ZnO has intrinsic compatibility with ferroelectric oxides as a semiconducting oxide. ZnO has also been used as a buffer layer for PZT ferroelectric capacitors in PtSi and as the channel layer for ferroelectric gate thin film transistors [89].

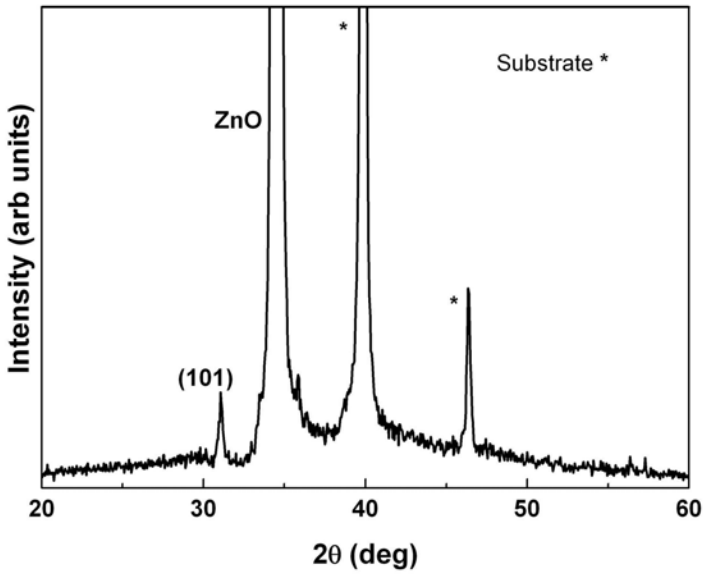

Figure 3.6: The XRD pattern of PZT thin films on PtSi substrates with ZnO buffer layer at $T_s = 300^0$C

Thin film of PZT is found to crystallize in perovskite phase at much lower substrate temperature when ZnO is used as the buffer layer. ZnO buffer layers may not affect the piezoelectric properties of PZT layer since

ZnO itself is a piezoelectric material. ZnO buffer layer has reduced the substrate temperature for the growth of perovskite PZT films from 600^0C to 300^0C. The XRD pattern of ZnO/PZT is shown in figure 3.6. ZnO buffer layer promotes the growth of (101) oriented perovskite phase of PZT thin films.

Compositional analysis confirms that PZT films grown with ZnO buffer layers are stoichiometric. Compositional analysis of thin films with buffer layer is given in the table.

Table 3.2: The composition of PZT thin films and the minimum substrate temperature for pervoskite growth

PT($PbTiO_3$), P2ZT(2% Pb excess PZT target), P10ZT(10% Pb excess PZT target)

Sample	Pb/(Ti+Zr)	Minimum Substrate Temperature for growth of perovskite phase
PT/PZT	0.79	500
PT/P2ZT	0.84	500
PT/P10ZT	0.22	500
PT/PLZT	0.413	500
ZnO/P2ZT	1.02	300

Apart from Pb vacancies, it is widely accepted that oxygen vacancies play an important role in PZT perovskite ferroelectrics. Though the oxygen ambient during deposition is used to prevent the formation of oxygen vacancies in the deposited film, it has been shown that oxide films grown using PLD are still oxygen deficient. The lattice of an O_2 deficient film

expands beyond the size reported for corresponding bulk ceramics. The interfacial defect layers may originate from accumulation of oxygen vacancies. Under the electric field oxygen vacancies migrate towards the electrode and aggregate near the electrode interface. The perovskite structured titanate could not afford a large population of point defects [92, 94].

In the case of conducting oxide electrodes or aqueous solution electrodes, oxygen vacancies in the perovskite film in the region near the film electrode interface can be compensated by the electrodes. Thus the use of this kind of electrodes inhibits the accumulation of oxygen vacancies at the interface. As a result no interfacial defect layer forms at ferroelectric oxide interfaces.

Oxide thin films have a wide range of properties covering insulators to high temperature superconductors and from ferroelectric to ferromagnetic materials. The growth of oxide thin films is an active field of research [95, 96]. Perovskite conducting oxide $La_{0.5}Sr_{0.5}CoO_3$(LSCO) is obtained from ABO_3 perovskite $LaCoO_3$ by partial substitution of La^{3+} by Sr^{2+} [97, 98]. The similar crystal structure of LSCO with that of the perovskite ferroelectrics makes it a potential candidate as electrode for ferroelectric memory devices. The LSCO which is a conductive oxide electrode act as oxygen vacancy sink of the PZT capacitors thereby reducing the fatigue problem usually encountered while using conventional Pt electrode [99–102]. The similar crystal structure of LSCO and perovskite ferroelectrics facilitates the easy growth of ferroelectrics over textured or epitaxially grown LSCO layer [103, 104]. $La_{0.5}Sr_{0.5}Co_{1-x}Ni_xO_3$ (LSCNO)is also widely used as electrode for ferroelectric memory devices [105]. The partial substitution of Co by Ni in $La_{0.5}Sr_{0.5}CoO_3$ has been reported to increases the electrical conductivity of LSCO thin films [106].

Hence for fabrication of capacitors using PZT thin films, $La_{0.5}Sr_{0.5}CoO_3$ (LSCO) and $La_{0.5}Sr_{0.5}Co_{1-x}Ni_xO_3$ (LSCNO)were used as electrodes. These will serve as an electrode as well as a template for the growth of ferroelectric PZT thin films.These oxide electrode layers were deposited on PtSi substrates by rf magnetron sputtering. The sputtering power was kept at 100W with an argon gas pressure of 0.003mbar and the substrate temperature at 600^0C. The films were crystalline and has a thickness of about 400nm.The resistivity of all the samples were of the order $10^{-5}\Omega$cm.The typical x ray diffraction pattern of LSCO and LSCNO on PtSi substrates is shown in figure 3.7 [107].

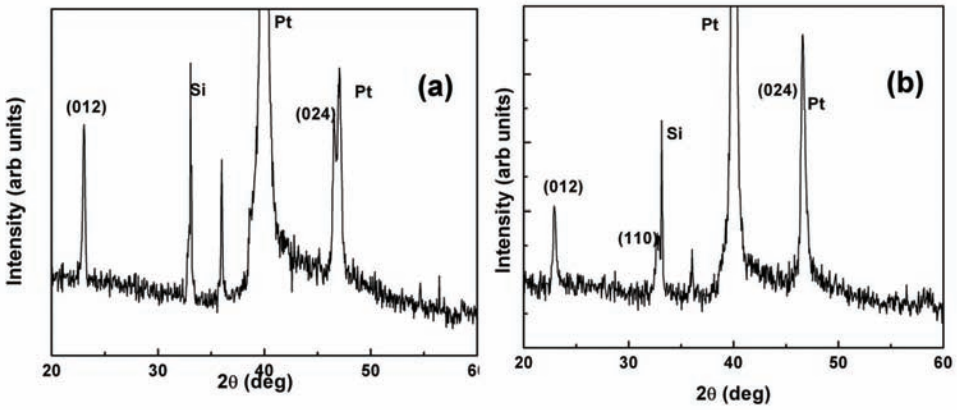

Figure 3.7: The XRD pattern (a) LSCO (b) LSCNO thin film electrodes deposited by rf magnetron sputtering

Thin films of PZT was deposited on LSCO and LSCNO oxide layers. The crystallinity of PZT thin films grown on LSCO and LSCNO electrodes

was studied using XRD. The figure 3.8 shows the perovskite structure of PZT films grown on LSCO and LSCNO electrode.

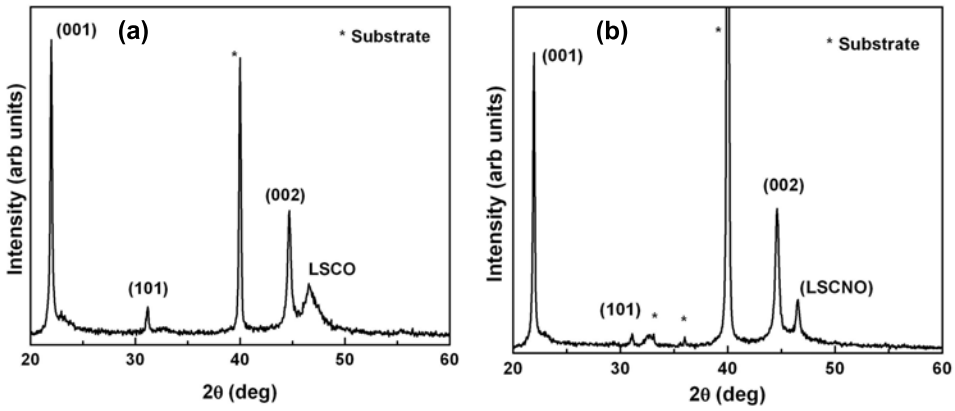

Figure 3.8: The XRD pattern of thin film PZT deposited on (a) LSCO and (b) LSCNO electrode

The films deposited at a substrate temperature of 500^0C showed crystallinity with pure perovskite phase. This growth temperature is lower than the substrate temperature needed for perovskite formation of PZT thin films on PtSi substrates.

The perovskite PZT thin film has a lattice constant of 3.85A^o. The LSCO and LSCNO materials also has perovskite structure with lattice parameter a = 3.805A^o. The lattice match between PZT and PLZT with LSCO and LSCNO be one of the reasons for the perovskite formation of PZT and PLZT at low temperature on LSCO/LSCNO films.

The surface morphology of the PZT thin films on PtSi substrates with and without buffer layer are studied.Figure 3.9 shows the SEM images of

PtSi/PZT, PtSi/PT/PZT, PtSi/ZnO/PZT and PtSi/LSCNO/PZT. The PZT films on PtSi substrates show particulates. This may be due to the high temperature and low oxygen pressure inside the chamber. The low sticking coefficients of Pb may have formed particulates at this pressure and temperature.

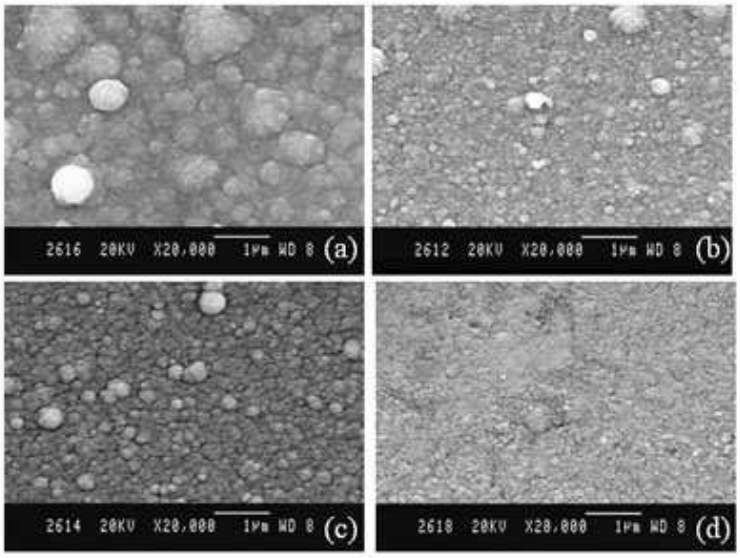

Figure 3.9: The SEM images of (a)PtSi/PZT (b) PtSi/PT/PZT (c) PtSi/Zno/ PZT and (d) PtSi/LSCNO/PZT

The films grown on ZnO buffer layer and oxide electrode LSCNO is crack free.

The cross sectional SEM of PZT thin films on LSCO electrodes on PtSi substrates is shown in figure 3.10. The electrode PZT interface is free from

defects and cracking.

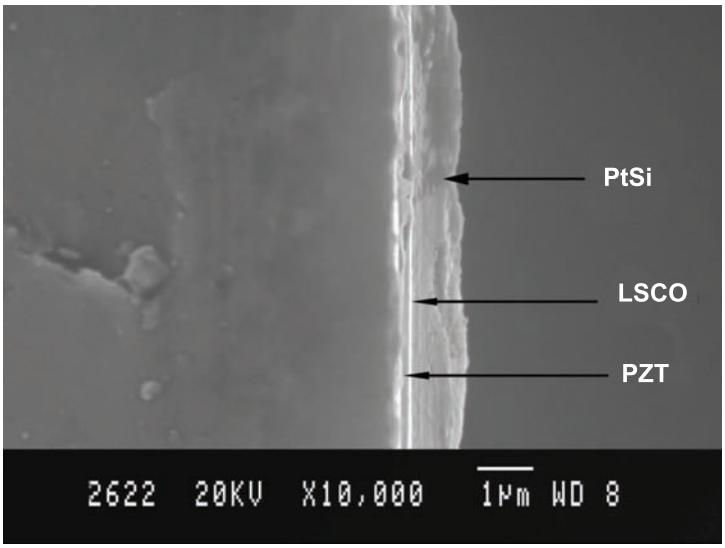

Figure 3.10: The cross sectional SEM of PZT/LSCO interface

3.4 Electrical characterization

The electrical characterizations using impedance analyser were carried out by forming a capacitor with PZT between the bottom Pt (or oxide LSCNO) and the top gold electrode. The top gold electrode is deposited by rf sputtering. Figure 3.11 shows the structure used for electrical measurements of PZT thin films.

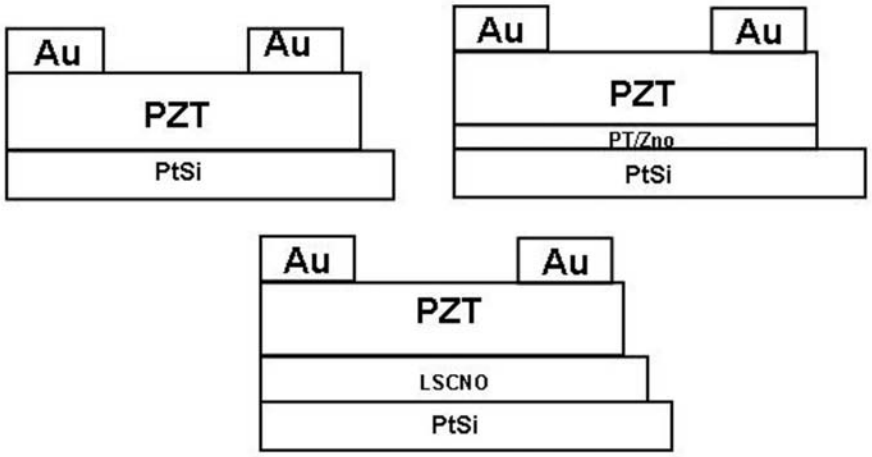

Figure 3.11: The different bottom electrode configuration used for electrical measurements (a)PtSi bottom electrode (b) $PbTiO_3$ or ZnO buffer layer(c) LSCNO bottom electrode

All the electrical characterizations were carried out on thin films of PZT in their perovskite structure.

3.4.1 Leakage current studies

The leakage current of the samples were found from the current - voltage (I-V) curve, where the current is measured at a specified voltage. The leakage current is an important characteristic of thin film ferroelectric capacitors, it directly limits the charge retention and it influences the ferroelectric hys-

teresis loop. The leakage current is also a sensitive electrical probe to the material quality of heterostructure as it is strongly dependent on material aspects of the ferroelectric film and of electrode-ferroelectric interfaces [107]. Capacitor with low leakage current is ideal for microelectronic device application.

PtSi/PZT/Au and PtSi/PT/PZT/Au

The leakage current of all the samples were measured using constant current and voltage source. The figure 3.12 shows the leakage current density vs electric field of PtSi/PZT/Au and PtSi/PT/PZT/Au structures. From the figure it can be seen that the leakage current with $PbTiO_3$ buffer layer is greater than that of heterostructure with PZT thin film alone. The buffer layer has not reduced the leakage current of PZT thin films in contrary the leakage current has increased due to the buffer layer. The extrinsic additives affect the nature and distribution of defects present in the PZT thin films [108]. Defect distribution and their subsequent mobility have a direct impact on leakage current. Oxygen defect of PZT thin films may increase when PT thin films were used as buffer layer.At the same time PZT thin films have the same structure as that of PT films. Hence leakage current is of the same order [93].

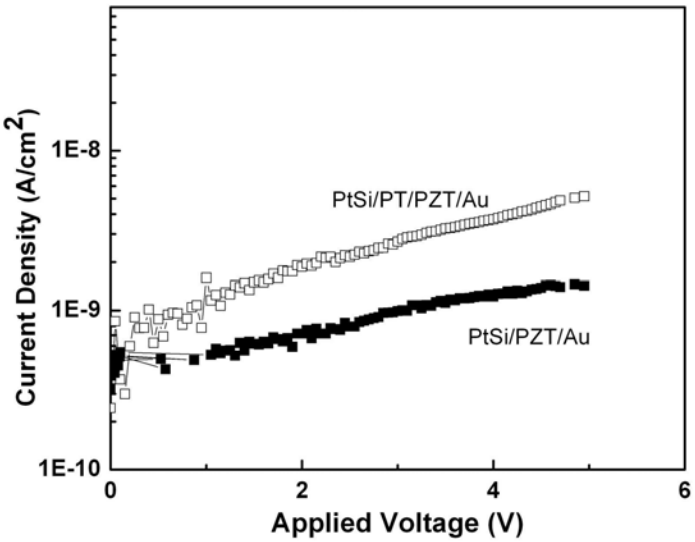

Figure 3.12: The current voltage characteristics of PZT heterostructure with and without PT buffer layer

All the films show good insulating properties. Initially, the leakage current shows an ohmic behavior for low fields. At slightly higher electric fields, there is an onset of non-linearity, the cause of which can be said to be the onset of the space charge limited conduction (SCLC) mechanism. The space charge limited current follows the law

$$I = \frac{V^{(l+1)}}{d^{(2l+1)}} \tag{3.1}$$

$$l = \frac{T_t}{T} \tag{3.2}$$

where, d = thickness of the thin films and T_t is the temperature parameter characterizing the trap distribution and T is the absolute temperature, for a distributed-trap space-charge limited conduction[97]. The measurement is carried out at room temperature. The conduction process for the structure is obtained by the analysis of the slope at different regions of the I-V plot by taking the log log plot of current density vs applied field.

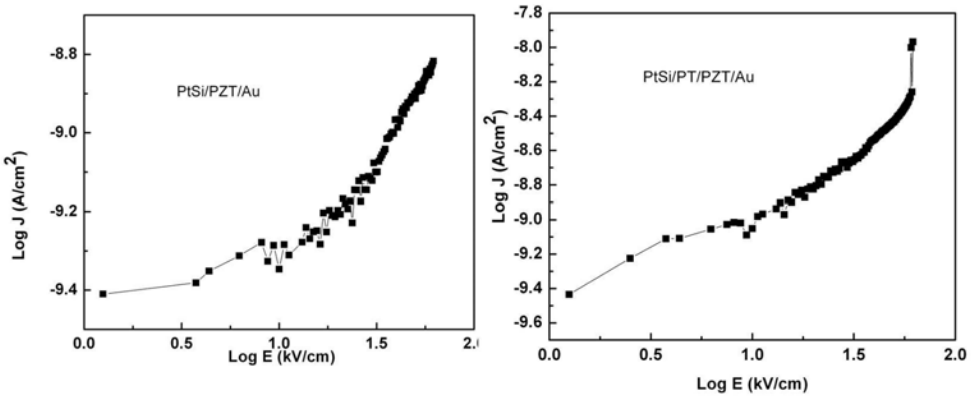

Figure 3.13: Log J versus Log E plot of the device (a)PtSi/PZT/Au and (b)PtSi/PT/PZT/Au

The variation of log J with log E in both the structures are similar as shown in figure 3.13. It consists of a low field linear region and a high field nonlinear region.

In the low field region (i) in the figure 3.13 the film shows ohmic nature. At room temperature, it can be assumed that enough charge carriers are present within the film, so as to contribute to the conduction process and hence a linear field dependence of conductivity can be observed. The onset

of the non-linear character for both types of contacts lie within region(ii) in the figure 3.13 , where a prominent role of the electrode is revealed. The onset of non-linearity is a combined effect of the Schottky emission through the contact interface and the SCLC mechanism within the bulk. The leakage current in the films is dominated by space charge limited current (SCLC) mechanism which can be expressed in the following form [109].

$$J = \frac{9\mu\epsilon_0\epsilon_r E^2}{8d} \tag{3.3}$$

where J is the leakage current density, μ is the charge carrier mobility, ϵ_0 is the permitivity of free space,ϵ_r is the dielectric constant of the film and d is the film thickness.

PtSi/ZnO/PZT/Au

The figure 3.14 shows the leakage current density vs electric field of PtSi/ZnO/PZT/Au structures. The films show good insulating behavior.The current voltage characteristics were carried out at room temperature.It can be seen that current density has increased with ZnO buffer layer.

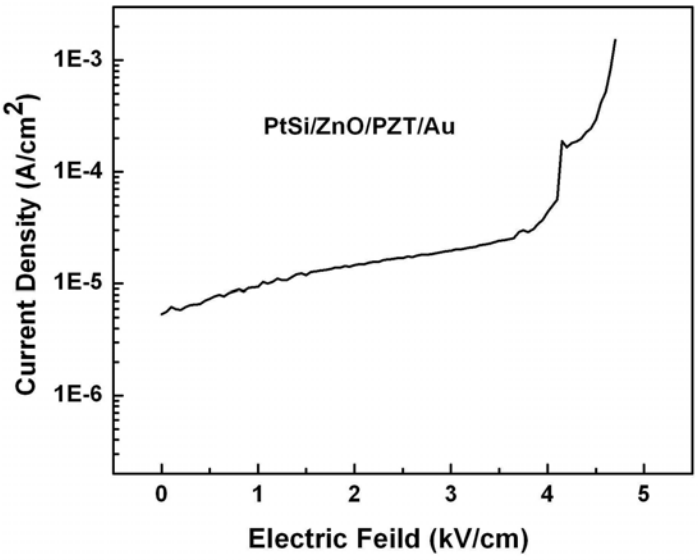

Figure 3.14: The current voltage characteristics of the device PtSi/ZnO/PZT/Au structure

The oxygen vacancies play an important role in the resistance degradation. They are positively charged with respect to the regular lattice and thus in a dc electrical fields they migrate towards the cathode. The increase in current density can be attributed to a decrease in the effective barrier height at the cathode [110].

The applied voltage can be divided into two regions a low voltage region and a high voltage region. The data is replotted according to equation for Pool Frenkel emission as Log J/E vs $E^{1/2}$ as shown in figure 3.15. The log (J/E) curves show only a small increase with $E^{1/2}$. In the high voltage region these value increases linearly with $E^{1/2}$.

The log log plot of the structure is shown in figure 3.16. In the low voltage region the graphs is linear with slope 0.75. Hence under low field the contact to ZnO/PZT structure is ohmic in nature. Under high field the distribution of the electrons is disturbed and the leakage current deviates from ohmic nature. The conduction mechanism is dominated by Pool-Frenkel emission.

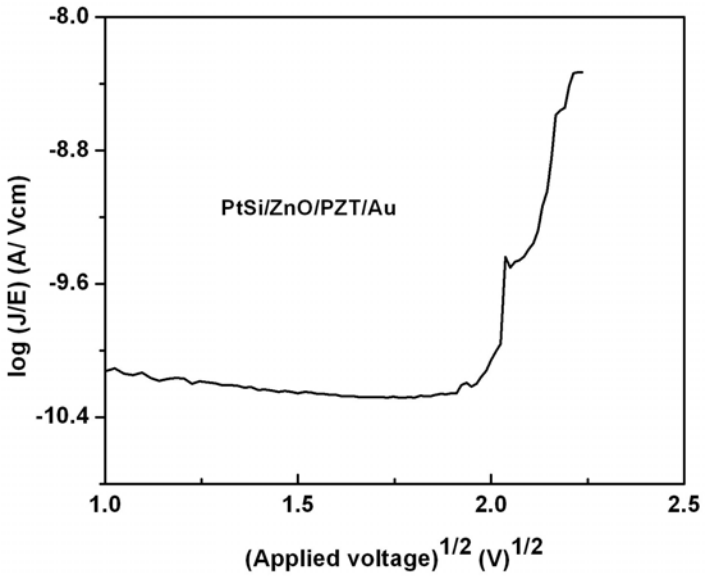

Figure 3.15: Log J/E versus $\sqrt{E}$ plot of the device PtSi/ZnO/PZT/Au structure

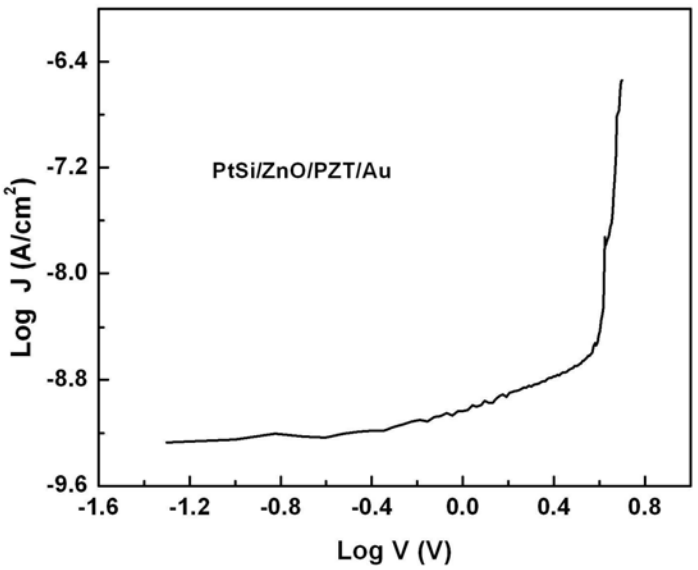

Figure 3.16: Log J versus Log V plot of the device PtSi/ZnO/PZT/Au structure

PtSi/LSCO(LSCNO)/PZT/Au

The electrical characterization of PZT thin films on oxide electrodes is investigated. The PZT films are insulating and bottom oxide layer is conducting. The leakage current density as a function of applied field for the structure PtSi/LSCNO/PZT/Au is shown in figure 3.18. Here also the oxide layer has decreased the effective barrier height thereby increasing the current density.

The IV characteristics of the heterostructure was studied using Keithley source measure unit. The figure 3.17 shows the current density-time graph of the device PtSi/LSCNO/PZT/Au. From the figure it can be seen that

at room temperature there is no current relaxation. The current after 100s can be taken as the true value of leakage current.

The data is reploted as log log plot to analyse the conduction mechanism. The figure 3.19 shows the Log J log V plot of the structure. The graph shows two regions a low voltage and high voltage region.

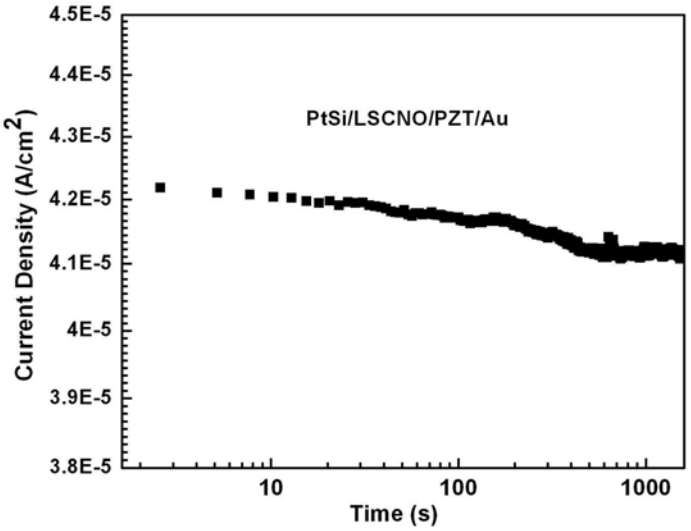

Figure 3.17: The room temperature current density-time plot of PtSi/LSCNO/ PZT/Au at an applied voltage of 1V

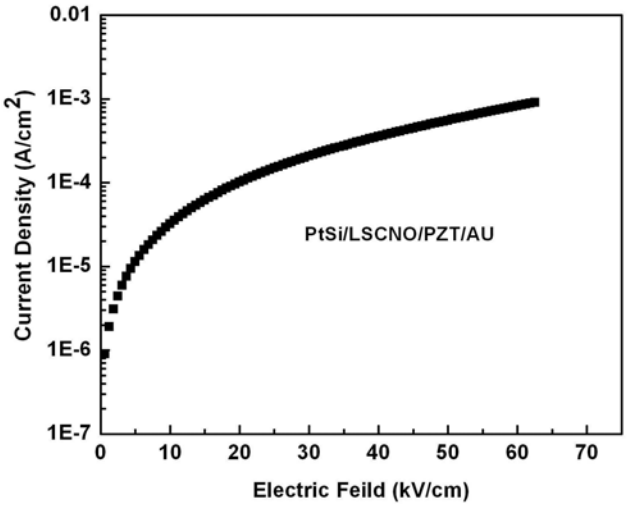

Figure 3.18: The room temperature leakage current of the structure PtSi/LSCNO/ PZT/Au

In the low voltage the slope of the graph is 1.28 which shows the behavior is ohmic. In the high voltage region also the behavior doesnt show much deviation. The slope in the region is 1.9.

The device show no effect of traps. The slope of the above plot is less than 2 both at higher and lower fields. which suggests a trap free space charge limited current (SCLC).

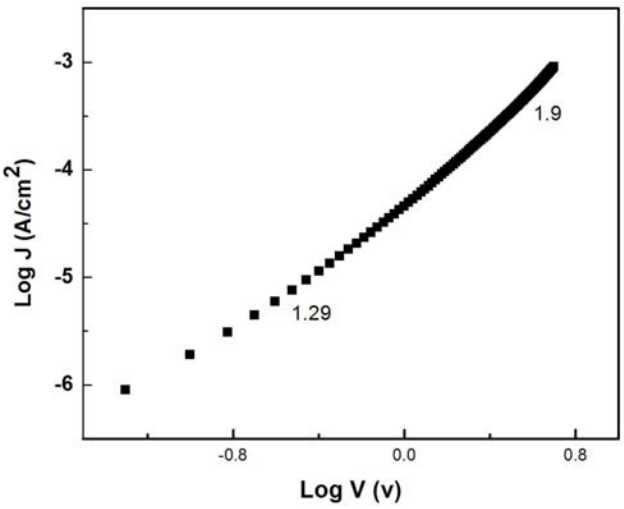

Figure 3.19: LogJ LogV plot of the device structure PtSi/LSCNO/ PZT/Au

3.4.2 Capacitance frequency measurements

The dielectric constant is given by the relation 3.4

$$\epsilon = \frac{Cd}{A\epsilon_0} \tag{3.4}$$

Where C is the capacitance in farads, ϵ_0 the free space dielectric constant ($8.85\text{x}10^{-12}\text{Fm}^{-1}$), A is the area of the capacitor and d is the thickness of the ferroelectric thin film.

PtSi/PZT/Au and PtSi/PT/PZT/Au

Figure 3.20 shows the variation of dielectric constant with frequency for the perovskite PZT films grown on PtSi substrates with and without $PbTiO_3$

(PT) buffer layer . The introduction of PT buffer layer has reduced the deposition temperature of PZT thin films in the present study. But the dielectric constant has diminished for the device fabricated with $PbTiO_3$ buffer layer(figure 3.20).

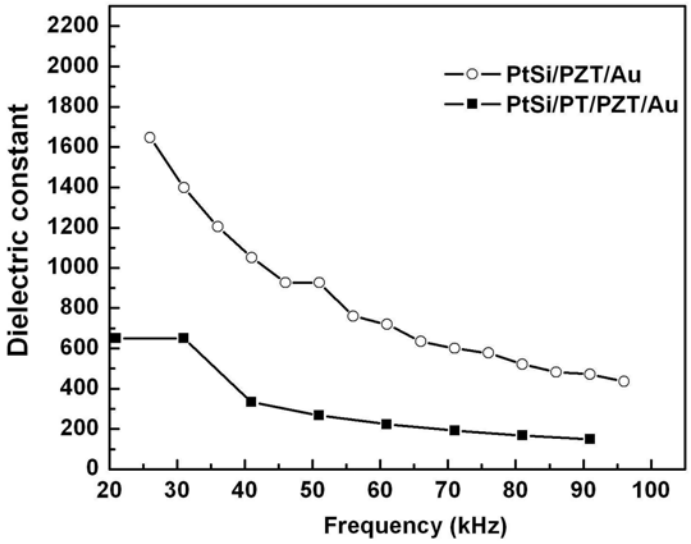

Figure 3.20: The variation of dielectric constant with frequency for PZT thin films for the structure PtSi/PZT/Au and PtSi/$PbTiO_3$/ PZT/Au structure

The reduction in the dielectric constant of PZT thin films with buffer PT layer can be attributed to the lower dielectric constant of $PbTiO_3$ layer. The thin layer of $PbTiO_3$ and PZT film behaves like series capacitance. Hence the total capacitance will be reduced due to the smaller capacitance of $PbTiO_3$. Thus the introduction of PT can decrease the dielectric constant of PZT thin films. The reduced dielectric constant of PZT with $PbTiO_3$

finds application in pyroelectric detectors.

PtSi/ZnO/PZT/Au

The effect of ZnO buffer layer on the electrical properties of PZT thin films has been also investigated. The variation of dielectric constant with frequency is shown in figure 3.21.

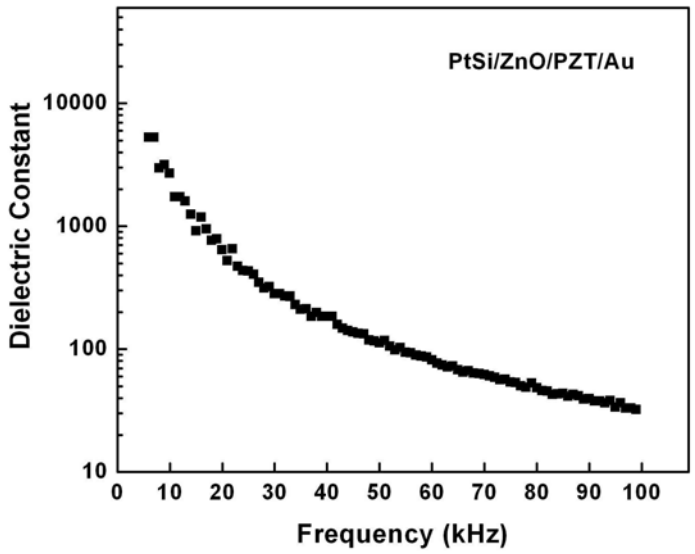

Figure 3.21: The variation of dielectric constant with frequency of PtSi/ZnO/ PZT/Au with PZT dielectric on ZnO buffer layer.

The dielectric constant of PZT with ZnO buffer layer shows similar value as that of PZT thin films without buffer layer. However it was possible to reduce the substrate temperature substantially to 300^0C with ZnO buffer

layer.

ZnO buffer layer, a metal oxide, is known to contain oxygen vacancies as a predominant point defects. It can alleviate the oxygen vacancy accumulation at the PZT/ZnO interface via oxygen transport at the interface. This should enhance the ferroelectric properties of PZT thin films. But in the present work the orientation of PZT is along (101). The polarization of the ferroelectric materials with the tetragonal structure is along (001) direction [111].

PtSi/LSCNO/PZT/Au

The variation of capacitance with frequency for the device structure PtSi/ LSCNO/PZT/Au is as shown in the figure 3.22. The films show dielectric constant of 900 at 1kHz.The variation of dielectric constant shows a frequency dispersion. The dielectric constant has not increased considerably compared with PtSi/PZT/Au structure.

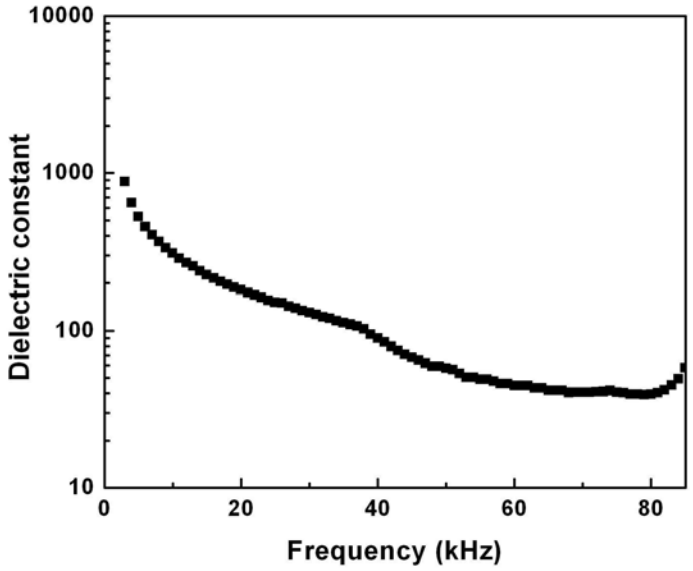

Figure 3.22: The variation of dielectric constant with frequency of thin film PZT deposited on LSCNO electrode for the structure PtSi/LSCNO/PZT/LSCNO/Au

3.4.3 Capacitance Voltage measurements

Dielectric permittivity versus electric field (or capacitance C versus voltage V) loops are often used in the characterization of ferroelectric materials. Measurements of ϵ - E (or C-V) curves are usually made by applying simultaneously on the sample a DC field which changes as a step-like function and an AC voltage of relatively high frequency (1 kHz or above) of small amplitude. The AC voltage is used to measure the capacitance which is then plotted as a function of the DC bias field, giving a C-V graph.

Initial rise in the permittivity with DC field is probably due to increased

movement of the domain walls which become 'free' from defects and will lock them at zero-DC field [112]. This is due to partial switching of some domains whose coercive field happens to be small enough and which can be switched by the DC and AC field combination. The maximum in the ϵ - E curve appears in the vicinity of the coercive field for the P-E hysteresis when most of the domains switch and the material appears to be dielectrically very 'soft'. At high DC fields, the permittivity decrease reflects two processes: (i) decrease in the number of domains as they become aligned with the field (ideally the sample becomes a single domain and only lattice contributions are present) and (ii) inhibition of the movement of residual domain walls by the DC field [112].

In all the devices studied and presented in this chapter the top and bottom electrode are of different material. The carrier concentration and electronic work function of the top and bottom electrode are different.This causes a shift in the C-V plot or hysteresis loop.

PtSi/PZT/Au

The variation of dielectric constant with voltage (ϵ - E) of PZT thin films with PtSi as bottom and Au as top electrode is shown in figure below 3.23.

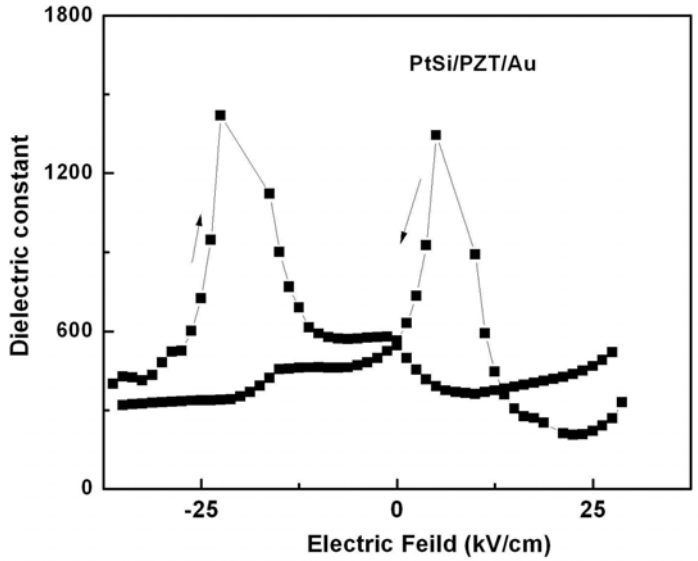

Figure 3.23: The butterfly loop (C-V characteristic) of thin film PZT ferroelectric capacitor with PtSi bottom electrode and Au as top electrode

The variation of dielectric constant with voltage of PZT thin films showed a butterfly loop. The butterfly shaped CV curves imply that the PZT films possess ferroelectric characteristics. The PZT films for this device structure was deposited at 600^0C to ensure the growth of perovskite ferroelectric phase. The maxima of the CV plot correspond to the coercivity (E_c). The coercive field for both the positive and negative field at 100kHz was found to be 28kV/cm and -25kV/cm respectively for a 800nm thick PZT film.

PtSi/PT/PZT/Au

The variation of dielectric constant with voltage (ϵ - E) of PtSi/PT/PZT/Au structure is shown in figure 3.24.

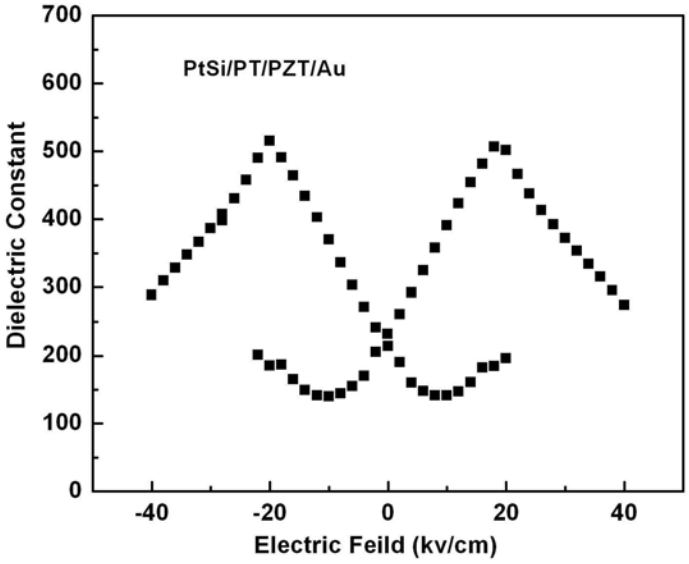

Figure 3.24: The butterfly loop (C-V characteristics) of thin film PtSi/PT/PZT/Au structure

The variation of dielectric constant with voltage of this films showed a butterfly loop. The butterfly shaped CV curves imply that the PT/PZT films possess ferroelectric characteristics. Here the PT buffer layer has reduced the growth temperature for the perovskite phase. The positive and the negative coercive field at 100kHz was found to be 18kV/cm and -22kV/cm respectively for a 800nm thick PZT film. The switchable field

of the device has also come down to 22kV/cm when PT buffer layer was introduced.

PtSi/ZnO/PZT/Au

The variation of dielectric constant with voltage (ϵ - E) of PZT thin films with PtSi/ZnO/PZT/Au structure is shown in figure 3.25.

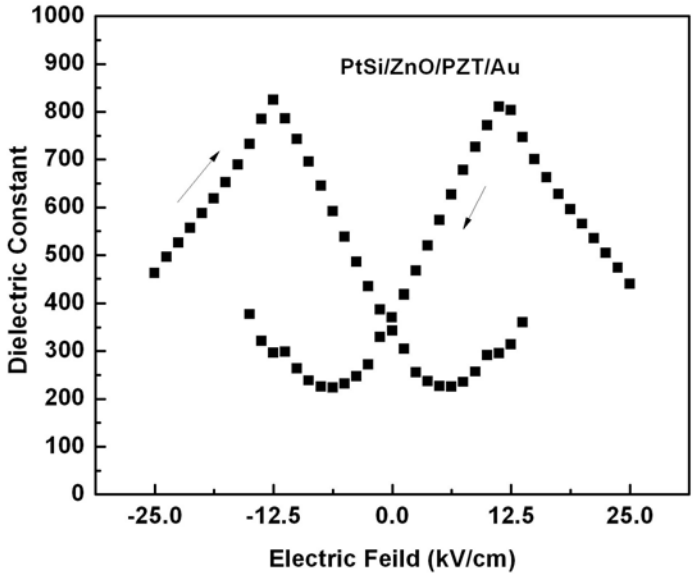

Figure 3.25: The butterfly loop (C-V characteristics) of thin film PZT deposited on PtSi electrode with ZnO buffer layer(PtSi/Zno/PZT/Au structure

The variation of dielectric constant with voltage of ZnO/PZT multilayer thin films showed a butterfly loop. The butterfly shaped CV curves imply that the films possess ferroelectric characteristics for the device structure

PtSi/ZnO/PZT/Au. The ZnO layer has substantially reduced the growth temperature of PZT thin films to 300^0C. But the ferroelectric properties were not deteriorated with the ZnO buffer layer. The maxima of the CV plot correspond to the coercivity (Ec). The coercive field at 100kHz was found to be 12kV/cm -15.6kV/cm for a 800nm thick PZT film. The switchable field of PtSi/ZnO/PZT/Au is smaller than that of PtSi/PT/PZT/Au structure.

PtSi/LSCNO/PZT/Au

The variation of capacitance of PtSi/LSCNO/PZT/Au structure as a function of applied voltage is shown in figure 3.26. The C-V exhibit a butterfly loop showing the ferroelectric nature of the LSCNO/PZT multilayers.

The coercive field of the devices can be obtained from the butterfly curve. Here the bottom electrode is LSCNO. The switching field at 10kHz is as low as 10kV/cm with oxide electrode for a 800nm thick PZT film. The coercive field for PtSi/LSCNO/PZT/Au heterostructure is lower than all the other structures investigated in the present study. This can be attributed to the better growth and crystallinity of PZT on LSCNO electrode.

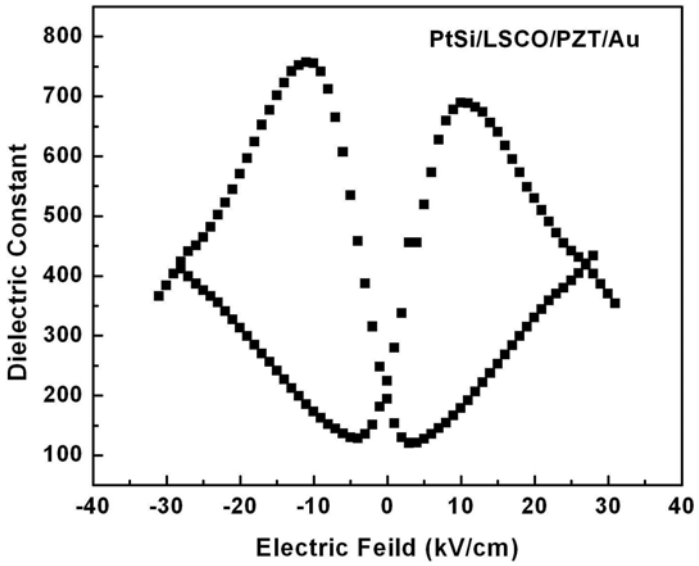

Figure 3.26: The butterfly loop (C-V characteristics) for PtSi/LSCNO/PZT/Au device

The LSCNO being an oxide electrode compensate the oxygen vacancy accumulation at the PZT/LSCNO interface. This may improve the ferroelectric property since oxygen vacancy play a detrimental role in domain wall pinning which was widely accepted as the main mechanism of ferroelectric fatigue.

The ferroelectric properties of PtSi/LSCO/PZT/Au have been studied using RT ferroelectric tester. The hysteresis behavior of the device is shown in figure 3.27. The remnant polarization of $4\mu C/cm^2$ and coercive field of 58kV/cm is obtained for films deposited on LSCO. The saturation polarisation is about $6\mu C/cm^2$.

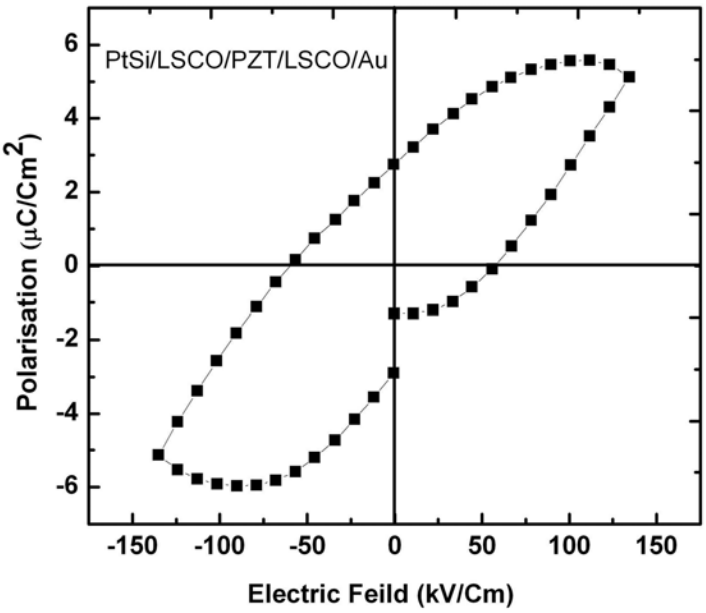

Figure 3.27: P-E hysteresis loop of the PtSi/LSCO/PZT/Au structure

3.5 Conclusion

PZT and PLZT thin films were deposited by pulsed laser deposition on PtSi substrates. Pure perovskite phase PZT thin films was obtained at a substrate temperature 600^0C for PZT thin films. The Pb excess targets were used for compensating the Pb loss in the PZT thin films. $PbTiO_3$ and ZnO buffer layers were deposited to lower the deposition temperature. Pervoskite phase was formed in all thin films at much lower temperature.The PT buffer layer have decreased the dielectric constant of PZT thin films for

possible application in pyroelectric detectors. ZnO buffer layer has lowered the deposition temperature to 300^0C. Stoichiometry is confirmed by composition analysis of the samples. Electrical characterization of the samples with and without buffer layer were studied. The leakage current through the sample were studied. The variation of dielectric constant with frequency shows a dispersion nature.The capacitance voltage measurements show butterfly loop for all the ferroelectric samples. The coercive field of the structure is the maxima of the C-V plot.This switchable field is lower for films deposited with LSCNO oxide electrode.

Chapter 4

Influence of oxygen to argon ratio on the optical and structural properties of rf magnetron sputtered $Ba_{0.7}Sr_{0.3}TiO_3$ thin films.

The optical properties of barium strontium titanate thin films are important due to its wide band gap, high refractive index and low absorption coefficient and hence find application in electro-optic devices and non-linear optical systems. $Ba_{0.7}Sr_{0.3}TiO_3$ (BST) thin films were deposited by rf magnetron sputtering on fused silica and $Pt/TiO_2/SiO_2$ (PtSi) substrates at relatively low temperature. The crystallisation of thin films strongly depends on O_2/Ar ratio. The optical parameters like band gap (E_g), re-

fractive index (n) were studied as a function of O_2 mixing ratio (OMR) in the sputtering gas. The electrical properties of BST thin films deposited on PtSi substrates as a function of OMR is also studied. The films show tunability 50% with minimum loss of 0.018 at 1MHZ for films grown at the optimized O_2 to Ar ratio.

4.1 Introduction

In the recent years ferroelectrics have gained much attention in the fabrication of novel functional devices. Barium strontium titanate (BST) has extensively studied because of its high dielectric constant, low dielectric loss, low fatigue and low leakage current [29]. This complex perovskite oxide is a potential material for the use in high density dynamic random access memories (DRAM) [113], voltage tunable devices and sensors [114].

Previous research into BST thin films has mainly been focused on wireless telecommunications because these materials exhibit high tunability and low dielectric loss in the microwave region at room temperature[115–118]. Recently much attention has also been paid to BST thin films in integrated opto-electronic device application since they have large electro optic coefficient and relatively low optical loss [119] .

The wide bandgap, high refractive index and low absorption coefficient of BST thin films find application in electro-optic devices and non linear optical systems [119, 120]. The parameters which govern the overall optical performance of these films for electro-optic applications are the band gap (E_g), refractive index (n) and extinction coefficient (k). Among these the optical band gap is an important parameter for electro optic materials. In

most cases an increase in bandgap of BST thin films depending on Ba/Sr ratio compared to bulk value with same composition has been reported.

Various deposition techniques are being used for the growth of BST films such as sputtering [121] , sol-gel process [37] and pulsed laser deposition [122–124]. The sputtering has some advantages such as high deposition rate, better homogeneity control and ease of fabrication of large area thin films [125]. Sputtering has been employed extensively to deposit BST thin films as it promotes uniformity, good adhesion to the substrates, a smoother surface and lower deposition temperature [126]. It is well known that both electronic and optical properties of the films which are sensitive to their stoichiometry [127], microstructure [128] and crystallinity [129] are determined by the sputtering and post deposition process.There are few reports on the dependence of optical properties on the deposition conditions like substrate temperature and O_2/Ar ratio during sputtering of thin film [126, 130, 131]. In all these cases the deposition temperature is very high and the films required post deposition treatments at high temperatures.

Due to the enormous technological importance in electronic and photonic applications, it is necessary to study the interdependence of the optical and structural properties of BST film as a function of sputtering condition [132]. Single crystals such as MgO, Sapphire, $SrTiO_3$ are the substrates usually used for the deposition of ferroelectric thin films for the application of optical devices,as the epitaxial films grown on such substrates have better optical properties than polycrystalline films grown on quartz. The use of quartz as substrates has economical advantages as they are cheaper than single crystals. Therefore it is necessary to fabricate well oriented thin films on quartz substrates. However, the growth of perfect and pure ferroelectrics has proven to be very difficult. Another fact is that indium

tin oxide(ITO) based optoelectronic devices can be fabricated on quartz substrates at temperatures higher than the crystallization temperature of BST. Thus monolithic integration of the BST devices with prefabricated ITO based devices on quartz substrates is feasible.

This chapter describes the growth of BST thin films by rf sputtering and its structural, optical and electrical characterizations. The chapter is divided into two sections. Section 4.3 describes the structural and optical properties of BST films grown by rf magnetron sputtering. A correlation has been observed between the structural and optical property of the BST thin films with O_2/Ar ratio during sputtering. Better optical properties of the BST films were obtained at lower substrate temperature without any post deposition heat treatment. The important role of grain size in modulating optical properties is explained here. Section 4.4 gives an account on the electrical properties of BST films depsoited on PtSi substrates.

4.2 Experimental

$Ba_{0.7}Sr_{0.3}TiO_3$ (BST) thin films were deposited by rf magnetron sputtering on fused silica and $Pt/TiO_2/SiO_2$ (PtSi) substrates. The presynthesised $Ba_{0.7}Sr_{0.3}TiO_3$ powder by solid state reaction was used as the target. The target to substrate distance was kept at 5cm. The sputtering was carried out at rf (13.56MHz) power of 100 watts at a pressure of 0.01mbar. The structural characterisation and grain size of BST thin films were analysed by X ray diffractometer (Rigaku) with Cu K_α radiation in θ - 2θ configuration.The grain size of BST thin films was determined by Scherrer's formula from equation (4.1).

$$d = \frac{0.9\lambda}{\beta cos\theta} \tag{4.1}$$

where d is the grain size, λ is the wavelength of x-ray used(1.5418$\mathring{A}$), β is the FWHM in radians of the peak at the diffraction angle θ.

The composition analysis is carried out using energy dispersive x- ray analysis (EDX) as well as x ray photon spectroscopy (XPS) with Al K_α source. Thickness of the film was measured using the surface profiler (Dektak 6M). The optical transmission of the films on fused silica has been studied using UV-Vis-NIR spectrophotometer (Jasco V 570) in the wavelength region 190-2600nm.

4.3 Structural and optical properties of rf sputtered BST thin films

4.3.1 Structural Characterisation

Figure 4.1 shows the x -ray diffraction (XRD) pattern of BST thin films sputtered at 0.01millibar at different substrate temperatures on PtSi substrates. The films grow with the (110) plane parallel to the substrate. When sputtered at room temperature the films were amorphous. Crystalline films with a preferred (110) orientation were obtained when the substrate temperature was 300^0C which is lower than reported value [133, 134]. The optimisation of the process parameters like pressure, oxygen content in the present study leads to the growth of crystalline films at lower substrate temperature.

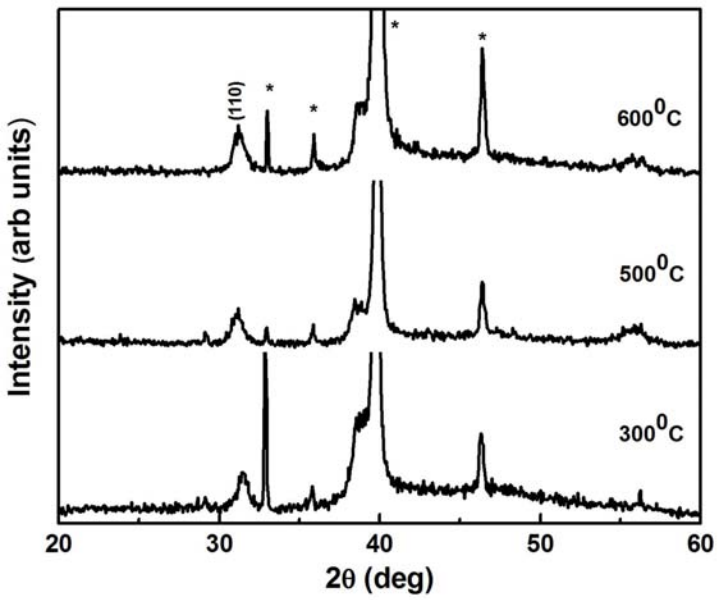

Figure 4.1: XRD pattern of BST thin films deposited on PtSi substrates at different substrate temperatures

.

The BST thin films on quartz substrates show crystalline nature when substrate temperature is 500^0C. The reason is the influence of different lattice parameters for fused quartz and PtSi substrates. Another reason is the fact that the real substrate temperature during sputtering of fused quartz is lower when compared with PtSi substrates. The fused quartz is transparent for IR waves radiated by the heater and there is large difference in thermal conductivity between PtSi and quartz [134].

Figure 4.2 shows the x -ray diffraction (XRD) pattern of BST thin films sputtered at 0.01millibar at a substrate temperature 500^0 C on PtSi and fused silica substrates for different O_2 to Ar ratio. The crystallisation of

thin films strongly depends on O_2/Ar ratio.

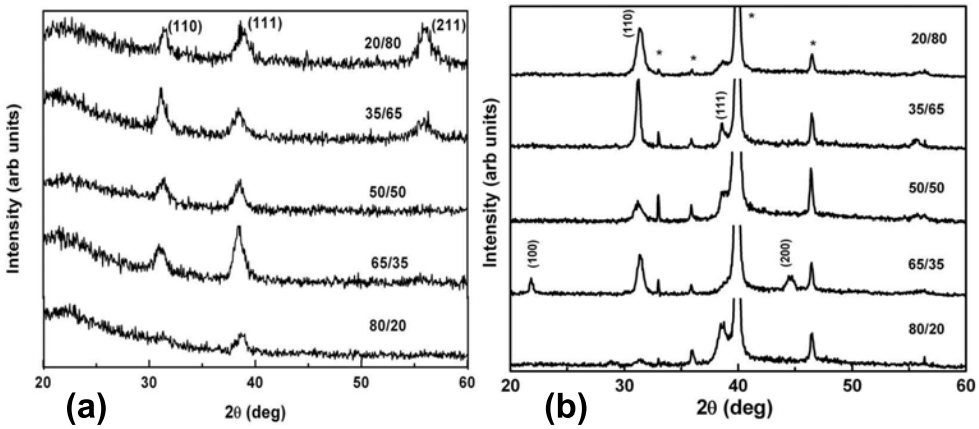

Figure 4.2: The XRD pattern BST thin films grown at 0.01 mbar at 500^0C at rf power 100 W for various O_2 to Ar ratio on (a) quartz substrate (b)on PtSi substrate.

The oxygen to argon ratio is also found to influence the growth of crystalline perovskite thin films. From the figure it can be seen that the (110) peak of perovskite is prominent. FWHM is minimum or crystallinity is better for thin films grown at 35/65 oxygen to argon ratio. The variation of FWHM of (110) peak of BST thin films on quartz substrates with O_2 to Ar ratio is shown in figure 4.3. There is an optimum ratio for obtaining (110) oriented crystalline BST thin film. This behavior is predictable as film stoichiometry, structure, texture are affected by the oxygen to argon ratio.

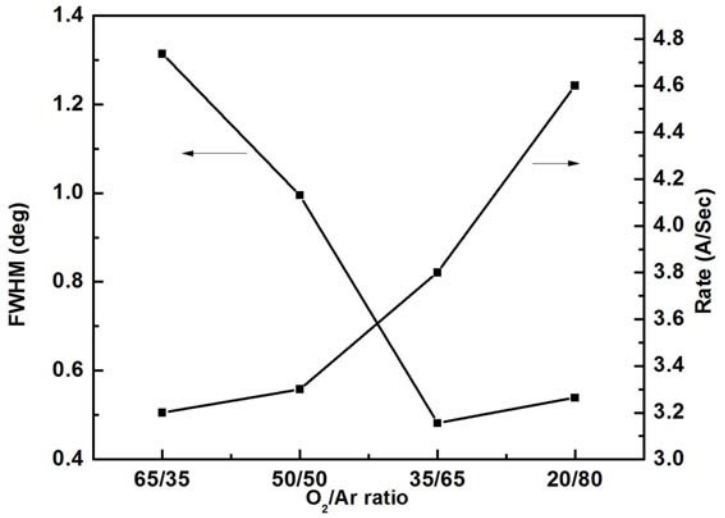

Figure 4.3: The variation of FWHM of (110) peak and rate of deposition of BST thin film grown on quartz substrates with O_2 to Ar ratio.

Increasing the oxygen partial pressure results in smaller grained films.The oxygen in the sputtering gas causes the reduction in sputtering rate (figure4.3). Negative oxygen ion that are generated at the oxide target and from the O_2 in sputtering gas gain enough energy and are accelerated passing through the cathode dark space [135, 136]. With increasing oxygen partial pressure there is an increase of negative ions which causes the resputtering of the films reducing the growth rate and grain size of the films. Generally the damages on the growing films are mainly attributed to the bombardment of secondary electron emitted from the cathode, the high energy sputtered particle, and negative ions such as oxygen ions in the sputtering gas. The secondary electron effects are minimized in a magnetron sputtering because they are captured around the cathode due to the magnetic field. The high energy sputtered particles can impact and deteriorate the surface of

the growing film when rf power increases over the optimum level. In the present study a constant moderate rf power of 100W was used for sputtering and hence the surface damage due to the sputtered particles can be neglected. The only source of resputtering of the films could be due to the bombarding of the negative oxygen ions.

At very low oxygen to argon ratio there would not be sufficient oxygen to produce stoichiometric films since the growth rate is very high (as compared with 35/65). The films grown in argon without oxygen under the similar conditions were amorphous. There is optimum oxygen to argon ratio for the better growth of perovskite BST thin film.

4.3.2 Composition Analysis

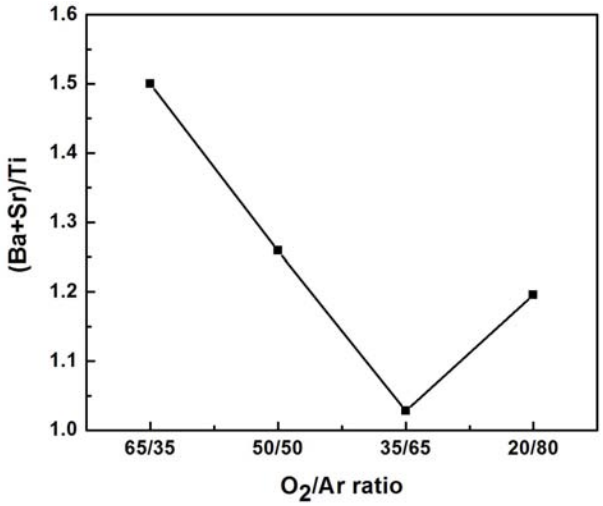

Figure 4.4: Variation of (Ba+Sr)/Ti of the BST thin films with oxygen to argon ratio

The chemical composition of the thin films was analysed using EDX and XPS measurements. EDX is used to calculate the atomic percentage of Ba, Sr, and Ti. The variation of (Ba+Sr)/Ti of the thin films with gas ratio is as shown in figure 4.4. The atomic ratio of (Ba+Sr)/Ti for stoichiometric BST is 1. The ratio for films grown at 35/65 is close to unity (1.02) which indicates that the films grown at this condition are stoichiometric. All the films grown at other oxygen partial pressure the cationic ratio is slightly greater than one.

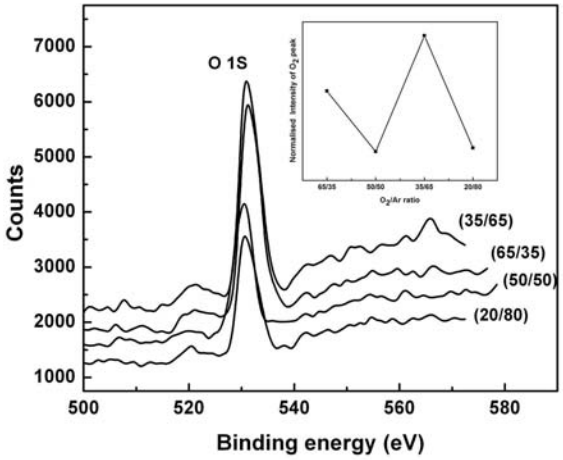

Figure 4.5: The XPS (O1s) peaks of BST thin films sputtered at different oxygen to argon ratio. The inset shows the oxygen content in these films as a function of O_2/Ar ratio.

The oxygen content in the BST films grown at various O_2/Ar pressures during sputtering was estimated using x ray photoelectron spectroscopy (XPS). The XPS of O1s peak is shown in the figure 4.5. Intensity of the recorded peaks of O1s suggests higher oxygen concentration in films de-

posited at O_2/Ar ratio of 35/65. The variation of oxygen content with respect to O_2/Ar gas ratio is plotted as inset in figure 4.5. The XPS results is in agreement with the EDX measurements.The films deposited at O_2/Ar ratio of 35/65 showed the highest oxygen content.

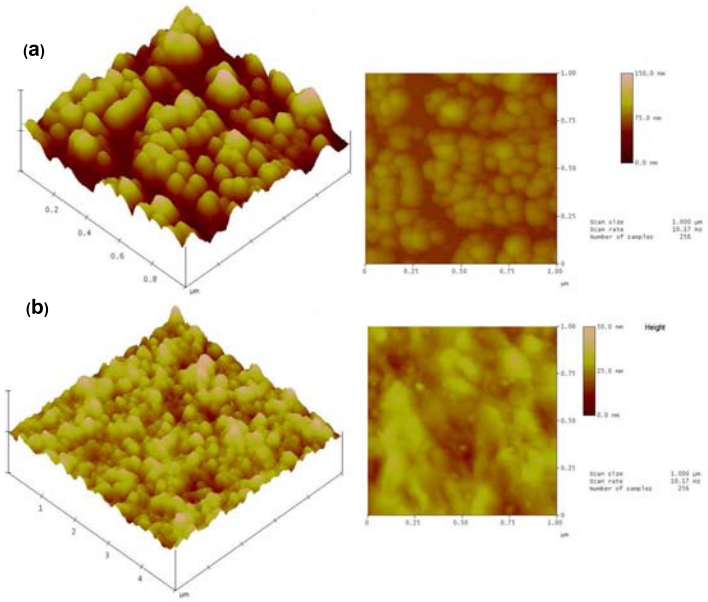

Figure 4.6: AFM picture of rf sputtered BST thin film on (a) Quartz substrates (b) on PtSi substrates at O_2/Ar ratio of 35/65.

The surface morphology of the thin film samples was studied using atomic force microscopy (AFM). The figure 4.6 shows the AFM of the sputtered thin films on quartz and PtSi substrates at O_2/Ar ratio of 35/65. All the films were smooth with an average roughness of about 4nm.

4.3.3 Optical Properties

The transmission spectra of BST thin films show a transparency $> 90\%$ in the visible region (figure 4.7). The transmission spectrum can be divided into two regions: a transparent oscillating region and a region of strong absorption. The oscillating region is the interference fringe due to the interference between the air-film and film substrate interfaces.

The transmission spectrum of BST thin films grown at different oxygen to argon ratio (fig 4.7) reveals a blue shift for the absorption edge with oxygen to argon ratio. The blue shift has close correlation to the grain size of the thin films. The grain size is calculated from XRD using Scherrer's formula. The absorption edge for the films grown at O_2 to Ar ratio 35/65 shifts to longer wavelength which implies a decrease in band gap.

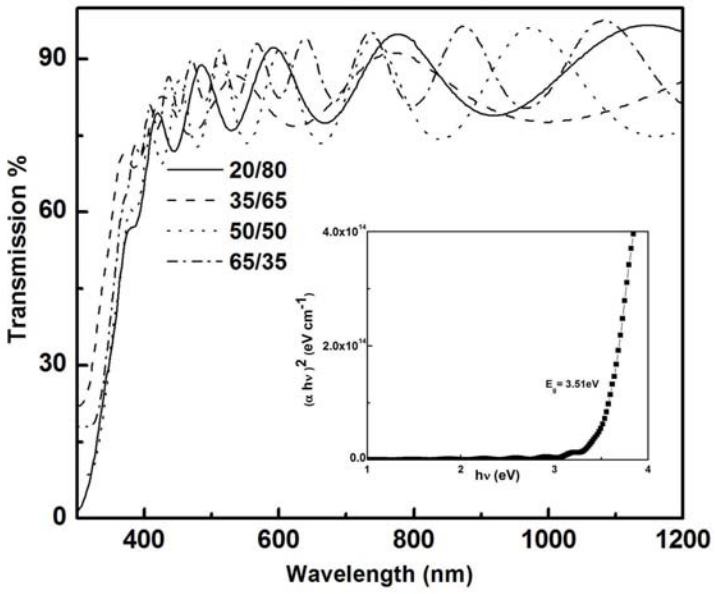

Figure 4.7: Transmission spectrum of BST thin films for various oxygen to argon ratio. Inset shows the typical plot of $(\alpha h\nu)^2$ vs $h\nu$ for thin films.

The bandgap of thin films were determined from the plot of $(\alpha h\nu)^2$ vs $h\nu$ ieby extrapolating the linear portion of the curve to $h\nu$ equal to zero [137]. The variation of band gap as a function of O_2 to Ar ratio and grain size is shown in figure 4.8 . The band gap of BST films is found to increase with increase of oxygen partial pressure during sputtering while the grain size decreases.

Blue shift in the band gap can occur due to several factors such as grain size effect, stress in the films and amorphous nature of the films. It is well known that the stress in thin film decreases with increase in thickness. In the present study the bandgap is found to be independent of the film thickness. Hence the shift in band gap may be attributed to grain size

effect.

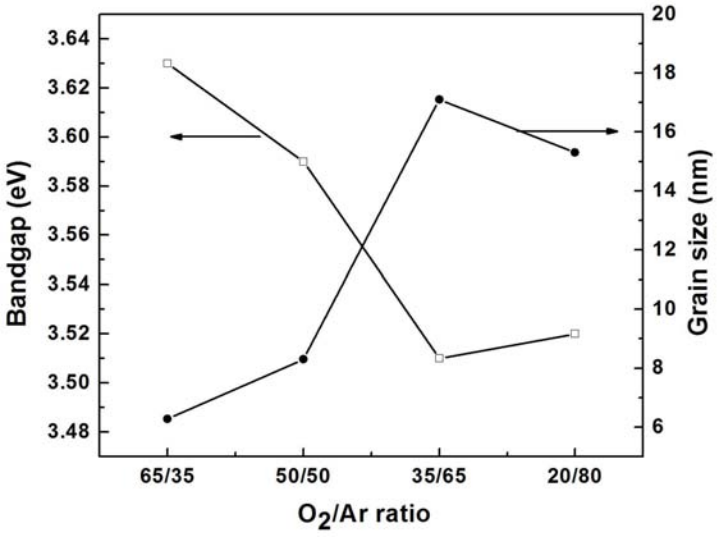

Figure 4.8: The variation of band gap and grain size of BST films with oxygen to argon ratio.

Refractive index (n_f) and excitinction coefficient (k) of the thin film was derived by the envelope method using the theory of Manificer [80] as described in chapter 2. Figure 4.9 shows the variation of refractive index as a function of O_2 to Ar ratio during sputtering. Refractive index is greater (2.10) for thin films deposited at 35/65 ratio. The excitinction coefficient of all the films is in the range 10^{-2}.

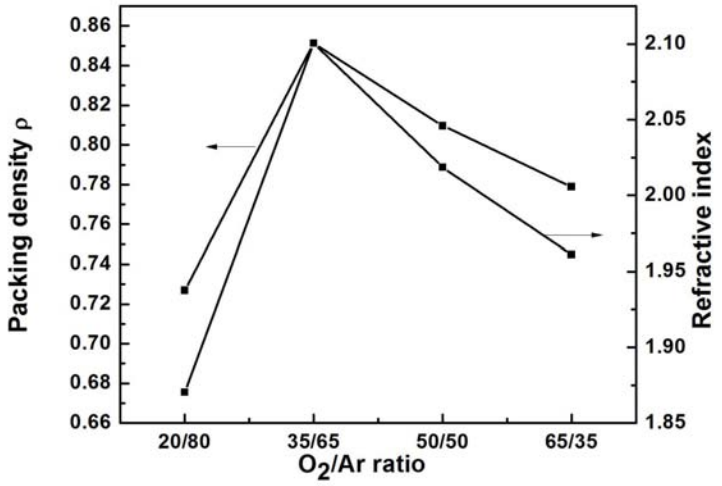

Figure 4.9: Variation of refractive index and packing density with oxygen to argon ratio in rf sputtered BST thin films.

The packing densities of the film and the bulk material can be calculated from refractive index. The packing density (p) is defined as the ratio of the average film density (ρ_f) and the bulk density (ρ_b) (equation 4.2)

$$P = \frac{\rho_f}{\rho_b} \tag{4.2}$$

The correlation between the packing density and the refractive index can be expressed as equation 4.3 [138, 139],

$$P = \frac{\rho_f}{\rho_b} = \frac{(n_f^2 - 1)}{(n_f^2 + 2)} X \frac{(n_b^2 + 2)}{(n_b^2 - 1)} \tag{4.3}$$

Where n_f denotes the refractive index of the film, n_b the refractive index of the bulk. Assuming the bulk value to be 2.46 at 550nm [122] and using the refractive index of the films, the packing density with oxygen to

argon ratio is shown in figure 4.9. The packing density of the BST films is maximum (0.85) when sputtering was carried out at O_2/Ar ratio 35/65. This shows the formation of closely packed structure.

In order to calculate the packing density of the film from the refractive index data, the effective medium model of Bragg and Pippard [140, 141], which takes the growth morphology of the film into account, was used. This model has been very successfully applied previously by a number of workers to explain the deviation in the refractive index values of oxide thin films from the bulk refractive index values [130]. The basic assumption is that the voids are either empty (refractive index = 1) or filled with moisture (refractive index = 1.33). In the current study, both possibilities have been taken into account and it was found that the model of closed packed columnar growth with empty voids provides a good fit.

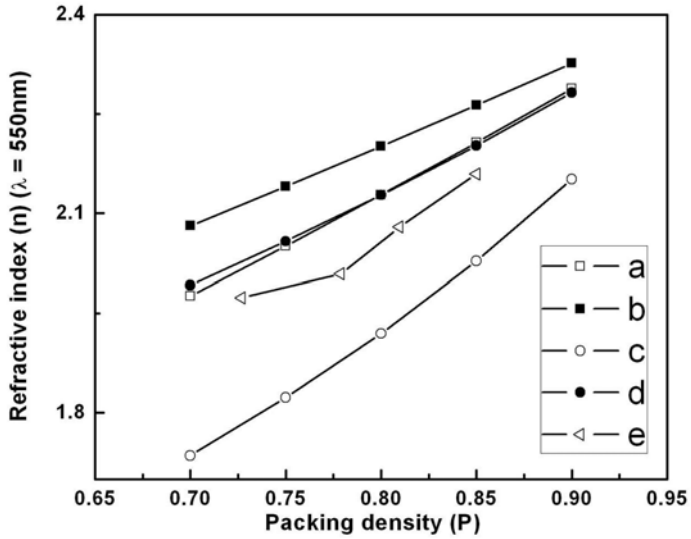

Figure 4.10: Refractive index (at $\lambda = 550$nm) as a function of packing density, P, for two microstructures calculated according to Bragg Pippard model:(a) close-packed columns with empty voids; (b) close-packed columns with moisture filled voids; (c) columnar growth with empty voids; (d) columnar growth with moisture filled voids; (e) observed values for rf sputtered $Ba_{0.7}$,$Sr_{0.3}TiO_3$ films in the present study.

For close-packed columnar grain morphology, the relation is given by

$$n_f^2 = \frac{(n_b^4 P + (2-P)n_b^2 n_p^2}{(2-P)n_b^2 + P n_p^2} \tag{4.4}$$

while for a columnar structure of reduced density it is given by

$$n_f^2 = \frac{((1-P)n_p^4 + (1+P)n_b^2 n_p^2}{(1+P)n_p^2 + (1-P)n_b^2} \tag{4.5}$$

where n_p denotes the refractive index of the voids, which is 1 for empty voids or 1.33 in the case of moisture filled voids.

Figure 4.10 depicts the calculated dependence of refractive index n_f (λ = 550nm) on the packing density, P, for a close packed columnar structure and a columnar structure of reduced density, both with empty and moisture filled voids. The refractive index versus the packing density for the rf sputtered BST films in the present study is also shown in the same figure. A comparison of these reveals that a close fit could be achieved in the packing density by assuming the mode of closed packed columnar growth with empty voids and columnar growth with voids filled with moisture. This assumption is justified by the fact that oxide films deposited by rf magnetron sputtering generally have a columnar growth structure with voids [123, 142]. In the present study the films were deposited at a substrate temperature of 500^0C and hence the presence of moisture filled voids cannot be taken into account. The mode of closed packed columnar growth with empty voids is, therefore, a good fit.

4.4 The electrical properties of rf sputtered BST thin films

4.4.1 Leakage current

Electrical characterization of sputtered BST thin films were carried out by depositing gold electrode on top by using shadow mask. The structure for the electrical characterization is PtSi/BST/Au.

The leakage current of the samples were found from the current - voltage (I-V) curve, where the current is measured at a specified voltage. Capacitor with low leakage current is ideal for microelectronic device application. The

current density versus electric field characteristics of the BST capacitor for the structure PtSi/BST/Au is shown in figure 4.11.

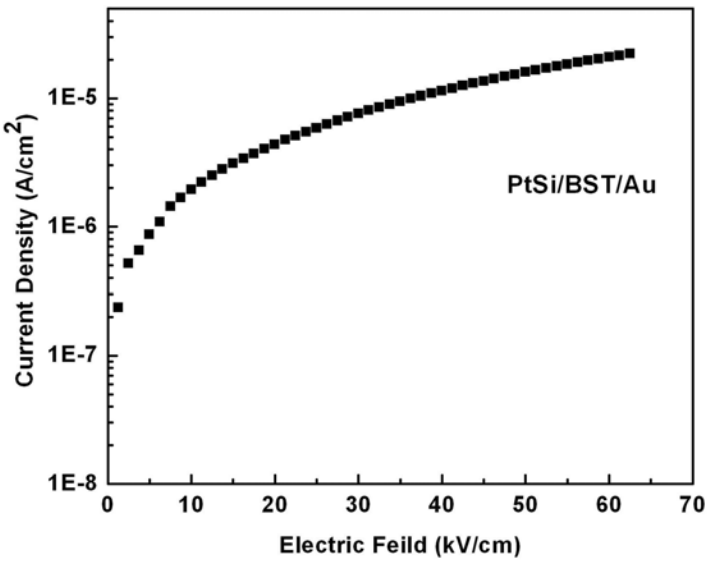

Figure 4.11: The room temperature leakage current with applied electric feild for the device PtSi/BST/Au.

The leakage current density is found to be 500nA/cm^2 at a bias of 3V for 500nm thick BST film. The low leakage current density of the capacitor makes it a potential candidate for DRAM application.

4.4.2 Capacitance Voltage measurements

Dielectric permittivity versus electric field (or capacitance C versus voltage V) loops are often used in the characterization of ferroelectric materials. Measurements of ϵ - E (or C-V) curves are usually made by applying simultaneously on the sample a DC field which changes as a step-like function

and an AC voltage of relatively high frequency (1kHz or above) of small amplitude. The AC voltage is used to measure the capacitance which is then plotted as a function of the DC bias field, giving a C-V graph.

The variation of dielectric constant with voltage (ϵ - E) of BST thin films with PtSi as bottom and Au as top electrode is shown in figure below 4.12 at O_2/Ar ratio 35/65 .

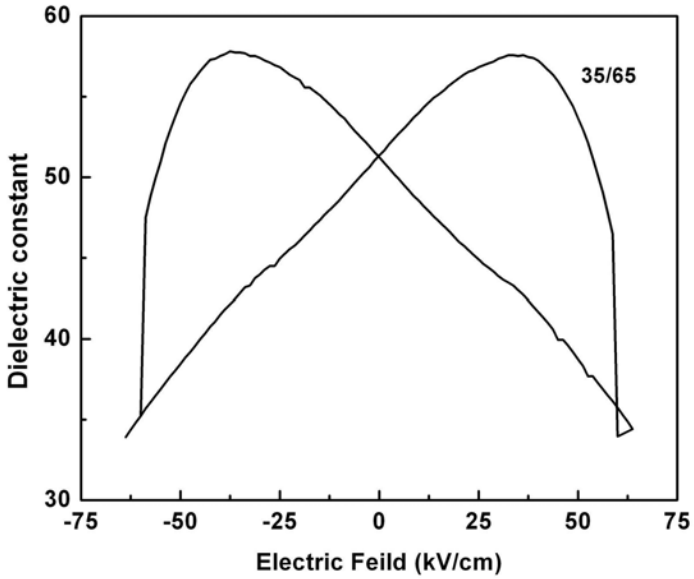

Figure 4.12: The butterfly loop (C-V characteristic) of thin film of the structure PtSi/BST/Au at O_2/Ar ratio 35/65

The bias voltage dependence of dielectric constant reveals that BST thin films have tunable nature as well. The dielectric properties at 1MHz for BST thin films grown at different oxygen to argon ratio at 30kV/cm is shown in figure 4.13.

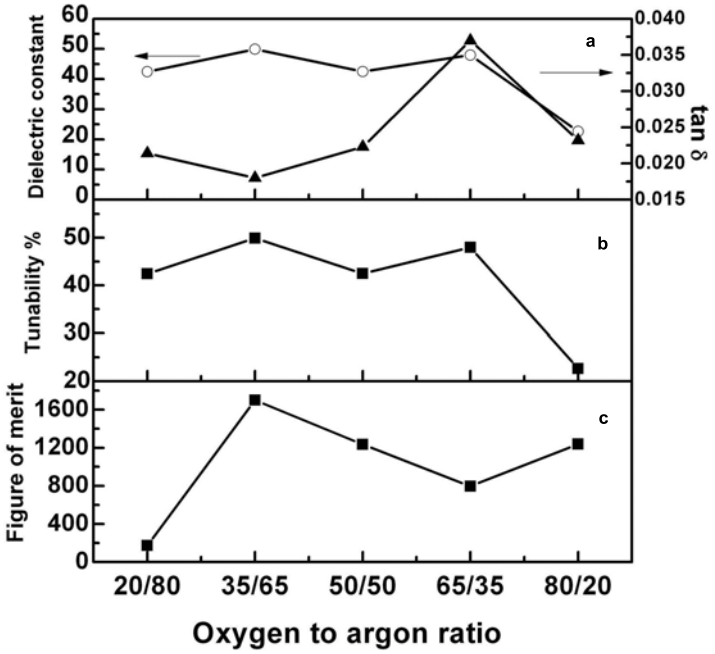

Figure 4.13: The dielectric properties of the BST thin films with O_2/Ar ratio (a) dielectric constant and dielectric loss (b) Tuning (%) (c) figure of merit.

The variation of dielectric constant and dielectric loss of BST thin films with O_2/Ar ratio is shown in figure4.13(a). All the films show smaller dielectric constants. The films deposited at 35/65 showed a maximum dielectric constant at 30 kV/cm and 1MHz. The smaller dielectric constant can be attributed to the smaller grain size of BST thin films. The dielectric loss of films grown at this O_2/Ar ratio is also very low (0.018).

The dielectric constant of all the BST films deposited at different oxygen to argon pressures showed tunable nature.The tunability is defined as the

$$tunability = \frac{[\epsilon(0) - \epsilon(E)]}{\epsilon(0)} X100\% \tag{4.6}$$

where $\epsilon(0)$ and $\epsilon(E)$ are the dielectric constant at zero electric field and at an applied electric field E respectively. The figure of merit is given by

$$K = \frac{\%tunability}{tan\delta} \tag{4.7}$$

The variation of tunability and figure of merit at 30kV/cm and 1MHz with O_2/Ar ratio is shown in figure 4.13 (b) and (c). The high tunability at the optimised O_2/Ar ratio can be attributed to the better crystallinity of BST thin films on PtSi substrates at that O_2/Ar ratio . The low dielectric loss of BST thin films and high figure of merit makes it a promising material for frequency agile application.

4.5 Conclusion

BST thin films were deposited on PtSi and fused quartz by rf magnetron sputtering at various oxygen to argon ratio. The XRD pattern shows that films deposited at room temperature are amorphous. The crystalline films are grown at lower substrate temperature on PtSi substrates than on quartz. The AFM of the sputtered thin films show that the films are smooth with an average roughness of about 4nm. The oxygen to argon ratio has profound influence on crystallinity. The present study shows that there is an optimum value for oxygen to argon ratio for the growth of BST thin films. The oxygen partial pressure during sputtering affects the crystallinity, growth rate and grain size of the BST films. It is found that oxygen to argon ratio of 35/65 shows better structural and optical properties. XPS confirms that maximum oxygen content is for films grown under these optimised conditions. The absorption edge shows a blue shift for smaller oxygen to argon ratio. The band gap for these films varies

from 3.63 to 3.48eV. The refractive index (2.01) and packing density (0.85) was also maximum for films grown at this optimised conditions. Electrical charecterisation of the films were carried out by fabricating PtSi/BST/Au devices. The leakage current of the device showed a good insulating behavior. The variation of dielectric constant with voltage shows the tunable nature of the device. The low loss (0.04) and high figure of merit tunable BST ferroelectric thin films can be used for microwave applications.

Chapter 5

Pulsed laser deposition of BST thin films

Ferroelectric thin films such as BST, PZT and PLZT are extensively being studied for the fabrication of DRAMS due to their high dielectric constant. The large and reversible remnant polarization of these materials make it attractive for nonvolatile ferroelectric RAM application. In this chapter we discuss the characterization of $Ba_{0.7}Sr_{0.3}TiO_3$ (BST) thin films grown by pulsed laser ablation on different substrates. The structural and electrical properties of the fabricated devices were studied. Growth of crystalline BST films was observed on $La_{0.5}Sr_{0.5}CoO_3$ (LSCO) and $La_{0.5}Sr_{0.5}Co_{1-x}Ni_xO_3$ (LSCNO) thin film electrodes at low substrate temperature. PtSi/LSCO/BST/LSCO and PtSi/LSCNO/BST/LSCNO heterostructures were fabricated and the structural and electrical characterizations of these were also carried out. The leakage current and charge storage density is found to be suitable for 64 and 256 Mb DRAM applications.

5.1 Introduction

Ferroelectric oxide thin films with perovskite structure are currently of great technological interest due to their excellent properties for the application in dynamic random access memories (DRAMS)[143]. For tunable device applications, such as varactors, filters, oscillators, and phase shifters, ferroelectric materials, whose working principle is based on the nonlinearity of the internal electrical polarization steerable by an external electric field, have attracted considerable attention.Compared to currently popular tuning elements such as p-i-n diodes, GaAs Schottky diodes or ferromagnetics, ferroelectric components offer the advantages of continuous, quick, low power tunability up to the highest gigahertz frequencies, and easy integration [144, 145].

Barium strontium titanate $Ba_xSr_{(1-x)}TiO_3$(BST) an environment friendly lead-free material is an attractive candidate for microelectronic devices. BST can be integrated to semiconductor technology such as next generation of giga byte dynamic random access memories because of high dielectric permittivity and low dielectric loss [146–148]. BST is the solid solution between barium titanate ($BaTiO_3$) and strontium titanate ($SrTiO_3$) over the entire range of concentration. The dielectric and ferroelectric properties of $Ba_xSr_{(1-x)}TiO_3$ depend on Sr content. At room temperature $Ba_xSr_{(1-x)}TiO_3$) is ferroelectric, when x is in the range of 0.7-1 and is paraelectric when x is in the range 0-0.7 [36]. As a result the electrical and optical properties of BST can be tailored over a broad range for various electronic applications [26].

Ferroelectric thin films have been successfully deposited by rf sputtering [121, 149], metal organic chemical vapor deposition [149], sol gel [146, 149]

and pulsed laser deposition [143, 149–152]. Among these process the laser ablation process is most superior since it posses the advantages viz., lower synthesis temperature, easier in controlling the stoichiometry of thin films, possibility in depositing oxide films of high melting point and the materials of metastable phase [149].

Leakage current characteristics of BST films are also highly influenced by the electrode and film electrode interface characteristics. Deposition conditions, composition and electrode structure play most significant role in leakage current characteristics. Understanding the current transport mechanism is crucial and most of the knowledge is based on the transport across the interfacial potential barrier at the cathode when thermionic field emission or a combination of this is dominant. For all the mechanisms the leakage current density J increases with increasing temperature leading to the increased probability for the electrons to overcome or to tunnel the barrier either at the interface or in the bulk due to higher thermal energy [153].

It is widely accepted that oxygen vacancies play an important role in perovskite ferroelectrics. Though the oxygen ambient is used to prevent the formation of oxygen vacancies in the deposited film, it has been shown that oxide films grown using PLD at high oxygen ambient pressure are still oxygen deficient [151, 152, 154, 155]. The lattice of an O_2 deficient BST film expands beyond the size reported for corresponding bulk ceramics [152, 154, 155]. One of the main technological challenges is to find a suitable electrode material with low electrical resistivity good thermal stability, high resistance to oxidation and good adhesion both to substrate and the ferroelectric film. The interfacial defect layers may originate from accumulation of oxygen vacancies. Under the electric field oxygen vacancies

migrate towards the electrode and aggregate near the electrode interface. The perovskite structured titanate could not afford a large population of point defects [156]. In the case of conducting oxide electrodes or aqueous solution electrodes, oxygen vacancies in the perovskite film in the region near the film electrode interface can be compensated by oxygen from the electrodes. Thus the use of this kind of electrodes inhibits the accumulation of oxygen vacancies at the interface. As a result no interfacial defect layer forms at ferroelectric oxide or ferroelectric aqueous interfaces [156].

Perovskite conducting oxide $La_{0.5}Sr_{0.5}CoO_3$(LSCO) is obtained from ABO_3 perovskite $LaCoO_3$ by partial substitution of La^{3+} by Sr^{2+} [36, 157]. The crystal structure of LSCO is same as that of the perovskite ferroelectrics which makes it a potential candidate as electrode for ferroelectric memory devices. The LSCO which is a conductive oxide electrode act as oxygen vacancy sink for the BST capacitors thereby reducing the fatigue problem usually encountered while using conventional Pt electrode [109, 158–160]. The similar crystal structure of LSCO and perovskite ferroelectrics facilitates the easy growth of ferroelectrics over textured or epitaxially grown LSCO layer [161, 162].

Some problems of porosity and poor adhesion are often reported in BST films and very high temperature thermal treatment is generally required to achieve well-crystallized BST thick films. Such a high temperature process could limit drastically the application potential of these BST films in integrated circuits [26, 144]. Low temperature deposition was achieved for BST thin films with deposition techniques like ion beam sputtering without any oxide buffer layer. But the dielectric constant of these films were low [144]. A low processing temperature is crucial for application of these thin film materials in integrated electronic devices. With oxide buffer layer the

deposition temperature has been reduced and crystallinity was observed without any post deposition treatment at relatively low temperature.

In this chapter the detail study on the growth of ferroelectric $Ba_{0.7}Sr_{0.3}Ti O_3$ (BST) films deposited on PtSi substrates are presented. The electrical characterization of PtSi/BST/Au is discussed. The conduction mechanism and the band structure is studied. BST thin films were deposited on oxide electrode material like $La_{0.5}Sr_{0.5}CoO_3$(LSCO) and $La_{0.5}Sr_{0.5}Co_{1-x}Ni_xO_3$ (LSCNO). This LSCO and LSCNO will serve as an electrode as well as a template for the ferroelectric BST. The films were deposited using both the third harmonics (355nm) as well as the fourth harmonics (266nm) of Nd:YAG laser.

Commercial $Si/SiO_2/TiO_2/Pt$ (PtSi) wafers were used as the substrate for deposition. The structure of discrete capacitors is shown in figure 1.1. Both the top and bottom LSCO electrodes were deposited by rf magnetron sputtering. The sputtering power was kept at 100W with an argon gas pressure of 0.003mbar at 600^0C. The films were crystalline and has a thickness of about 400nm.The resistivity of all the samples were of the order $10^{-5}\Omega$ cm. The detailed growth and characterization of LSCO thin films grown in the laboratory has been reported elsewhere [163].

5.2 Experimental Details

BST thin films were ablated using the third (355nm) and fourth harmonics of Nd:YAG laser(266nm). The repitation frequency was 10Hz with a pulse width of 8-9ns. The laser fluence was kept at $2J/cm^2$.

The target for PLD was prepared by solid state reaction of Barium titanate ($BaTiO_3$) and strontium titanate ($SrTiO_3$). The mixture was

pressed and sintered at a temperature of 1450^0C for 5hrs to obtain $Ba_{0.7}Sr_{0.3}TiO_3$ (BST). The target was fixed at an angle 45^0 to the direction of laser beam and it was rotated at a constant rpm during the laser deposition, so that pitting of the target surface by the laser beam will be uniform. The focused high-energy laser beam ionises the target material and the 'plume" produced spreads out in the forward direction towards the substrates and it is slightly divergent. The substrate was placed at a distance 4cm to the target surface. The gas (oxygen) was bled into the vacuum chamber continuously at a fixed flow rate, while the chamber was simultaneously pumped to maintain a constant background pressure during deposition. The flow of oxygen ambient gas was controlled by a mass flow controller. The substrate temperature (T_s) was varied from 300^0C - 600^0C. The oxygen partial pressure in the chamber is 0.15mbar.

The crystallinity of thin films was determined by X ray diffractometry (XRD) excited with CuK_α radiation ($\lambda = 1.541\mathring{A}$) and surface morphology by AFM and SEM. Thickness of the samples were measured using Dektak 6M stylus profiler. Electrical characterization was carried out using Keithley SMU unit. The dielectric constant was calculated from the capacitance measured at 1kHz using LCR meter and polarization by Sawyer Tower circuit.

5.3 Growth of thin films ablated using 355nm and 266nm

5.3.1 Growth on quartz substrates

To study the optical properties BST thin film are deposited on quartz substrates using third and fourth harmonics of Nd:YAG laser. The crystallinity of these films were compared.

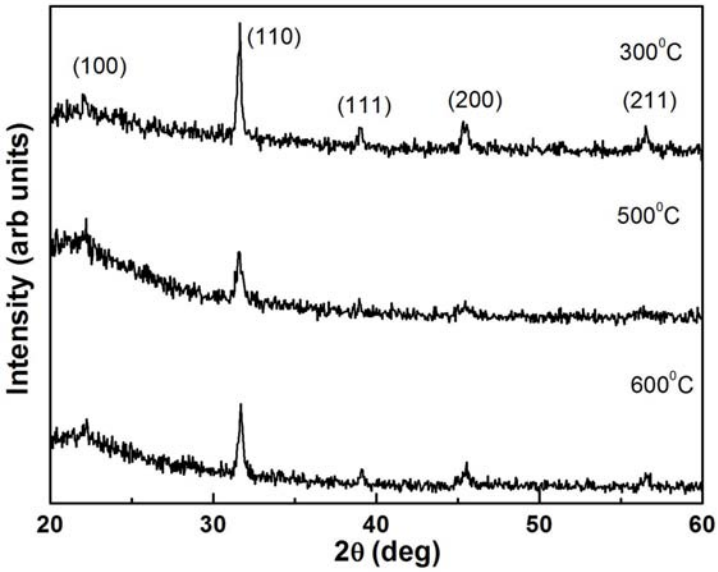

Figure 5.1: XRD pattern of BST thin films grown on quartz substrates at various deposition temperature and post annealed at 600^0C in O_2 atmosphere using 355nm

As deposited films were amorphous on all the films deposited on quartz irrespective of the ablation wavelength used. Hence these films were annealed in oxygen ambience to induce crystallinity. The films were annealed in excess oxygen flow for 1hr at 600^0C. All the films showed perovskite crys-

talline nature on annealing irrespective of the wavelength used for ablation. The thickness of the films were about 800nm.

The XRD pattern of thin films deposited using 355nm of Nd:YAG laser is shown below(figure 5.1). A laser fluence of $2J/cm^2$ was used for ablation The films were deposited at 0.1mbar oxygen pressure at 300^0C and annealed at 600^0C in oxygen ambience. The (100) oriented growth trend is ascribed to the fact (100) plane is a closely packed O_2 plane which has the lowest surface energy in perovskite structure [134].

The XRD pattern (as in figure 5.2) of BST thin film deposited using 266nm also show a similar pattern. In this case also the laser fluence was maintained at $2J/cm^2$. All the films deposited were amorphous and required post deposition treatment. When compared with 355nm the films deposited using 266nm were smooth and better crystalline under the same condition.

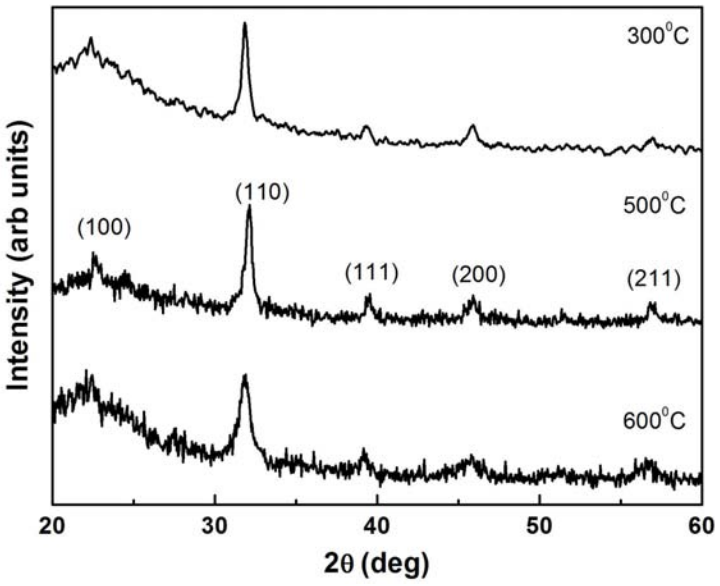

Figure 5.2: XRD pattern of BST thin films grown on quartz substrates at various deposition temperature and post annealed at 600^0C in O_2 atmosphere using 266nm

The oxygen rich phase in perovskite (001) is seen in the films deposited at lower temperature irrespective of the wavelength used for ablation. The grain size of the films were calculated using Debye Scherrer's formula. The films deposited using 266nm show larger grain size than films deposited using 355nm. The variation of grain size with substrate temperature for films deposited using 355nm and 266nm is shown in figure 5.3.

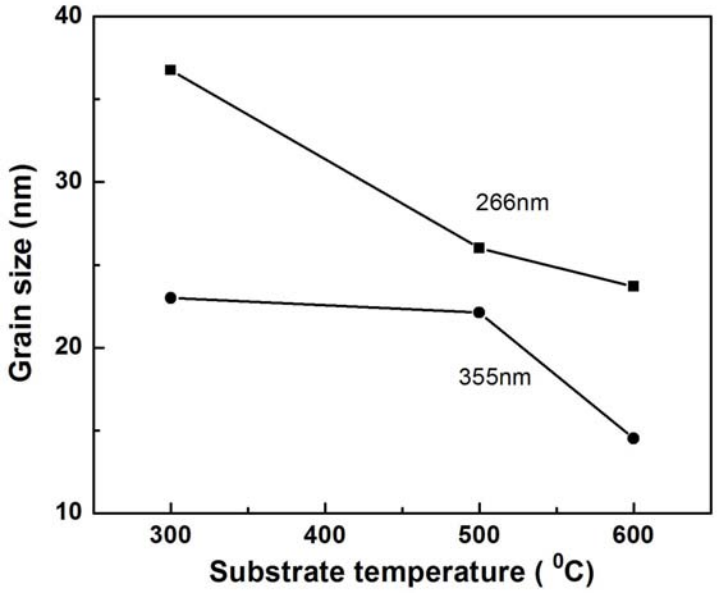

Figure 5.3: Variation of grain size with temperature for BST films grown using 355nm and 266nm of Nd:YAG laser(line for visual guidance only)

5.3.2 Growth on Si substrates

Thin films were grown at various temperatures on Si substrates (100) at 0.1 mbar oxygen pressure. All the as deposited films on Si were found to be amorphous. This may be due to the low oxygen pressure in the chamber during deposition. These films were annealed in oxygen atmosphere at 600^0C for 1hr. The post annealed films were found to be crystalline. Figure 5.4 shows the XRD pattern of BST thin film grown at different temperatures. It can be seen that the crystallinity is better for thin films grown at lower temperature. The preferred orientation of BST thin films at each substrate temperature are determined from the thermodynamical

equilibrium between various depositions variables, including stress occurred on the thin films. The (100) oriented growth trend is ascribed to the fact (100) plane is a closely packed O_2 plane which has the lowest surface energy in perovskite structure.

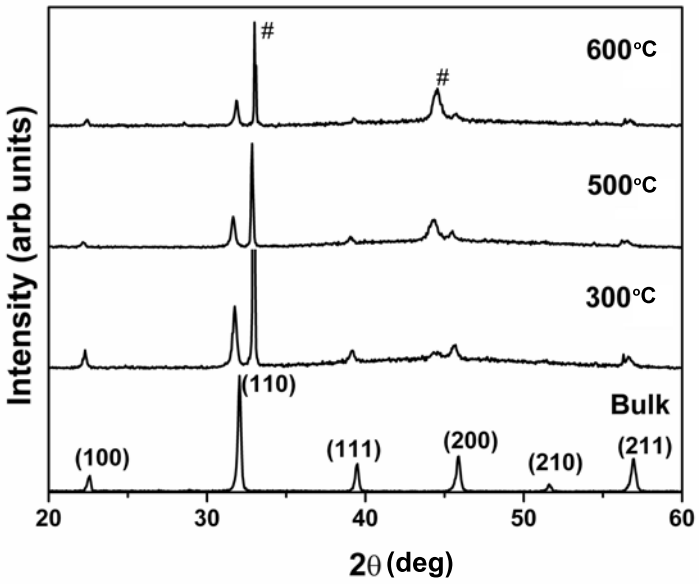

Figure 5.4: XRD pattern of BST thin films grown by ablation using 355nm on Si substrates at various substrate temperatures and then post annealed at 600^0C in O_2 atmosphere.

The thin film BST deposited using 266nm also showed perovskite structure similar to that of figure 5.4. Here also the films deposited at lower substrate temperature on annealing shows better crystallinity.

5.3.3 Growth of BST thin films on Pt Si substrates

PtSi act as a good substrate for the deposition of perovskite oxides. XRD pattern given in figure 5.5 shows the growth of perovskite BST thin films. The films were deposited at a substrate temperature of 600^0C at 0.1mabr. The PLD films were always found to be oxygen deficient which hinders the crystallinity. Hence they need post deposition annealing in oxygen presence. In the present study the as deposited BST films were found to be crystalline even without oxygen annealing. The (100) oriented growth trend is ascribed to the fact that (100) plane is a closely packed O_2 plane which has the lowest surface energy in perovskite structure.

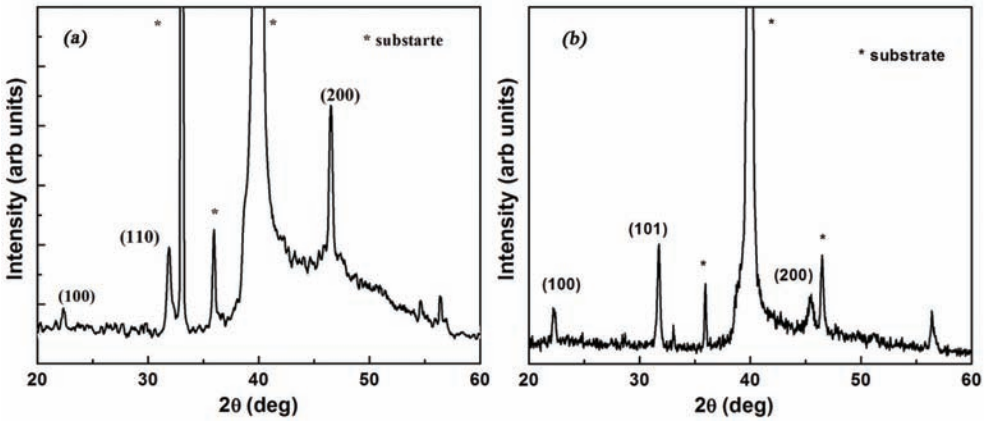

Figure 5.5: XRD pattern of PLD grown BST thin films on PtSi substrates at 600^0C: (a) using 355nm of Nd:YAG laser (b) using 266nm of Nd:YAG laser

The films were deposited using 266nm of Nd:YAG laser as well. The XRD pattern of thin films show perovskite structure. The films show better crystallinity compared to films grown by 355nm laser wavelength all the other conditions being the same.

5.3.4 Growth of BST thin films on oxide electrodes

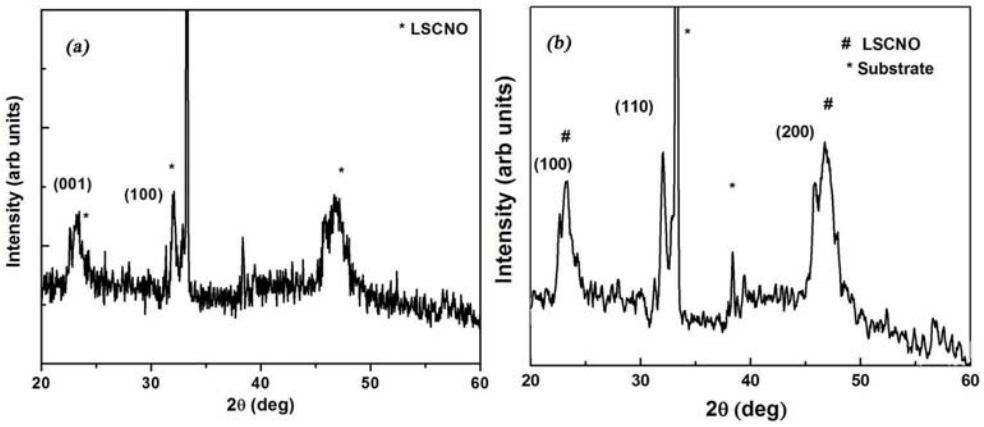

Figure 5.6: The XRD pattern of Si/LSCO/BST and Si/LSCNO/BST grown at 500^0C at 0.1 mbar using 266nm of Nd:YAG laser

BST thin films were deposited on oxide electrodes LSCO and LSCNO using both 266nm and 355nm of Nd:YAG laser. LSCO and LSCNO were deposited using rf magnetron sputtering. The conditions for the growth and the XRD pattern of LSCO and LSCNO is discussed in chapter 3.

BST thin films were grown by PLD at 500^0C at 0.1 mbar oxygen pressure on $La_{0.5}Sr_{0.5}CoO_3$ (LSCO) and on LSCNO electrodes. LSCO was grown on Si (100) substrates using rf magnetron sputtering. The LSCO crystallizes in the perovskite structure. It was found that there is better growth of BST thin films on LSCO and LSCNO electrode. The as deposited films were found to be crystalline without post annealing. A typical XRD pattern of the layers Si/LSCO/BST is shown in figure 5.6

The BST perovskite film were grown at a lower substrate temperature on the LSCO and LSCNO electrodes. These oxide electrodes act both as a

template and as electrode for BST thin films.The perovskite BST thin film has a lattice constant of 3.95$\mathring{A}$. The LSCO materials also has perovskite structure with lattice parameter a = 3.805$\mathring{A}$. Crystalline growth of BST on LSCO thin films is due to the close match among the crystal structure, lattice parameter and atomic arrangements between LSCO layer and BST material [164].

5.4 Surface morphology and composition analysis

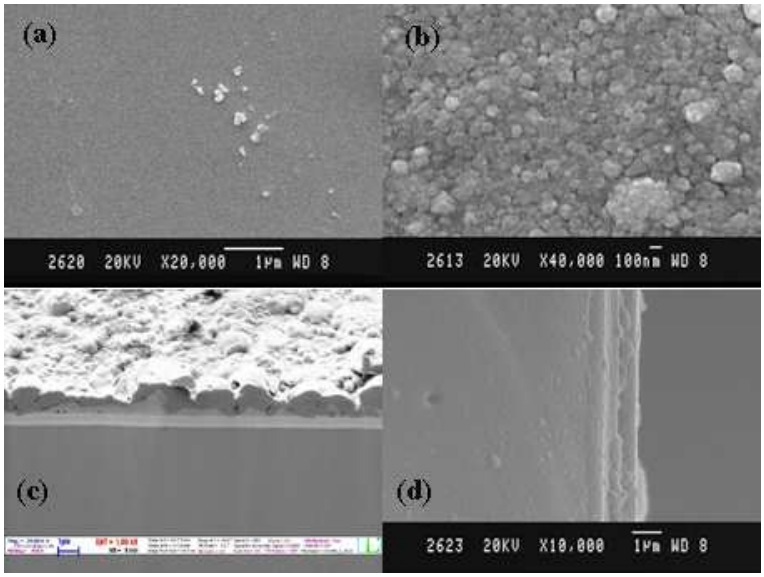

Figure 5.7: SEM image of films (a)ablated using 355nm (b) ablated using 266nm of Nd:YAG laser (c) cross sectional SEM image of Si/SiO_2/LSCO/BST and (d) cross sectional SEM image of PtSi/BST

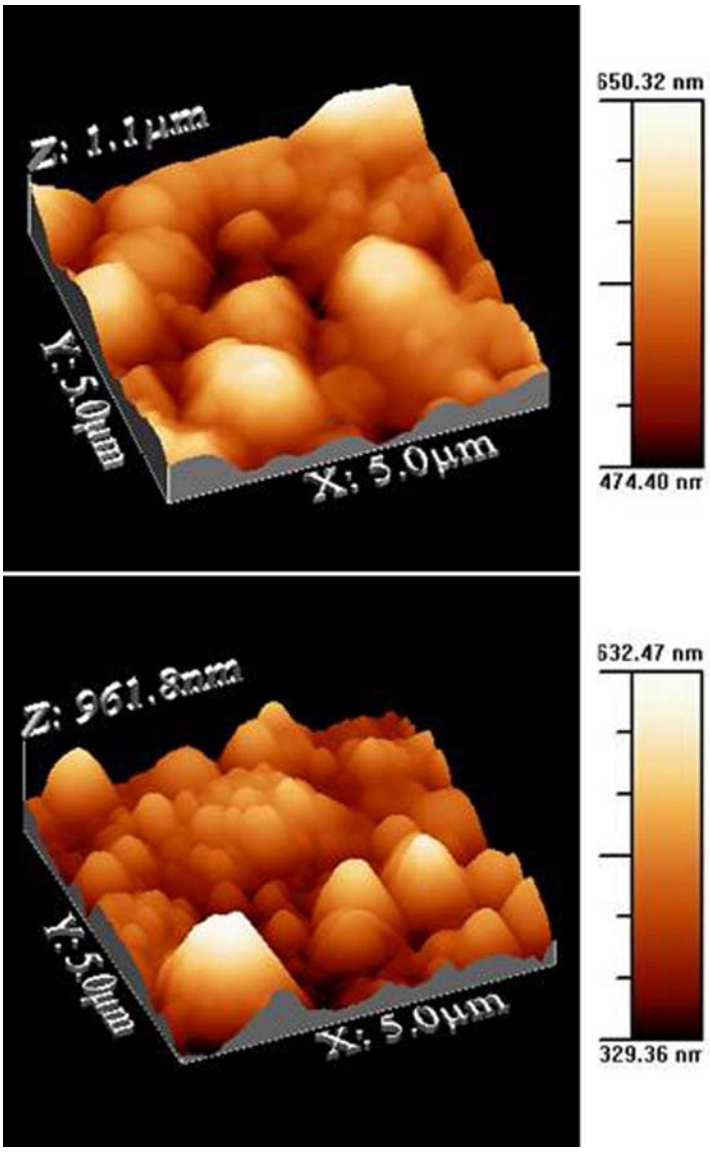

Figure 5.8: AFM image of BST thin films deposited using (a) third harmonics and (b) fourth harmonics of Nd:YAG laser on Si substrates.

Surface morphology of thin films were studied using SEM and AFM images. The cross sectional SEM images were used to study the electrode-film interface. The compositional analysis were carried out using EDX measurements. SEM image of BST thin films shows that the films are smooth. The SEM images of BST thin films deposited using 355nm and 266nm of Nd:YAG laser is shown below(figure5.7).

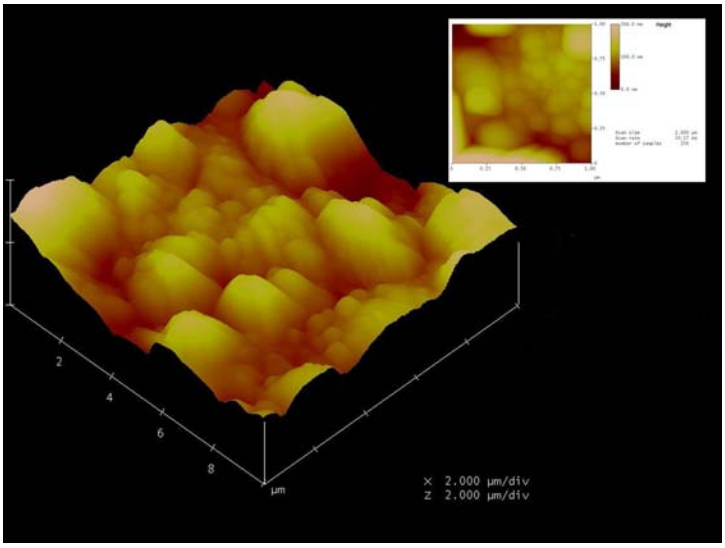

Figure 5.9: AFM image of BST thin films grown on LSCO oxide electrode using fourth harmonics of Nd:YAG laser on PtSi substrates.

The AFM image of BST thin film deposited on Si substrates is shown in figure 5.8. The average roughness of BST thin film deposited using 355nm of Nd:YAG laser on Si substrates is about 29nm and that using 266nm is 22nm. The AFM image of BST thin films deposited on oxide electrode LSCO is shown in figure 5.9. The average roughness was found to be 19nm.

The compositional analysis of thin films shows that the films with per-

ovskite phase has Ba+Sr/Ti ratio approximately 1 irrespective of the substrate used.

5.5 Optical characterization

Optical studies was carried out on BST thin films grown on quartz substrate using UV Vis NIR spectroscopy. The as deposited films do not show good transmission as the films were milky in appearance.

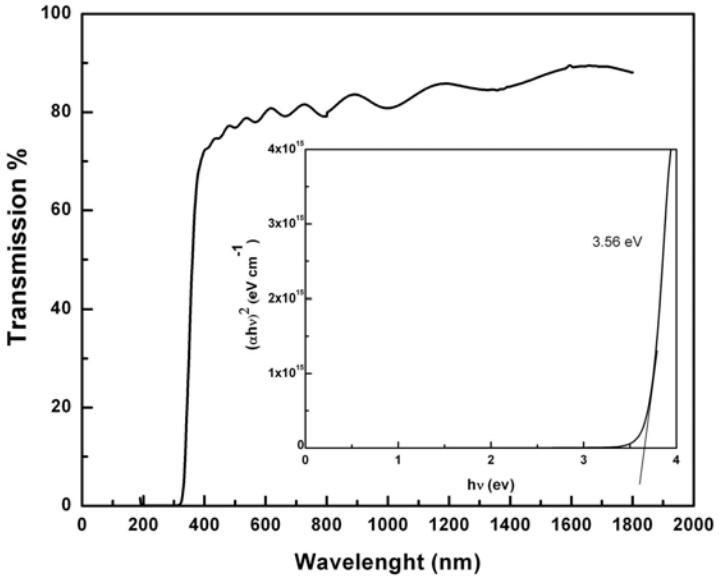

Figure 5.10: Transmission spectra of BST thin films grown by PLD using 266nm on quartz substrates at substrate temperature 300^0C and then annealed at 600^0C in O_2 atmosphere for 266nm

The films deposited on quartz substrates using 355nm of Nd:YAG laser after post deposition annealing show transmission less than 70% in the

visible region.But the films deposited using 266nm and annealed in oxygen ambience showed transmission greater than 85%. The transmission spectra of BST thin films deposited using 266nm is shown in figure5.10.

The band gap of BST thin films is calculated using Tauc plot. The absorption coefficient α is related to the photon energy hν as given by equation (5.1)[137].

$$(\alpha h\nu) = A(h\nu - Eg)^n \tag{5.1}$$

where E_g is the energy band gap and n = 1/2 for direct allowed transitions between valance and conduction band. Inset of figure 5.7 shows the plot of $(\alpha h\nu)^2$ vs hν. Band gap of BST thin films is found to be 3.51eV.

Refractive index (n) of the thin film was derived by the envelope method using the equation 5.2 and 5.3 [80].

$$n = ((N' + (N'^2 - n'^2)^{1/2})^1/2 \tag{5.2}$$

$$N' = 1/2(1 + n_s)^{1/2} + \frac{2n_s(T_{max} - T_{min})}{T_{max}T_{min}} \tag{5.3}$$

where T_{max} and T_{min} are the corresponding transmittance maximum and minimum at a particular wavelength λ and n_s is the refractive index of fused quartz. The refractive index of the thin film was calculated to be about 2.

5.6 Electrical Characterization

5.6.1 Leakage current density

The leakage current of the samples were found from the current – voltage (I-V) curve, where the current is measured at a specified voltage. The leakage

current is an important characteristic of thin film ferroelectric capacitors, it directly limits the charge retention and it influences the ferroelectric hysteresis loop. The leakage current is also a sensitive electrical probe of the material quality of hetrostructure as it is strongly dependent on material aspects of the ferroelectric film and of electrode-ferroelectric interfaces [165]. Capacitor with low leakage current is ideal for microelectronic device application.

Devices are fabricated in the structure PtSi/BST/Au and PtSi/ LSCO/ BST/ LSCO/Au structures for the electrical characterization. The top Au electrode is deposited using a shadow mask by rf magnetron sputtering. The leakage current mechanism in the two device structures are different.

PtSi/BST/Au

The true I – V characteristics was performed by first analyzing the I – t characteristics. As it can be seen from figure5.11, the current value after 100 seconds can be taken to be a near approximation of the true leakage current.

The leakage current of the device PtSi/BST/Au with applied dc voltage is shown in the figure 5.12. The measurement was carried out at room temperature with top electrode negatively biased.The method of obtaining the I – V characteristics was repeated over several electrode dots on the same sample and also samples from different batches to ensure reliability of the obtained data. An analysis of the slope at different regions of the I – V plot in a log – log plot gives an idea of the conduction processes involved under the influence of varying electric fields.

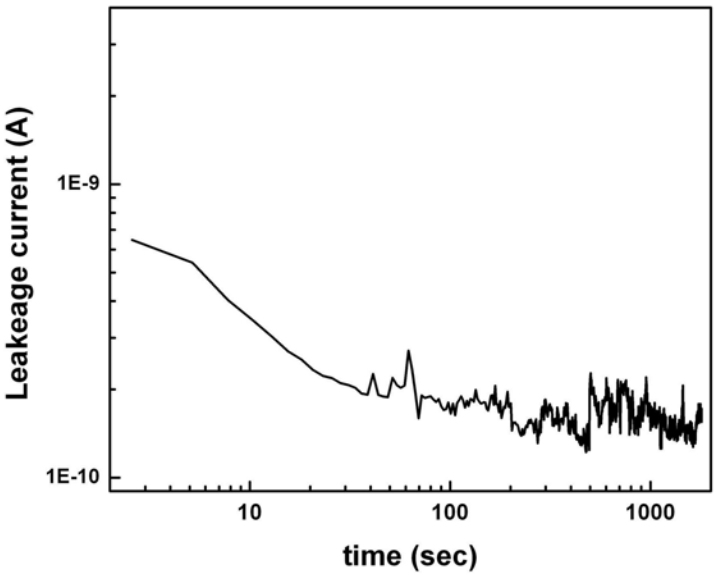

Figure 5.11: Typical I – t curve of PtSi/BST/Au structure for BST thin films deposited at 500^0C at 0.1mbar oxygen pressure

To ensure the universality of the obtained data, the current and voltage values were converted into current density and electric fields J – E and are plotted in figure 5.13. Initially, the leakage current shows an ohmic behavior for low fields. At slightly higher electric fields, there is an onset of non-linearity, the cause of which can be said to be the onset of the space charge limited conduction (SCLC) mechanism.

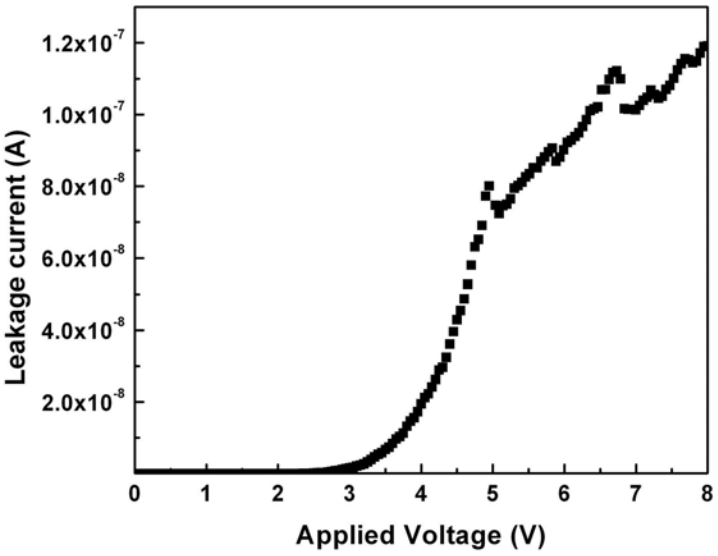

Figure 5.12: The room temperature leakage current with applied dc voltage for the device PtSi/BST/Au

The space charge limited current follows the law

$$I = \frac{V^{(l+1)}}{d^{(2l+1)}} \tag{5.4}$$

$$l = \frac{T_t}{T} \tag{5.5}$$

where, d = thickness and T_t is the temperature parameter characterizing the trap distribution and T is the absolute temperature, for a distributed-trap space-charge limited conduction [36]. The type of trap present can be judged by the behavior of the I – V characteristics of the sample. The presence of grain boundaries usually contribute to the trap distribution, through structural and chemical defects. The verification of this particular process lies in the film thickness dependence characteristics.

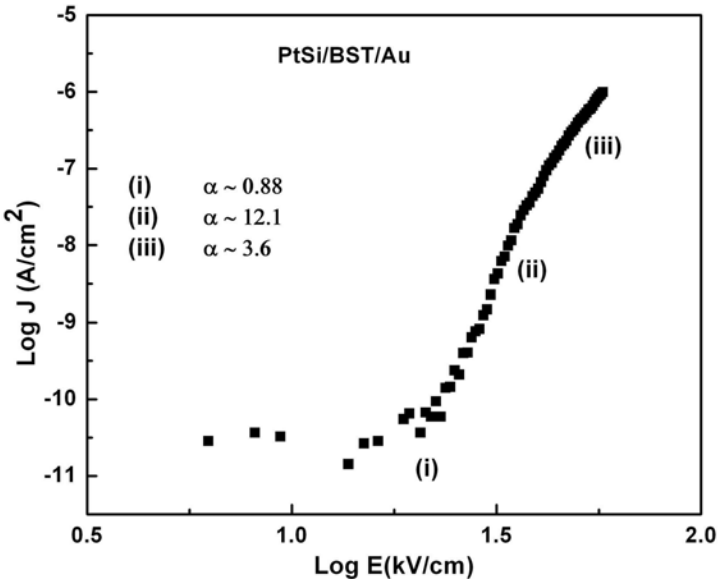

Figure 5.13: The log J versus log E plot of the device PtSi/BST/Au device

Since the film is composed of ultra-fine grains, the space charge mechanism is governed by the size of the grain and not the film thickness. It was already shown that the value of d corresponds to the grain size and not the film thickness [157].

Region (I) corresponds to the low field region, region (II) and (III) corresponds to the intermediate field region and very high field region is not considered here. The corresponding slopes in the different regions are indicated by ohmic in nature, i.e. an enrichment space charge contact. Waser [158], reported that the ultra-fine-grained films are fully depleted of charge carriers and the conduction mechanism is completely electrode controlled. Though, the electrode plays an important role in the leakage current value, yet the presence of grain boundaries and their properties can

variably change the value of the leakage current by orders of magnitude. Further, the conduction mechanism varies for films with different thickness ranges. Films with lower thickness ($< 0.1\mu$m) repeatedly show electrode limited conduction process, while films with higher thickness tends to be dominated by bulk properties. This can be attributed to the fact that complete depletion [158] of the film takes place if the film thickness is less, while for thicker films, the film is not completely depleted.

The current equation, governing the Schottky mechanism is given by [158].

$$J = A^{**}T^2 exp(\alpha E^{1/2-W_b})/k_b T) \tag{5.6}$$

$$\alpha = \sqrt{\frac{q^3}{4\pi\epsilon_r\epsilon_0}} \tag{5.7}$$

$$W_b = W_m - q\chi \tag{5.8}$$

where, A** is the effective Richardson constant which incorporates carrier mobility, T is the absolute temperature, E is the applied electric field, W_b is the zero field barrier height, k_b is the Boltzmann constant, q is the electronic charge, ϵ_0 is the permittivity of free space and ϵ_r is the relative dielectric constant.W_m is the work function of the metal electrode and χ is the electron affinity of the insulator.

For $SrTiO_3$ and $BaTiO_3$, the reported value of the electron affinity are $q\chi_{SrTiO_3}$ = 4.1 eV [159] and $q\chi_{BaTiO_3}$ = 2.45 eV [160], respectively. Assuming the electron affinity of the BST film to be very nearly equal to $SrTiO_3$, the barrier height is around 1 eV for the Au contact. The value of the barrier height justifies the presence of a Schottky or blocking contact at

the metal insulator interface. A charge depletion region is thus formed near the interface to account for the difference in the Fermi level of the insulator and the metal. Since the film is composed of numerous grains along the thickness each grain boundary contribute to the effective potential barrier for the conducting electron. Thus the behavior can be effectively viewed as the combined effect of the grain, grain boundary interfaces as well as the electrode interface.

In polycrystalline sample the deposited films can be thought of a series of grains, grain boundaries, and electrode interfaces. The field dependence of conductivity, or the J – E characteristics, of the films is a combined response of these three parts. Variations in the influences of different parts give rise to variation in J – E characteristics.

In the low field region (i) in the figure 5.13 the film shows ohmic nature. At room temperature, it can be assumed that enough charge carriers are present within the film, so as to contribute to the conduction process and hence a linear field dependence of conductivity can be observed.

The onset of the non-linear character for both types of contacts lie within region(ii) in the figure 5.13 , where a prominent role of the electrode is revealed. The onset of non-linearity is a combined effect of the Schottky emission through the contact interface and the SCLC mechanism within the bulk. The leakage current in the films is dominated by space charge limited current (SCLC) mechanism which can be expressed in the following form [109].

$$J = \frac{9\mu\epsilon_0\epsilon_r E^2}{8d} \tag{5.9}$$

where J is the leakage current density, μ is the charge carrier mobility,

ϵ_0 is the permitivity of free space, ϵ_r is the dielectric constant of the film and d is the film thickness.

Band Structure

In terms of the energy-band picture, the function of the insulator is to raise a potential barrier between the electrodes, extending from the electrode Fermi level to the bottom of the conduction band of the insulator. This barrier impedes the flow of electrons from one electrode to the other, which would normally flow virtually unimpeded in the absence of an insulator (i.e. metal–metal contact). Then the height of the potential barrier is an important parameter in conductivity studies in metal-insulator systems. The shape of the potential barrier just within the surface of the insulator depends on whether or not the insulator is intrinsic or extrinsic, and on the relative magnitudes of the work functions of the metal and insulator. The mechanism of blocking or Schottky contact arises when the work function of the metal is higher than that of the insulator, which results in an outflow of electrons from the insulator to the metal contact to establish thermal-equilibrium conditions. A space-charge region of positive charge, the depletion region is thus created in the insulator and an equal negative charge resides at the metal electrode. If the insulator is thick enough, or the doping density is high, the depletion region at the interface effectively screens the interior of the insulator. Under these conditions, the interior of the insulator is field-free, and the bottom of the conduction band attains its equilibrium position above the Fermi level within the interior [36].

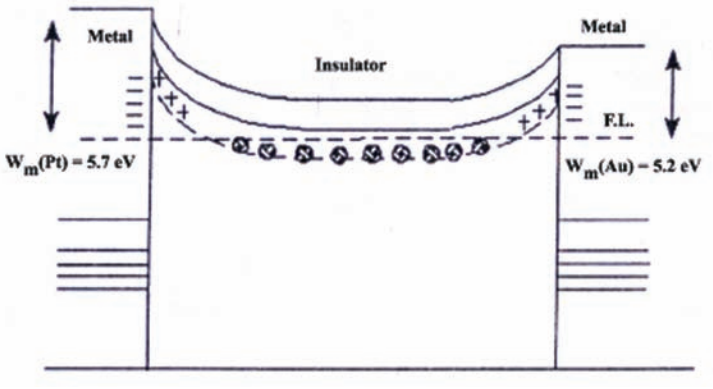

Figure 5.14: Energy band structure of the Pt/BST/Au sturucture

Figure 5.14 shows the band structure of the metal-insulator-metal contact as proposed by Saha et al [36]. Considering the band structure as shown in figure where the depletion region is very thin and the bulk resistance is quite high due to the presence of traps, it is possible to observe electrode to bulk-limited transition in the conduction process [161]. For initial voltage bias in the low to intermediate field region, the conduction process will be electrode-limited because of the high cathode-insulator barrier. The electrode-limited conduction process is by simultaneous thermal excitation of electrons from the cathode over the interfacial barrier with the barrier lowering effect due to the electric field. In that condition, the conduction process is purely a Schottky type and the J–E characteristics (as shown in Figure5.13) are revealed which shows the effect of the blocking contact. At higher fields one of the two process can occur. If the barrier at the Fermi level becomes thin enough, field emission of electrons from the cathode to the conduction band of the insulator can take place or impact ionization can take place in the depletion region when the voltage

bias exceeds $3E_g/2$, where E_g is the band gap of the insulator. Both these processes are characterized by a rapid increase in current with applied voltage, i.e. the contact resistance decreases extremely rapidly with increasing field. The electrode-limited process does not continue indefinitely, since the bulk resistance decreases much more slowly with increasing field than does the contact. Thus at some field, there will be a transition from the electrode limited process to the bulk-limited process, where the contact resistance falls to the value equal to that of the bulk and the voltage across the sample is equally shared between the contact and the bulk. Thereafter, all the voltage in excess of the transition voltage falls across the bulk and the remaining across the barrier, just sufficient to ensure current continuity throughout the system [36].

PtSi/LSCO/BST/LSCO

The current density versus electric field characteristics of the BST capacitor for the structure PtSi/LSCO/BST/LSCO is shown in figure 5.15.The leakage current density of BST thin film capacitor with LSCO electrode is found to be 200nA/cm^2 at a bias voltage of 2V for 800nm thick BST film. The low leakage current density of the capacitor with LSCO electrode makes it a potential candidate for gigabit density memory [166].

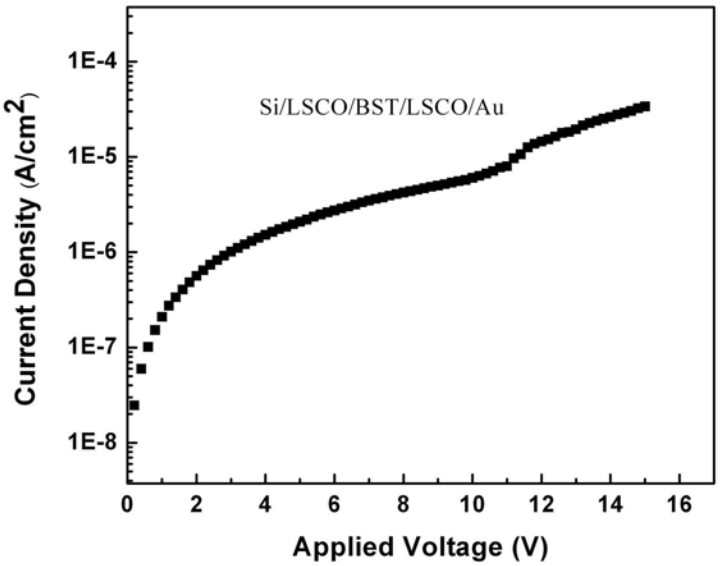

Figure 5.15: The room temperature leakage current density with applied field for the device PtSi/LSCO/BST/LSCO

The applied voltage can be divided into two regions based on the increase of Log J with V viz a low voltage region and a high voltage region. Here Log J increases with V in the low voltage region at a small rate as well as in the high voltage region.

Log J vs Log V plots of the capacitor shown in the figure 5.16 describes the leakage current mechanism in the low voltage region. In the low voltage regime the graph is linear with a slope of 1.31eV. The contact LSCO/BST can be considered to be ohmic like under low field strength. At high voltage the distribution of electrons between LSCO and BST can be disturbed and the leakage current deviates from ohmic behavior. In the high voltage region the conduction mechanism is dominated by Pool Frenkel mechanism.

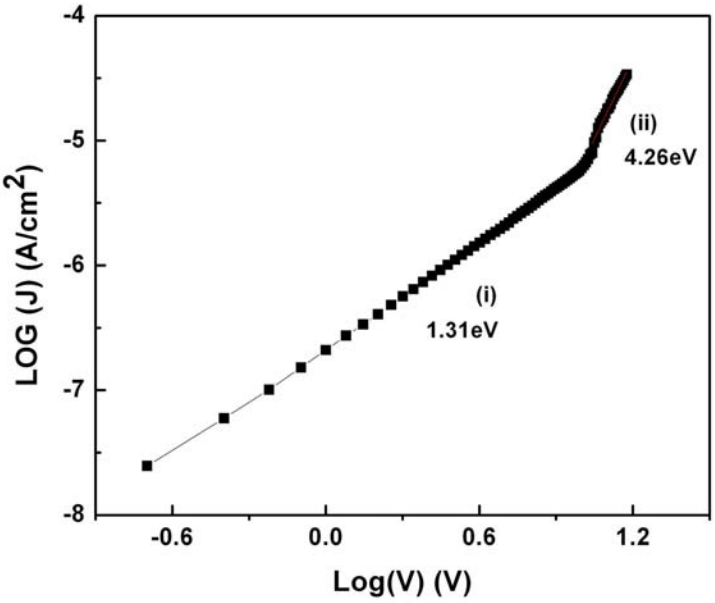

Figure 5.16: Variation of Log J for PtSi/LSCO/BST/LSCO as a function of Log V

To ensure the Pool Frenkel conduction mechanism,the data in the figure 5.16 is replotted as Log(J/E) vs $\sqrt{V}$ as shown in figure 5.17. The log(J/E) curve show small increase with $\sqrt{V}$ in the low voltage region. At high voltage the values increases linearly with $\sqrt{V}$. The variation of Log J with measurement voltage as a function of temperature is shown in figure 5.18. The variation of Log(J/E) with 1/T for various voltages is plotted. All the films showed good linearities with negative slopes suggesting thermally activated leakage current mechanism are operative. A typical plot of Log(J/E) with 1000/T at 50kV/cm is shown in figure 5.19. The activation energy is calculated from the slope of the this plot. The activation energy is about 1.21eV for a voltage of 50kV/cm.

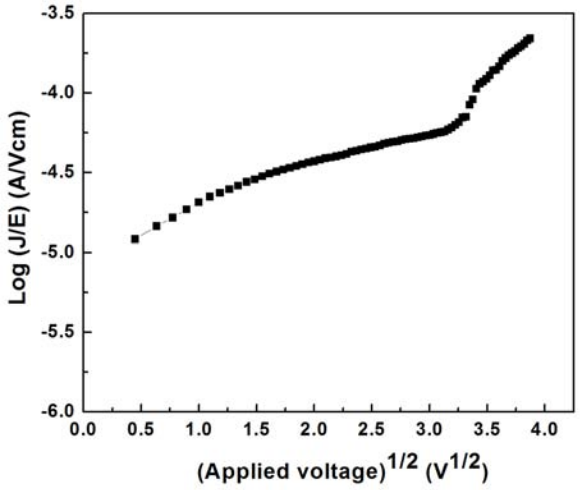

Figure 5.17: Variation of Log J/E as a function of $\sqrt{V}$ for the device PtSi/LSCO/BST/LSCO

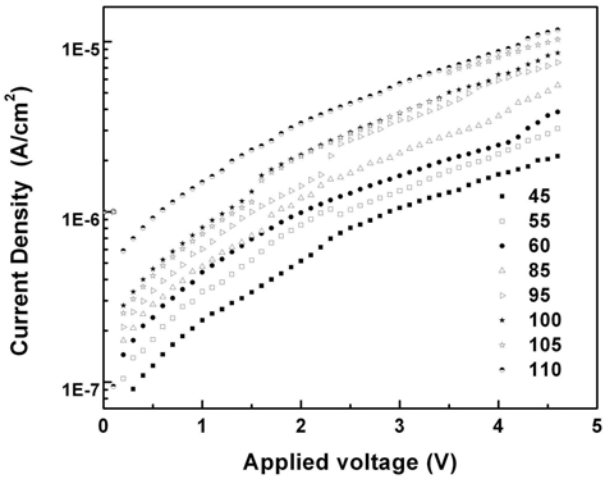

Figure 5.18: Variation of Log J as a function of voltage with temperature for the device PtSi/LSCO/BST/LSCO/Au

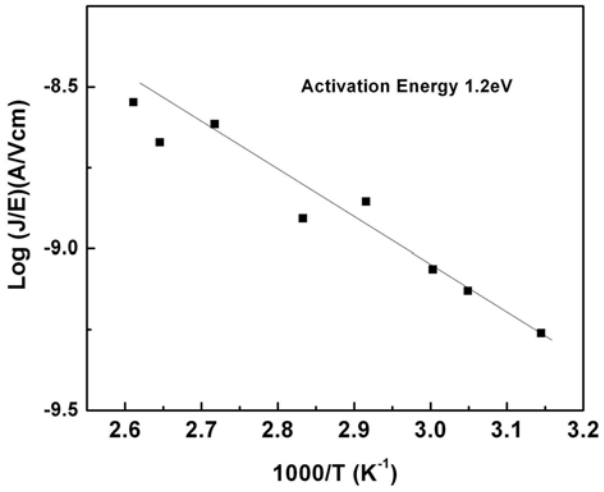

Figure 5.19: Variation of Log J/E as a function of 1000/T for the device PtSi/LSCO/BST/LSCO/Au at 50kV/cm

The activation energies at each voltage are calculated from the slopes of each plot. The activation energy as a function of $\sqrt{V}$ is plotted in figure 5.20. This figure shows the two different leakage current mechanism operating in the high and low voltage regions. In the high voltage region the activation energies decrease in a linear fashion with $\sqrt{V}$ with larger absolute values than those in the low voltage regions. Mean square linear fitting for the high voltage region when extrapolated to V = 0 gives the activation energy at V=0 as 1.3eV.

In the low voltage region the linear decrease in activation energy with square root of the applied voltage suggests that the conduction is not purely ohmic but rather a type of field enhanced thermally activated process may be involved.

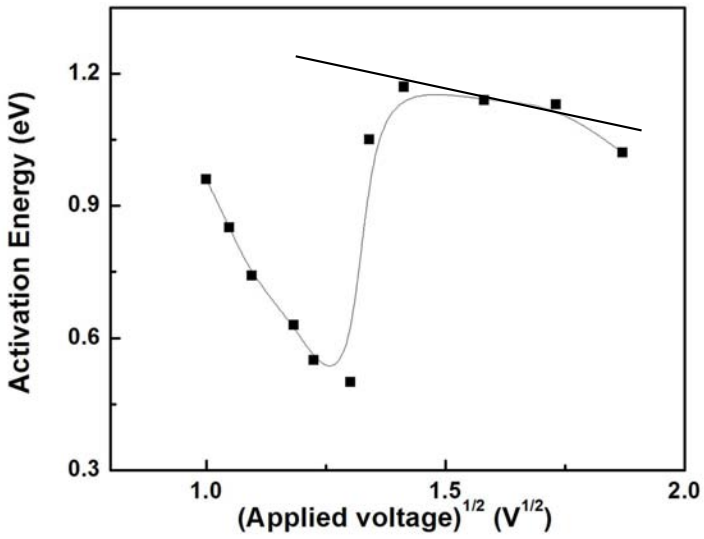

Figure 5.20: Variation of the activation energy for the device PtSi/LSCO/BST/ LSCO/Au as a function of $\sqrt{V}$

This may be the reason for the slope being larger than 1 in the log J log V plot(figure 5.16). At high voltage region the leakage current deviates from ohmic or ohmic like behavior. The activation energy in the high voltage region decreases linearly with $\sqrt{V}$ suggesting that a field enhanced thermally activated process is responsible for electrical conduction in this region. The slopes of the plot log J-log V and that obtained by extrapolation of activation energy to V =0 are the same. At high voltages the the electrical conduction mechanism can be attributed to Pool Frenkel emission mechanism.

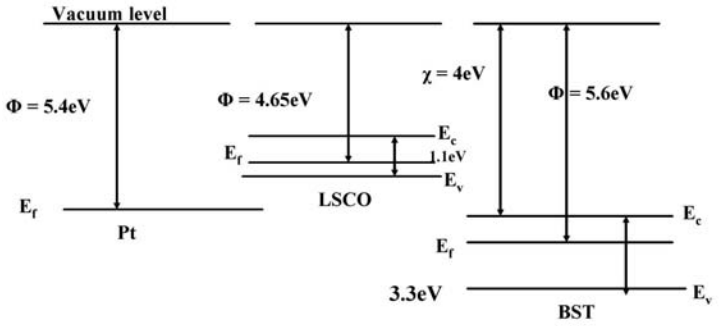

Figure 5.21: Energy band diagram for the PtSi/LSCO/BST/LSCO device structure

A band structure based on the conduction mechanism is proposed in the present study. The ohmic nature of LSCO/BST implies that the surface states of the BST in contact with LSCO is different from metal electrode. The main difference is in the chemical bonding nature of the BST with oxide electrode. The oxygen ions in the LSCO strongly interact with oxygen and cations in the BST thus forming chemical bonds. In the case of metal/BST the chemical states of the surface dangling bonds can be preserved after contact formation but on LSCO/BST most of the dangling bonds disappear due to the interaction of oxide electrode with BST [167]. The contact between BST and LSCO is ohmic as observed in figure5.16. The oxygen vacancy concentration is reduced and the Fermi level is located closer to the center of the energy band. The LSCO can release oxygen to the oxygen deficient BST during the film formation. Figure5.21 shows the schematic energy bands for PtSi/LSCO/BST/LSCO devices.

5.6.2 Dielectric constant

In order to measure the capacitance several heterojucntions were fabricated viz PtSi/BST/Au, PtSi/LSCO/BST/LSCO were fabricated. The dielectric constant estimated using the relation

$$C = \frac{A\epsilon\epsilon_r}{d} \tag{5.10}$$

Where C is the measured capacitance in Farads,ϵ the free space dielectric constant (8.85x10^{-12}Fm), A the area of the capacitor (m^2) and d (m) the thickness of the ferroelectric thin film.

PtSi/BST/Au

The variation of dielectric constant with frequency for PtSi/BST/Au device is shown in figure 5.22. The dielectric constant is low for PtSi/BST/Au capacitors.

The dielectric constant of the crystallized BST films were found to be around 1436 at a frequency of 100kHz. As compared to sintered pellets of BST, the dielectric constant was found to be low, which is a consequence of the small grain size of the grown films. The dielectric constant showed dispersion with frequency which is due to the presence of internal interfacial barriers [162]. It can be seen from the figure that there is a tendency of decrease in the dielectric constant with increase in frequency, which suggests that at higher frequency the contribution from a possible dc conduction contribution decreases.

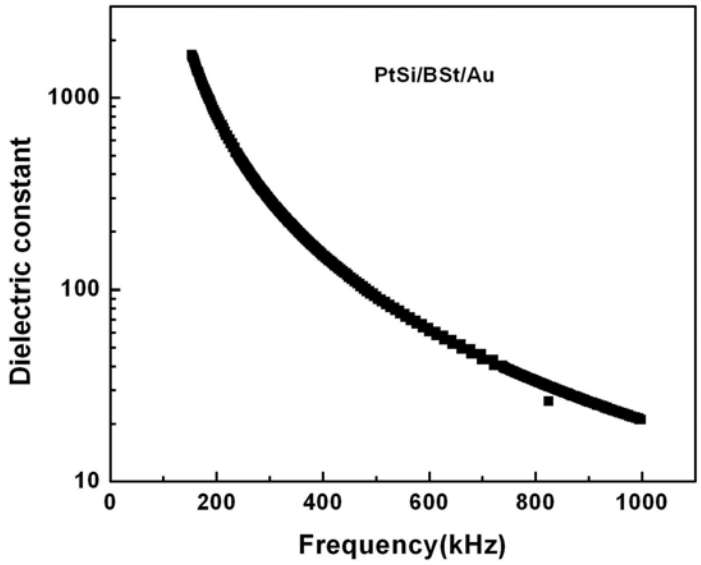

Figure 5.22: The capacitance-frequency variation of BST thin films deposited on PtSi/BST/Au devices

PtSi/LSCO/BST/LSCO

PtSi/LSCO/BST/LSCO structure showed appreciable capacitance with minimum loss. The variation of dielectric constant measured with PtSi/ LSCO/ BST/LSCO capacitor configuration with the BST film grown by PLD is shown figure5.23.

The dielectric constant of the crystallized films were found to be around 628 and the dissipation factor around 0.04 at a frequency of 100kHz. As compared to bulk values the dielectric constant was found to be low, which is a consequence of the small grain size of the grown films. The dielectric constant and the loss tangent do not have noticeable dispersion with frequency, indicating good quality of the present film and the absence of

internal interfacial barriers. However it can be seen from the figure that there is a tendency of decrease in the dielectric constant with increase in frequency, which suggests that at higher frequency the contribution from a possible dc conduction contribution decreases.

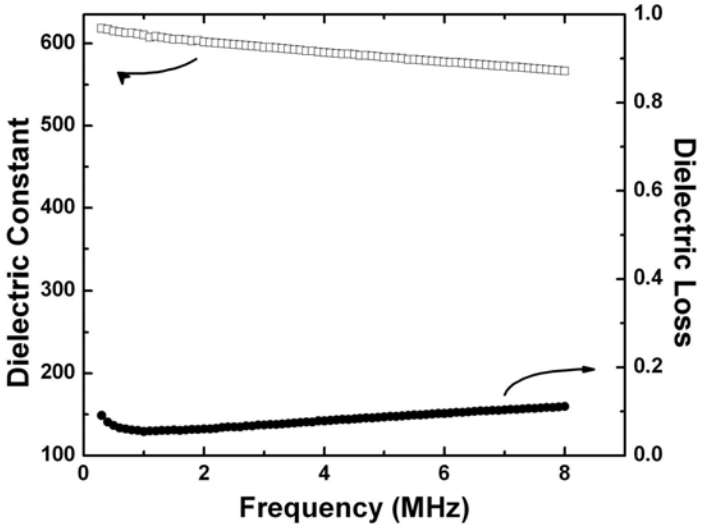

Figure 5.23: The variation of dielectric constant and loss with frequency for BST films deposited on oxide electrode

From the figure it can be seen that the dielectric constant is better for films grown on oxide electrodes. It was found that the loss is minimum for the capacitor fabricated with LSCO electrodes. This may be due to the better growth of BST thin films over LSCO electrodes. Several devices were fabricated on Si as well as on quartz substrates. Figure 5.24 shows the variation of dielectric loss with frequency for the BST capacitors fabricated on various substrates.

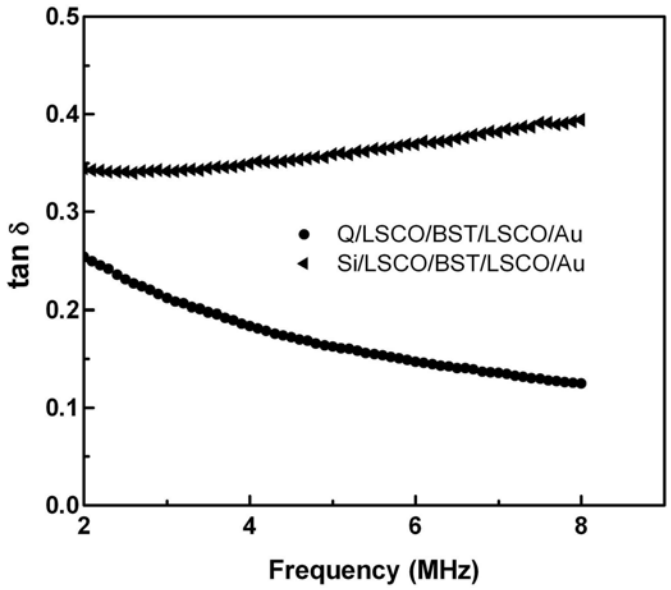

Figure 5.24: The variation of dielectric constant and loss with frequency for films deposited on oxide electrode on quartz and Si substrates

The dielectric loss is found to be minimum for Quartz/LSCO/BST/Au heterojunction. It can be seen that the films deposited on quartz show lower loss but its dielectric constant is also lower compared to PtSi/LSCO/BST/LSCO.

The ferroelectric property of the BST thin films on oxide films in the configuration PtSi/LSCO/BST/LSCO has been studied.

Figure 5.25 shows the room temperature dielectric constant ϵ and dissipation factor tan δ as a function of the applied dc electric field where the relative dielectric constant ϵ_r was calculated from the capacitance data using the classical formula of parallel-plate capacitors. The capacitance - voltage characteristics of the BST films were measured at a frequency of 1kHz. Hysteresis was observed in the films showing the ferroelectric phase

at room temperature. The dielectric properties BST thin films are highly tunable through the application dc bias field.

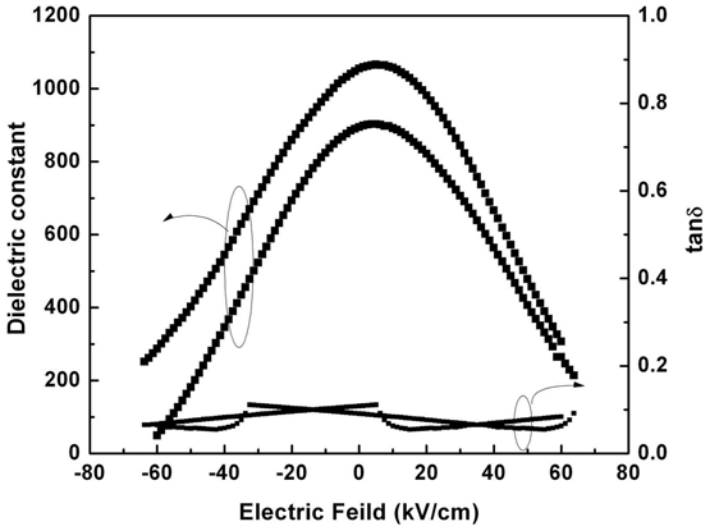

Figure 5.25: Variation of dielectric constant and dielectric loss of PtSi/LSCO/BST /LSCO structure measured at 1kHz

The tunability is defined as the

$$tunability = \frac{[\epsilon(0) - \epsilon(E)]}{\epsilon(0)} \times 100\% \tag{5.11}$$

where $\epsilon(0)$ and $\epsilon(E)$ are the dielectric constant at zero field and at an applied field E respectively. The variation of tunabiliy and figure of merit with the dc field is shown in figure 5.26.

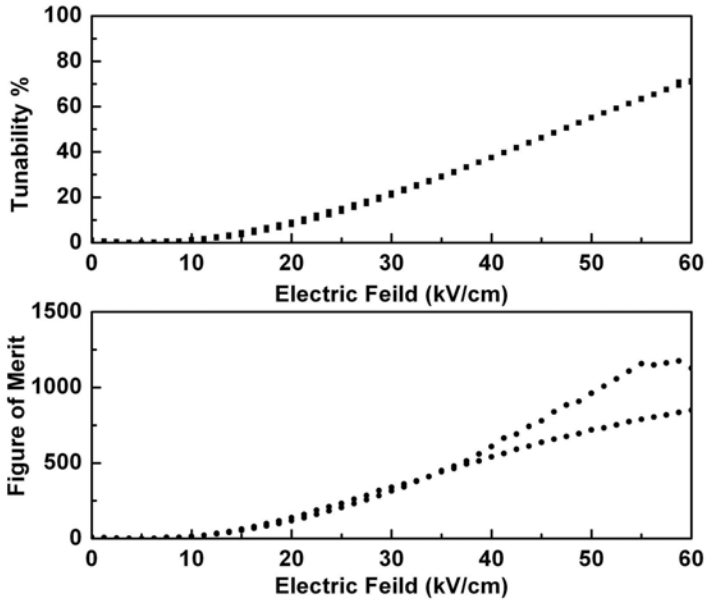

Figure 5.26: Variation of tunability and figure of merit of PtSi/LSCO/BST/LSCO structure with dc bias voltage

The films show high tunability and figure of merit with oxide electrode. High value of tunability can be attributed to the better growth of BST thin films on oxide electrode.

5.6.3 Polarisation

PtSi/BST/Au

The ferroelectric property of the BST thin film was examined in metal ferroelectric metal MFM configuration. Figure 5.27 gives the room temperature P - E characteristic of the BST film. A saturated P-E hysteresis loop is obtained with a remnant polarization of $1\mu C/cm^2$ and coercive field

of 45kV/cm.

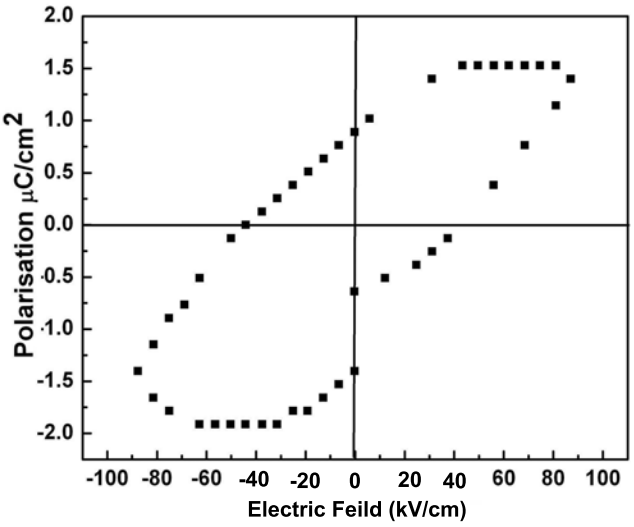

Figure 5.27: P-E hysteresis loop of the PtSi/BST/Au structure

The P-E curve shows that the polarisation is very low with a small coercive field. The remnant polarization of $1\mu C/cm^2$ and coercive field of 45kV/cm. The saturation polarisation is about $1.8\mu C/cm^2$. The low value of the PtSi/BST/Au devices can be attributed to the smaller grain size (12nm) of thin films on PtSi substrates.

PtSi/LSCO/BST/LSCO/Au

The ferroelectric property of the BST thin films on oxide films in the configuration PtSi/LSCO/BST/LSCO/Au is studied. The P-E characteristics (figure 5.28) of the films shows hysteresis behavior with a remnant polarization of $4.8\mu C/cm^2$ and coercive field of 48kV/cm. The saturation

polarisation is about 7.8μC/cm^2.

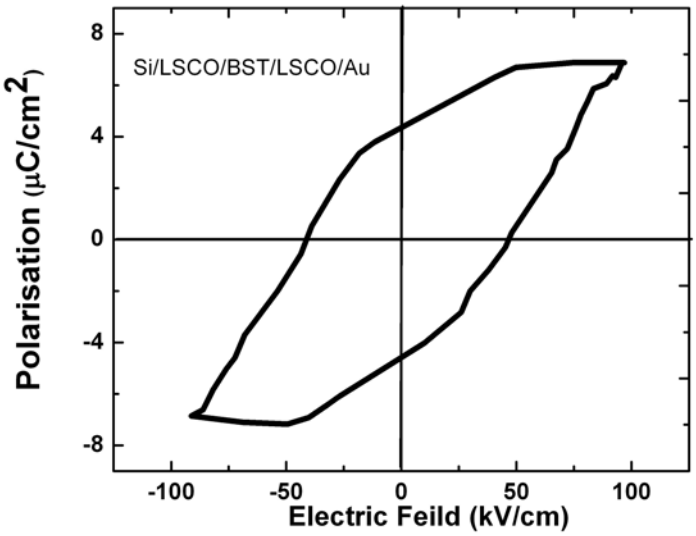

Figure 5.28: P-E hysteresis loop of the PtSi/LSCO/BST/LSCO/Au structure

The ferroelectric properties of PtSi/LSCNO/BST/LSCNO/Au is also studied using RT ferroelectric tester. The hystersis behaviour of the device is shown in figure 5.29. The remnant polarization of 8μC/cm^2 and coercive field of 35kV/cm is obtained for films deposited on LSCNO. The saturation polarisation is about 10μC/cm^2.

The improved remnant polarization on LSCNO electrode can be attributed to the crystalline growth of BST thin films. The grain size of BST thin films on LSCNO electrode is 42nm where as that on LSCO is 35nm. Hence the lower polarization of PtSi/LSCO/BST/LSCO/Au capacitors.

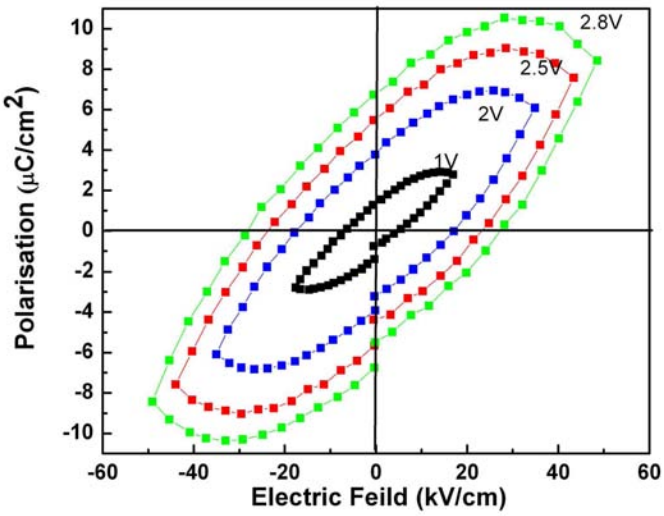

Figure 5.29: P-E hysteresis loop of the PtSi/LSCNO/BST/LSCNO/Au structure

The grain size of BST films on oxide electrode is larger than PtSi/BST/Au structure. Hence both the oxide devices showed better ferroelectric property than PtSi/BST/Au devices.

5.7 Conclusion

Ferroelectric BST thin films were grown on different substrates by pulsed laser ablation. The films were deposited using both the third harmonics and fourth harmonics of Nd:YAG laser.The films deposited by laser ablation using 266nm were found to show better properties than those grown by ablating with 355nm. The films were deposited on Si and PtSi substrates to form capacitors with Au electrodes. The electrical characterization of

the device PtSi/BST/Au is studied and the conduction mechanism shows SCLC nature at intermediate fields. The polarization versus electric field plot shows ferroelectric nature. BST thin films deposited on LSCO and LSCNO, oxide perovskite electrodes, were found to be crystalline without any post deposition heat treatment. Thus LSCO and LSCNO serve as a template as well as bottom electrode for the BST thin film capacitors. The interface between the oxide electrode and the BST layer is sharp and free from defects. The dielectric constant of BST is studied as a function of frequency. The devices showed little dispersion with frequency. The loss was found to be minimum for BST capacitors with oxide electrodes. The leakage current shows that the BST films are insulating. The films showed Pool Frenkel emission at high fields. The P-E characteristics traces hysteresis loop with a good polarization and low coercive field.

Chapter 6

Pulsed laser deposition of Eu^{3+} doped $Ba_{0.7}Sr_{0.3}TiO_3$ thin film for optoelectronic application

The europium doped barium strontium titanate (BST:Eu) films find application in ferroelectric as well as in optoelectronic devices. In this chapter the linear and nonlinear optical properties of pulsed laser deposited BST:Eu thin films are discussed. The structural and optical properties of the PLD grown BST film have been investigated and correlated. The luminescent properties of BST:Eu thin films follows a close correlation with crystallinity of thin films. Films deposited at lower substrate temperature show good luminescent characteristics. Dependance of substrate temperature on linear and nonlinear optical properties are investigated. Nonlinear properties are investigated using the Z-scan technique at room temperature.

6.1 Introduction

Perovskite oxides are attractive as a host material for rare earth doping. These materials finds application in integrated light emitting devices, field emission devices (FED's) all solid –compact laser devices operating in the blue-green region and positive temperature coefficient (PTC) resistors [168–170]. Luminescent rare earth doped materials are extensively studied because of their potential application in photonic devices and next generation flat panel displays. Rare earth (RE) ions exhibit a characteristic intra 4f shell luminescence which is almost insensitive to host material and temperature. This feature can be used to tune the emission spectrum for specific application by the appropriate doping of rare earth ions in host material [171].

Recently, electro-optic (EO) characterizations of BST films reveal an EO coefficient with a very large saturation value of the field-induced birefringence at the wavelength of 632.8 nm [172]. Optical second-harmonic generation (SHG) has also been observed in the NIR (near infra-red) wavelength range using Q-switched Nd-YAG laser at 1.06 μm [173] and mode-locked Ti:Sapphire laser at 760 nm [174]. Thin films of BST show nonlinear optical absorption and refraction and hence is a good candidate for nonlinear application. The nonlinear optical absorption and refraction of the polycrystalline $Ba_{0.7}Sr_{0.3}TiO_3$ film on quartz substrate have been measured to be 1.2x10^{-6} m/W and 1.08x10^{-15} m^2/V^2 respectively [175]. But the nonlinear absorption and refraction coefficient on epitaxial $Ba_{0.6}Sr_{0.4}TiO_3$ thin films on MgO is much lower [176]. The large value of nonlinear optical absorption and refraction of BST polycrystalline film was attributed to the small grain size and good homogeneity [175].

ABO_3 type of perovskite compounds such as $BaTiO_3$, $SrTiO_3$ and solid solutions of these viz. $Ba_xSr_{(1-x)}TiO_3$ (BST) have drawn a good deal of attention due to their attractive ferroelectric and electro optic properties. Barium strontium titanate is a dielectric material with excellent dielectric properties such as high dielectric constant, small loss and with large breakdown strength. Hence it is a good candidate as a host material for doping RE as luminescent center. BST:Eu ceramics had shown excellent luminescent properties at room temperature for application in optoelectronic devices [170]. Hence combining the merits of electrical and optical properties, BST:Eu thin films is a promising candidate for optoelectronic –ferroelectric – nonlinear optical devices.

In this chapter the linear and nonlinear optical properties of pulsed laser deposited BST:Eu thin films are presented. The structural and optical properties of PLD grown films are investigated and correlated. Dependance of substrate temperature on linear optical properties like bandgap and PL spectra are investigated. A single beam Z-scan set up is used for nonlinear absorption and nonlinear refraction measurements at room temperature.

6.2 Experimental

The target for pulsed laser deposition (PLD) was prepared by solid-state reaction of barium titanate ($BaTiO_3$), strontium titanate ($SrTiO_3$) and europium oxide (Eu_2O_3). The mixture was sintered at a temperature 1450^0C in air for 5 hrs to obtain $Ba_{0.7}Sr_{0.3}TiO_3$:Eu (BST:Eu) target with Eu 3.5 wt%. The fourth harmonics of Q-switched Nd: YAG laser(266nm) was used for ablation. The repetition frequency was 10Hz with a pulse width of

6-7 ns. The laser fluence was kept at $2J/cm^2$. The target to substrate distance was kept at 3.5cm. The substrate temperature (T_s) was varied from 300^oC to 600^0C. The oxygen partial pressure in the chamber was maintained at 0.1mbar. All the as deposited films were amorphous irrespective of the substrate temperature ($T_s = 300^0$-600^0C). The deposited films were annealed in oxygen ambience at 600^0C for 1 hr which resulted in perovskite phase. All the studies were performed on the films after the post deposition annealing at 600^0C for 1 hr in oxygen atmosphere.

The crystallinity of thin films was determined by x ray diffraction (XRD) using CuK_α radiation (λ =1.5418A^0). Thickness of the samples were measured using Dektak 6M surface profiler. The room temperature photoluminescence (PL) studies were carried out using fluorimeter (Horiba Jobin Yuon Floromax-3) in the range 500-800nm with excitation wavelength 408nm. The optical transmittance spectra of the samples were recorded in the range 190nm – 1800nm using (Jasco V - 570) UV-Vis-NIR spectrophotometer. A single beam Z-scan technique was employed for nonlinear absorption and nonlinear refraction measurements at room temperature. The second harmonics of Q switched Nd:YAG laser at 532 nm having a repetition rate of 10 Hz was used as the light source of z scan measurements. The focal length of the lens used was 25cm. Using a translation stage the sample was moved in a spatially varying intensity region on either side of the focused laser beam. The transmitted and reference energies can be measured using probe heads of the energy ratio-meter. The entire setup was automated using LabVIEW. The details of the experimental set up is described in chapter 2.

6.3 Results and discussion

6.3.1 Structural and Compositional analysis

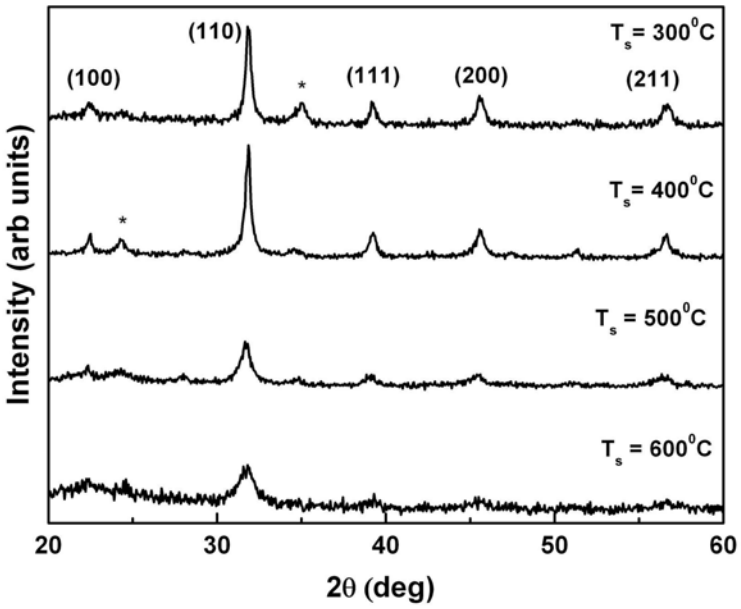

Figure 6.1: The XRD pattern of BST:Eu thin films deposited at various substrate temperature and then annealed in oxygen atmosphere at 600^0C (* represents $SrTiO_3$)

X-ray diffraction patterns of the europium doped barium strontium titanate(BST:Eu) thin films deposited on quartz substrates at various substrate temperature (T_s) and then annealed at 600^0C in oxygen atmosphere are shown in figure 6.1. The crystallinity of thin films annealed in oxygen atmosphere at 600^0C decreases with increase in T_s during the deposition.

The films were crystalline with tetragonal perovskite structure having (110) orientation on annealing.

The amorphous films deposited at lower T_s on post deposition annealing at 600^0C in oxygen ambiance may reorient and recrystallise to form oxygen rich perovskite phase as evident from the XRD pattern. The (100) peak is ascribed to the fact (100) plane is a closely packed oxygen plane which has the lowest surface energy in perovskite structure [134]. The XRD peak observed at 24^0 for thin film deposited at 400^0C and the peak at 34^0 for films deposited at 500^0C may be attributed to the presence of $SrTiO_3$ in thin films. The films deposited at high temperature did not show oxygen rich (100) orientation after post deposition annealing. Thin films deposited below 300^0C substrate temperature were amorphous even after post deposition annealing in oxygen ambience.

The surface morphology of BST:Eu films were studied using scanning electron microscope (SEM). The SEM pictures (figure 6.2) shows that the post deposition annealed films are smooth irrespective of the deposition temperature.

EDX was used to determine the atomic percentage of Ba, Sr and Ti. The atomic ratio of (Ba+Sr)/Ti for stoichiometric BST is 1. The variation of this ratio with substrate temperature is shown in figure 6.2c. The (Ba+Sr)/Ti ratio for films grown at 300^0C is close to unity (1.06) which indicates that the films grown at this condition are stoichiometric. Hence the better crystallinity at $T_s = 300^0$C is due to the recrystallisation. The films deposited at 600^0C are not stoichiometric (Ba+Sr)/Ti = 1.6) as evident from the EDX and hence poorly crystalline.

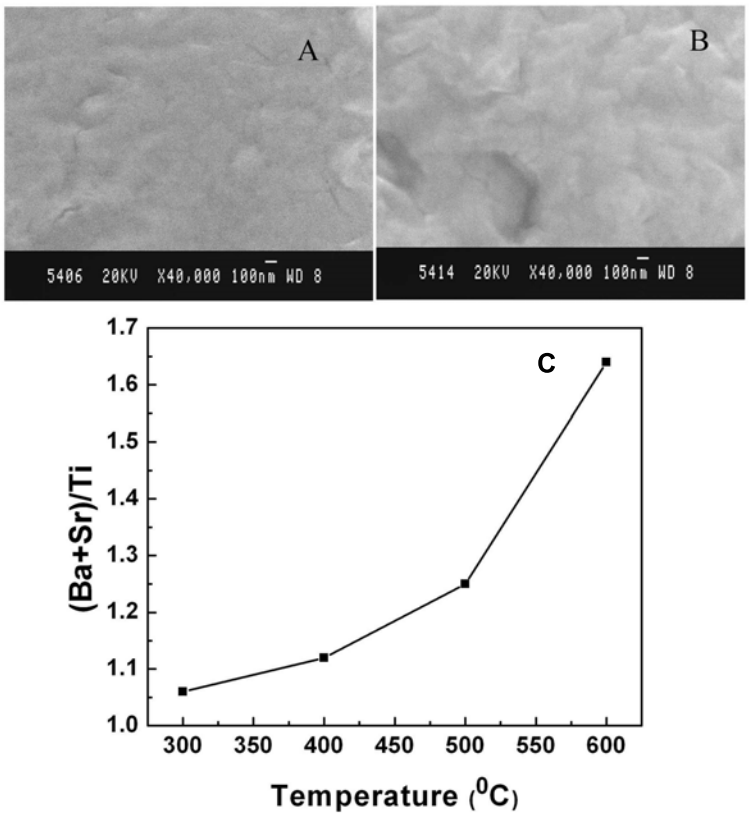

Figure 6.2: A typical SEM image of BST:Eu thin film deposited by PLD and post annealed in oxygen atmosphere at 600^0C (A) $T_s = 300^0$C and (B)$T_s = 600^0$C (C) the variation of (Ba+Sr)/Ti with substrate temperature T_s.

6.3.2 Photoluminescence (PL) studies

The PL spectra (figure 6.3) of the thin films were recorded at an excitation wavelength of 408 nm. The emission band clearly shows the presence of Eu^{3+} in the host lattice. The Commission Internationale de lEclairage (CIE) coordinates of the films were calculated from the emission spectra.

The BST:Eu films gives a red emission with CIE coordinates (x=0.615; y=0.383) suggesting the use of BST:Eu in phosphor convertor light emitting diodes converting UV and blue emission to red emission.

The emissions in the region 550-700nm are in good agreement with radiative transition between energy levels of Eu^{3+} ions [177, 178]. The PL emission peak in this region are due to the transition $^5D_0$ – ^7F_j (j = 2,3). The PL peak at 615nm and 669nm are respectively the characteristic $^5D_0$ – $^7F_2$ and $^5D_0$ – $^7F_3$transitions of Eu^{3+} ions [179, 180]. The emission at 550nm is due to the transition $^5D_1$ – $^7F_1$ [179]. The most prominent Eu^{3+} related emission is in the red spectral region due to the $^5D_0$ – $^7F_2$ transition. The presence of $SrTiO_3$ has not effected the PL spectra of BST:Eu thin films since $SrTiO_3$ itself is good host material for Eu^{3+} ions showing similar PL transitions [180].

PL spectra of amorphous thin film BST is also shown in figure 6.3. Luminescence of amorphous and partially crystalline materials originate from disordered phase [181, 182]. The observed PL in amorphous film show a broad emission peak at 617.5nm. This emission is not due to Eu^{3+} ions since the other transitions at 550nm and 699nm were absent. Hence the emission of as deposited BST:Eu thin films can be attributed to the disordered phase of the host BST material.

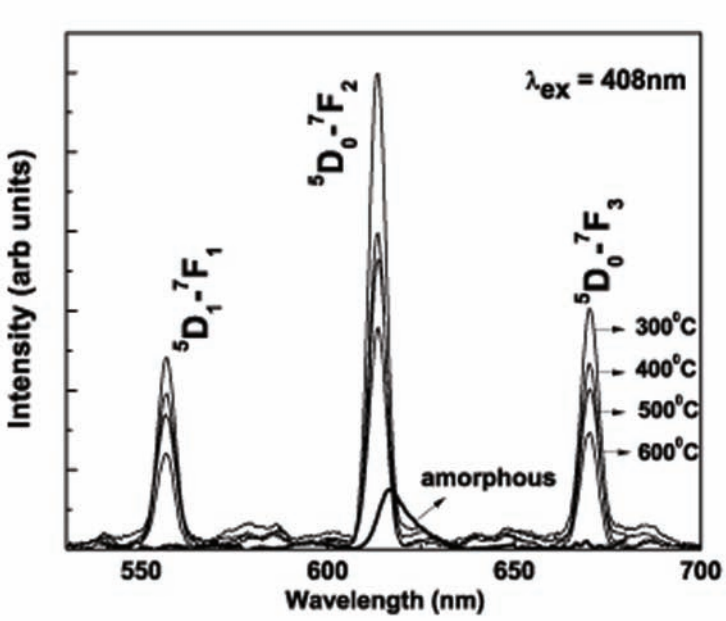

Figure 6.3: Room temperature photoluminescence emission (λ_{ex} = 408nm) spectra of BST:Eu thin film deposited at different substrate temperatures and post annealed at 600^0C. PL emission of as deposited amorphous film is also shown.

The as deposited films at $T_s \geq 300^0$C on annealing in O_2 atmosphere at 600^0C , reorient and recrystallise to form crystalline BST:Eu thin films. Films deposited at lower substrate temperature (300^0C) on post deposition annealing was found to be polycrystalline with larger grain size (29nm). The improvement in crystallinity can be related to oxygen stoichiometry as indicated by the x ray diffraction peak. The (100) plane is the closely packed oxygen plane which has the lowest surface energy in perovskite structure [134]. The EDX analysis shows that the cationic ratio is ~ 1 for the film deposited at $T_s = 300^0$C. Hence the higher PL intensity for the films grown at 300^0C can be attributed to the better crystallinity and lower

oxygen defect density. Lower defect density and better grain size correspond to a better PL transition[183]. As T_s increases the oxygen defect density and cationic ratio Ba+Sr/Ti increases providing nonradiative path for de-excitation.

Samantary et al [170] had observed splitting of the energy levels due to the crystal field in the PL spectra of BST:Eu powder. But no such splitting was observed in BST:Eu thin films in the present study . This indicates that there is no change in crystal field symmetry. The weak emission at 580nm corresponding to the forbidden $^5D_0$ - $^7F_0$ electric dipole transition suggests that Eu^{3+} ions occupy the low symmetry environment in BST. The ionic radii of Eu ion is more close to Ba^{2+} ions than Ti^{4+} sites and hence Eu^{3+} ions occupy Ba^{2+} ions preferentially. In perovskite crystal structure of $BaTiO_3$ the distance between Ti^{4+} and O^{2-} is $2.00\mathring{A}$ and the distance between Ba^{2+} and O^{2-} is $2.83\mathring{A}$. The crystal field is lower for Eu^{3+} ions occupying a lower symmetry site and hence no splitting of the spectral lines is observed in the PL spectrum.

The variation of PL integral intensity of the peak at 615nm and FWHM of the XRD peak with substrate temperature at which the films are grown is shown in figure 6.4.

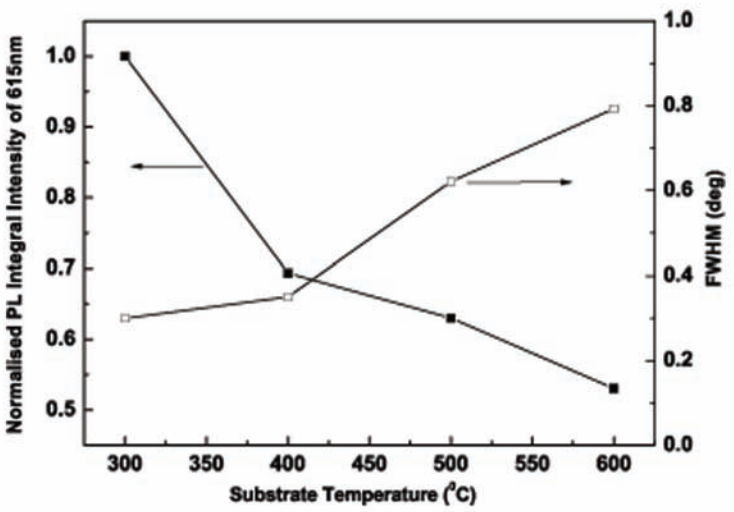

Figure 6.4: The variation of normalised integral intensity of PL emission of BST:Eu thin film excited at 408nm.

Characteristic luminescence features of the materials are determined by the electronic structure of the doped rare earth, while the width and the relative intensity of the spectra depend on the crystal symmetry of the host matrix [170].The characteristic emission of Eu^{3+} is present in all the films grown at $T_s \geq 300^0$C irrespective of the processing condition. The Eu content in the film may vary with substrate temperature. The EDX spectra shows all the films have the Eu content more or less the same. The PL emission peaks are intense for films deposited at $T_s = 300^0$C. This can be attributed to the better crystallinity of the films grown at that condition.

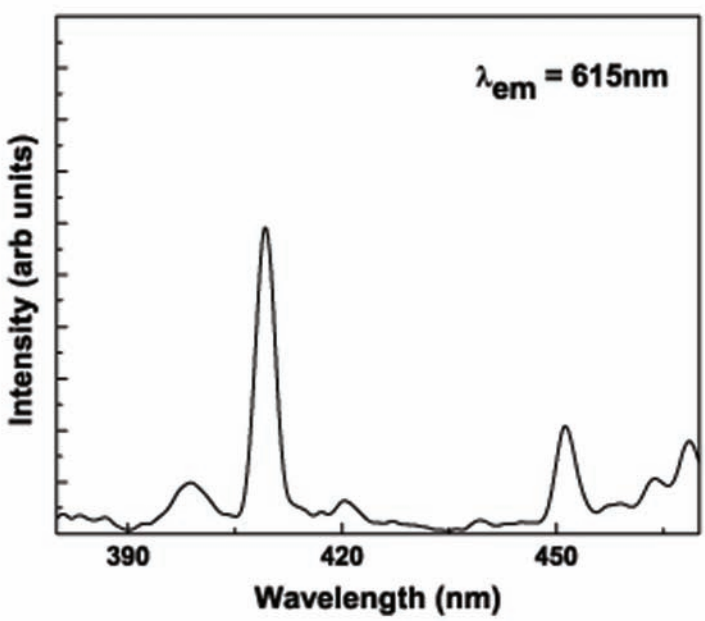

Figure 6.5: Room temperature photoluminescent excitation spectra (λ_{em} = 615nm) of BST :Eu thin films deposited at 300^0C and post annealed at 600^0C

The photoluminescent excitation (PLE) spectra of thin films are shown in figure 6.5. The excitation peaks at 408nm and 458 nm corresponds to the $^7F_0$ - $^5D_3$ and $^7F_0$ - $^5D_2$ transitions of Eu^{3+} ions corresponding to the energies 2.99eV and 2.66eV. The broad band at 398nm corresponds to the $^7F_0$ - $^5L_6$ transition (3.147eV) [180]. The emission wavelengths of BST:Eu thin films were same for all these of the excitation wavelengths.

Schematic representations of the main energy levels identified in the studied samples are shown in figure 6.6. The absorption and emission lines are shown in the diagram.

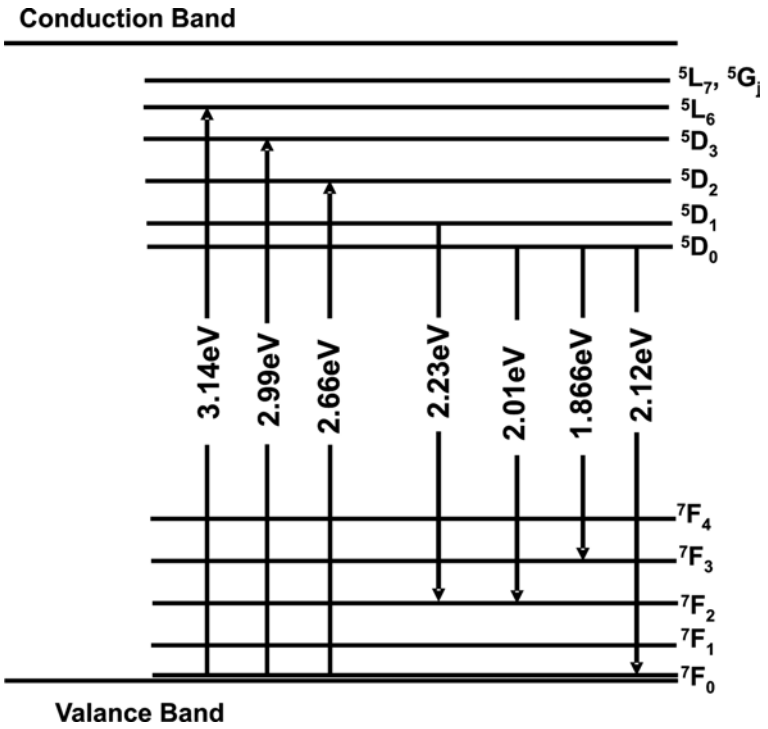

Figure 6.6: The schematic energy diagram of Eu^{3+} in BST thin film samples.

6.3.3 Optical bandgap

The optical properties of the thin films deposited on quartz substrates were investigated by recording the transmission spectra. All the films are transparent in the visible region. The optical band gap of BST thin films were found out using the Tacu's plot [137] $(\alpha h\nu)^n = A(h\nu - Eg)$ Where A is a constant,α is the absorption coefficient; h$\nu$is the photon energy , Eg optical band gap and the constant n depends on the nature of electronic transition, for direct transition n=2. BST thin films have direct allowed transitions between valance and conduction band. The transmission spectra showed a

blue shift in bandgap with substrate temperature. The plot of transmission as a function of wavelength is shown in figure6.7. Inset shows the plot of $(\alpha h\nu)^2$ vs hν of the films grown at different substrate temperatures.

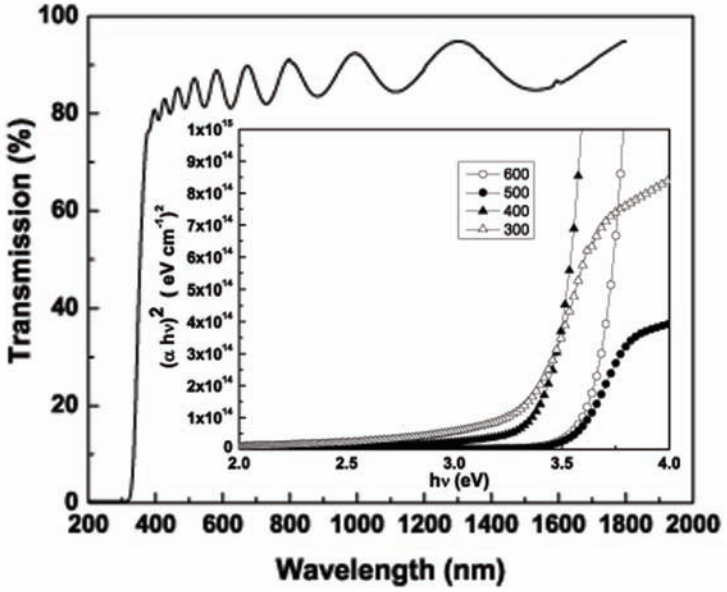

Figure 6.7: Transmission spectrum of BST:Eu thin film. Inset shows the $(\alpha h\nu)^2$ plot for various temperatures

Variation of band gap with substrate temperature is shown in figure6.8. Generally the blue shift in band gap is attributed to various reasons like the amorphous nature of the films [84], stress induced distortion by substrate film interaction [184, 185] and grain size effect [183].

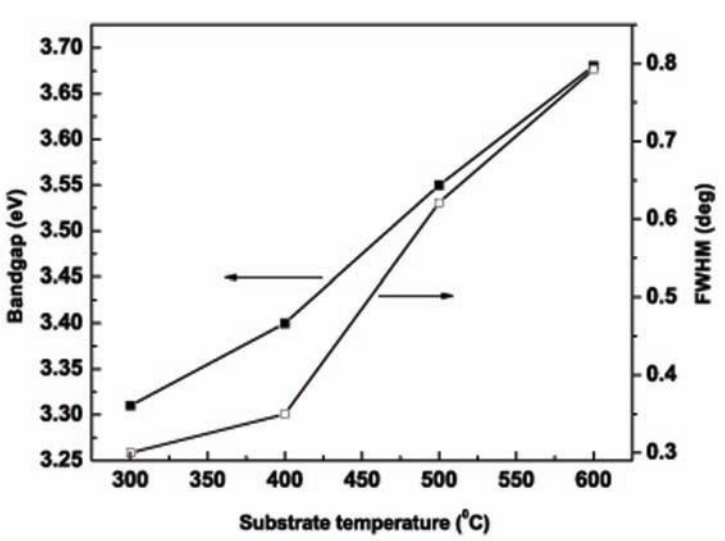

Figure 6.8: The variation of FWHM of (110) XRD peak and bandgap with substrate temperature.

The variation due to stress induced shifts is verified by depositing films under same conditions but for two different thicknesses. In the present study the films of thickness 500nm and 1μm were grown at 600^0C and then annealed in oxygen atmosphere for 1 hr at 600^0C. The band gap was found to be almost a constant (3.68 and 3.64 respectively). In the present study the variation in band gap with substrate temperature is not due to the stress effect but can be attributed to the poor crystallinity. The linear refractive index and the absorption coefficient of the thin films are calculated from the transmittance spectrum using the envelope methods[80]. At 532nm the linear refractive index is found to be 1.82.

6.3.4 Nonlinear optical studies

Nonlinear absorption coefficient is calculated from the single beam Z scan set up as described in section 2.3.5. The open aperture curve comprises a normalised transmittance as a result of non linear absorption as shown in figure 6.9.

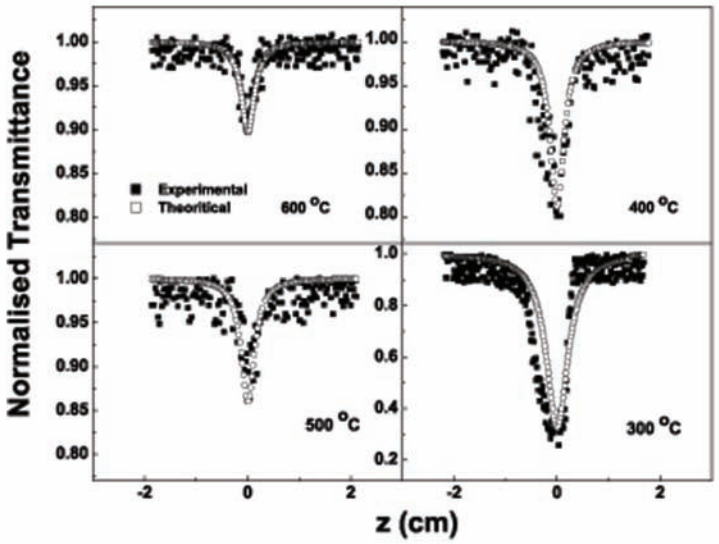

Figure 6.9: The open aperture Z-scan curve of BST:Eu thin films grown at different substrate temperature.

The experimental data is fitted with the theoretical values (open circles). The theoretical equation for normalised transmittance T, for two photon absorption is given by equation 6.1 [84].

$$T(z, S = 1) = (1/\sqrt{\pi})q_0(Z, 0) \int [ln(1 + q_0(Z, 0))e^{-\tau^2}]d\tau \qquad (6.1)$$

Where q_0(Z,t) is the fitting parameter given by equation 6.2, S=1 for open aperture

$$q_0(Z,t) = \frac{\beta I_0(t) L_{eff}}{(1 + z^2/z_0^2)} \tag{6.2}$$

β is the nonlinear absorption coefficient, I_0(t) is the on axis irradiance at the focus L_{eff} is the effective focal length given by equation 6.3

$$L_{eff} = \frac{(1 - e^{-L\alpha})}{\alpha} \tag{6.3}$$

with L the sample length and α the linear absorption coefficient. The experimental curve can be theoretically fitted by equation 6.1 and the non-linear absorption coefficient β is calculated. Since quartz substrates have very low nonlinear absorption at 532 nm the observed non linear absorption is from BST:Eu thin films.

The open aperture Z-scan curve of BST:Eu shows that the dip in the nonlinear absorption is maximum for thin films deposited at 300^0C followed by the post annealing. This is attributed to the better crystallinity of thin films grown at 300^0C. In the present study the nonlinear absorption coefficientβ was found to increase with decrease in T_s (figure 6.10).

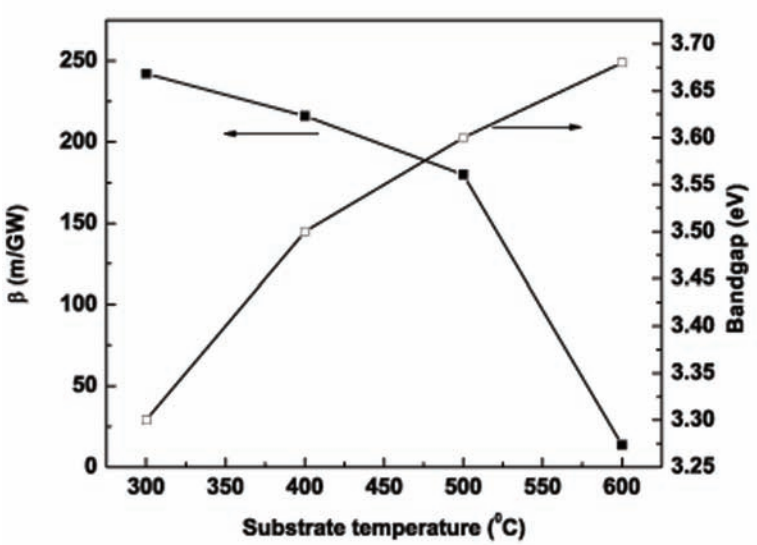

Figure 6.10: The variation of absorption coefficient β and bandgap of BST:Eu thin films with substrate temperature.

Absorption coefficient β follows an inverse relation with bandgap E_g [186]. The figure 6.10 clearly depicts the inverse relation of absorption coefficient and bandgap. This variation is followed from the crystallinity of thin films with T_s.

The imaginary part of third order nonlinear susceptibility $Im\chi^{(3)}$ is calculated using the relation between $Im\chi^{(3)}$ and β given by equation 6.4 [84].

$$\beta = \frac{3kIm\chi^3}{2\epsilon_0 c n_0} \tag{6.4}$$

Where $k = 2\pi/\lambda$ ($\lambda = 532$nm) ϵ_0 is free space dielectric constant, n_0 is linear refractive index and c the velocity of light. The third order suscep-

tibility of all BST:Eu thin films were calculated. The variation of Im$\chi^{(3)}$ with substrate temperature is shown in figure 6.11

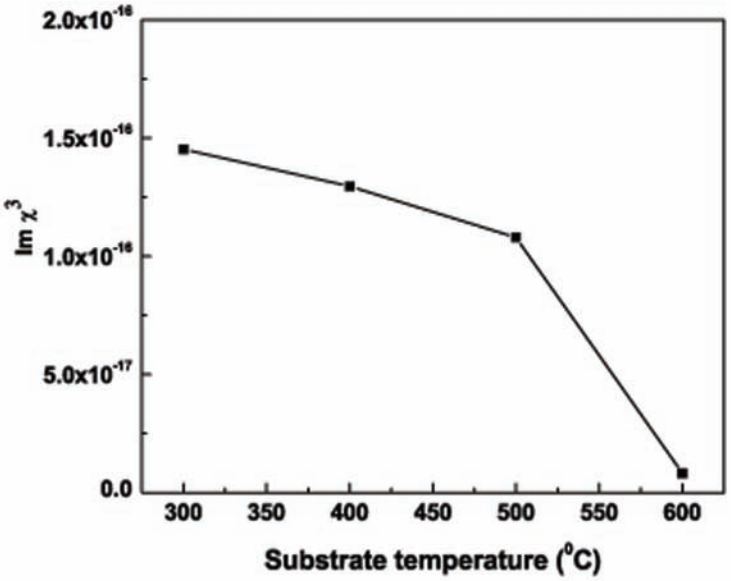

Figure 6.11: The variation of Im$\chi^{(3)}$ of BST:Eu thin films with substrate temperature.

The typical closed aperture Z-scan curve for the BST:Eu film is shown in figure 6.12. The measured data show a negative nonlinear refractive index n_2 with peak-to-valley curve. The curve was obtained by dividing the closed aperture data with the corresponding open aperture data, after normalizing each scan.

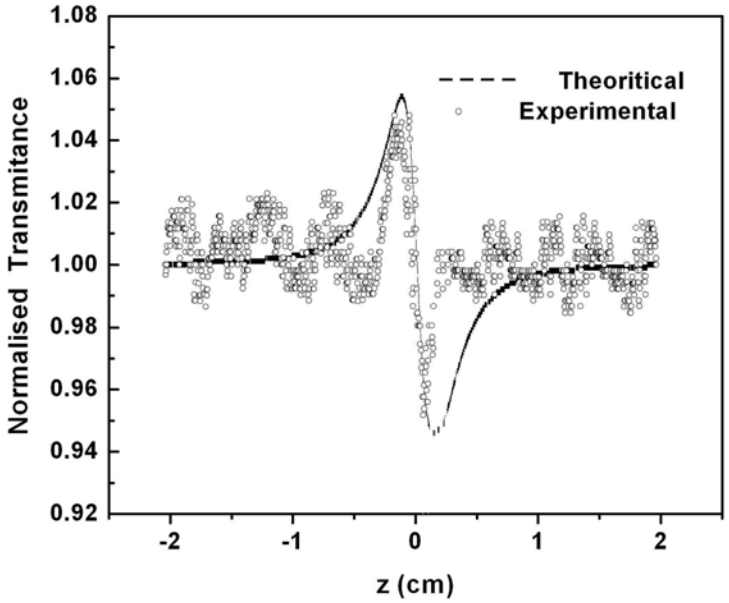

Figure 6.12: Closed aperture Z-scan curve of BST:Eu thin film (S=0.1). The dotted line is the theoretical fit.

The data were analysed using the procedure described by Sheik-Bahae [84]. The on axis phase shift at the focus, $\Delta\phi_0$, can be obtained through the best theoretical fit from the normalised closed aperture transmittance T(z,$\Delta\phi_0$) at the sample position z, by the equation (6.5) [84].

$$T(z, \Delta\phi_0) \approx [1 + \frac{4\Delta\phi_0 x}{(x^2+9)(x^2+1)}] \tag{6.5}$$

where x = z/z_0. The nonlinear refractive index γ and the real part of third order optical nonlinear susceptibility Re$\chi^{(3)}$ is given by the following equations (6.6) and (6.7) [84].

$$\gamma = \frac{\lambda\Delta\phi_0}{2L_{eff}I_0} \tag{6.6}$$

$$Re\chi^{(3)} = 2(n_0)^2\varepsilon_0 c\gamma \tag{6.7}$$

where λ = 532nm is the wavelength of laser used, ϵ_0 is free space dielectric constant, n_0 is linear refractive index and c the velocity of light. The calculated nonlinear refractive index is - 1.508 x 10^{-6} m^2/GW and the real part of third order optical susceptibility, Re$\chi^{(3)}$ is 2.58 x 10^{-17} m^2/V^2 . The negative nonlinear refractive index indicates the self defocusing optical nonlinearity. The third order nonlinear susceptibility can be expressed as χ^3 = Re$\chi^{(3)}$ + i Im $\chi^{(3)}$

The property of two photon absorption makes BST:Eu useful for novel application as an optical limiter. An ideal optical limiter has a linear transmission only up to threshold input fluence I_{th} which will vary in different materials. If the input fluence is increased above the I_{th}, the output fluence remains a constant. So the transmittance T of the sample falls down with increasing input fluence. The optical limiting characteristic of samples is the plot of input energy versus normalized transmittance T of the sample (figure 6.13). All the films showed optical limiting behavior. The I_{th} of the thin film sample grown at 300^0C is about 125μJ.

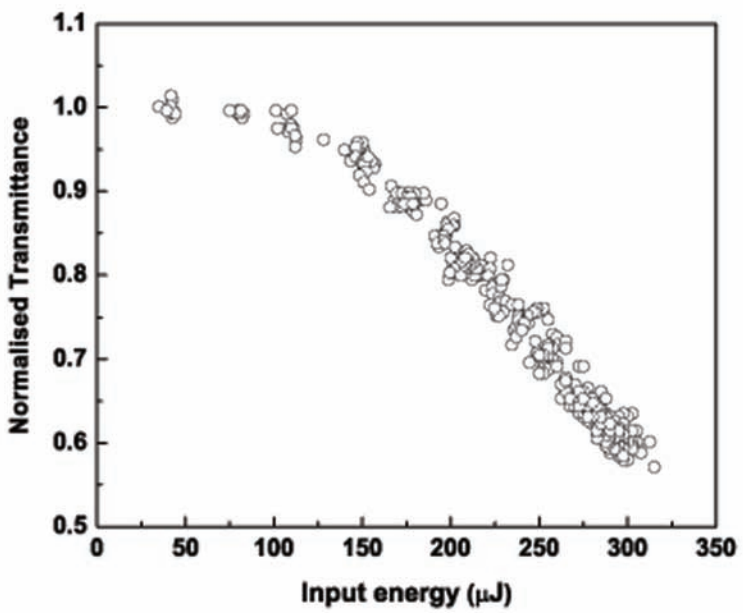

Figure 6.13: The optical limiting property of BST:Eu thin films.

6.3.5 Electrical Characterizations

The electrical characterization is carried out on BST:Eu thin films deposited on commercial PtSi wafer. Gold deposited through shadow mask by rf sputtering was used as the top electrode. The structure used for the electrical characterization is PtSi/BST:Eu/Au.

The leakage current of the samples were obtained from the current voltage characteristics.

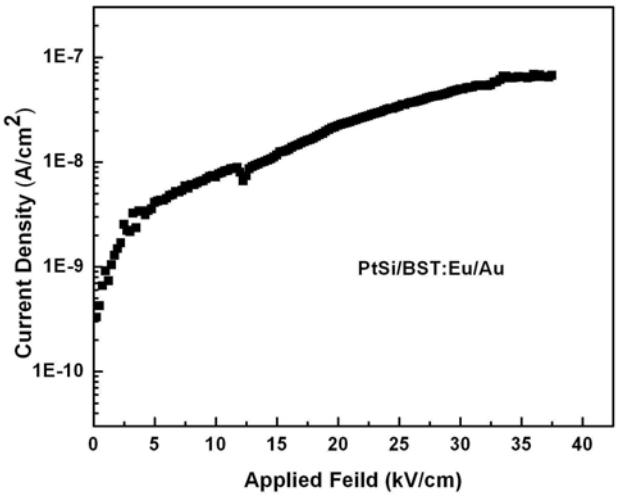

Figure 6.14: The room temperature leakage current with applied dc voltage for the device PtSi/BST:Eu/Au.

The current density versus electric field characteristics of the BST capacitor with the structure PtSi/BST:Eu/Au is shown in figure 6.14. The leakage current density of BST:Eu thin film capacitor is found to be 200nA/cm^2 at a bias voltage of 2V for 600nm thick BST:Eu film. The low leakage current density shows that the films have good insulating property.

The dielectric constant of the hetrostructure PtSi/BST:Eu/Au is calculated using the relation

$$c = \frac{A\epsilon\epsilon_r}{d} \tag{6.8}$$

Where C is the capacitance in Farads,ϵ the free space dielectric constant (8.85x10^{-12}F/m), A the area of the capacitor (m^2) and d (m) the thickness of the ferroelectric thin film. The variation of dielectric constant with frequency for PtSi/BST:Eu/Au device is shown figure 6.15.

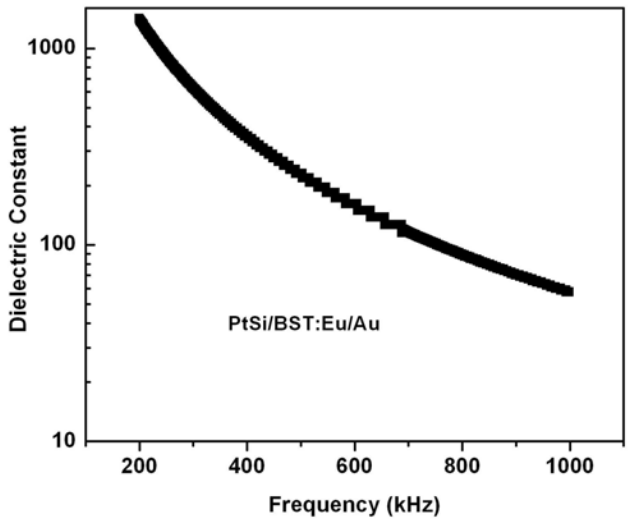

Figure 6.15: The capacitance-frequency variation of BST:Eu thin films deposited on PtSi/BST/Au devices.

The dielectric constant of the crystallized films were found to be around 1400 at a frequency of 100kHz. The dielectric constant is almost same for PtSi/BST/Au devices. Thus BST:Eu showed similar behavior as that of undoped sample.

Figure 6.16 shows the room temperature dielectric constant ϵ as a function of the applied dc electric field where the relative dielectric constant ϵ_r was calculated from the capacitance data using the formula parallel-plate capacitors. The capacitance - voltage characteristics of the BST films were measured at a frequency of 100KHz. Hysteresis was observed in the films showing the ferroelectric phase at room temperature. The dielectric properties BST:Eu thin films are highly tunable through the application of dc bias field.

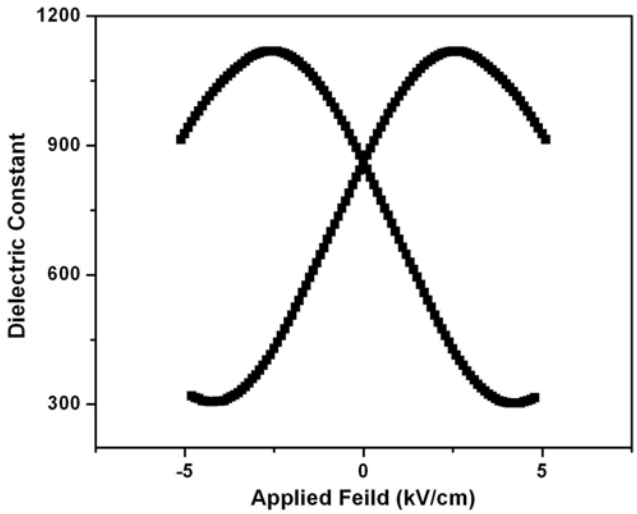

Figure 6.16: Variation of Dielectric constant of PtSi/BST:Eu/Au devices with applied field at 100kHz.

6.4 Conclusion

Eu doped BST thin films were successfully deposited by pulsed laser ablation. Optical properties follow a close correlation with the crystallinity of thin films. All the as deposited films were amorphous and post annealing in oxygen atmosphere at 600^0C results in crystalline films with perovskite structure. Luminescent properties were investigated at an excitation wavelength of 408nm. The room temperature photoluminescence spectrum reveals the characteristic lines of rare earth Eu^{3+} in all the thin films. The luminescence intensity shows a close correlation with crystallinity of thin films. The linear refractive index of the samples calculated from the transmittance spectra is 1.82. The nonlinear optical properties were investigated by a single beam Z scan set up. The films show excellent nonlinear opti-

cal property. The open aperture Z-scan curve of BST:Eu shows that the dip in the nonlinear absorption is maximum for thin films deposited at 300^0C. The imaginary part of third order susceptibility $\mathrm{Im}\chi^{(3)}$ increases with substrate temperature. The thin film shows good optical limiting property with a threshold input fluence of 125μJ. This indicated that the BST:Eu thin films can be used for optoelectronic applications. The electric property of BST:Eu thin films shows that the films are highly insulating. The dielectric constant of BST:Eu is also high. The capacitance voltage measurements shows the ferroelectric nature of BST:Eu thin films. Thus nonlinear - optoelectronic - ferroelectric functions of BST:Eu thin films can be integrated to a single device

Chapter 7

Summary and Scope for further study

7.1 Summary of present study

Todays dynamic random access memories (DRAMs) have advanced by mainly focussing on how to make memory cells small to realize high density DRAMs. The continuous shrinking of devices up to Gbit density exposes many technological challenges. The most critical challenges in gigabit density DRAMs are yield loss due to large die size and small feature size, standby current failure caused by large chip size and small data retention times owing to reduced charge packet in the memory cell. Narrowing the bandwidth mismatch between fast processors and slower memories and achieving low-power consumption together with aforementioned challenges drive DRAM technologies toward smaller cell size, faster memory cell operation, less power consumption and longer data retention time. In addition, a tight control of increasingly complicated wafer processing requires DRAM

process technology to be simpler and less sensitive to processing variation. Thus, DRAM technology in Gbit era should solve the challenges imposed by the shrink technology system application requirement and manufacturing technology [29, 187–189].

One of the most critical challenges which Gbit density DRAMs face will be memory cell capacitance. Memory cell capacitance is the crucial parameter which determine the sensing signal voltage, sensing speed, data retention times and endurance against the soft error event. It is generally accepted that the minimum cell capacitance is more than 25fF per cell regardless of density. However, lower supply voltage and increased junction leakage current due to high doping density drive memory cell capacitance toward higher value more than 25fF per cell in the Gbit density DRAMs. The strategy to increase memory cell capacitance has been focussed on the increase of the memory cell capacitor area and decrease of the dielectric thickness up to now. In the memory cell capacitor which is the most important technology in the Gbit era, high dielectric constant capacitor seems to be the only solution [29].

The capacitor materials currently utilized in DRAMs are either silicon dioxide (SiO_2) or a silicon oxide/nitride composite layer (ONO) with a relative dielectric constant of 6. Use of SiO_2 or ONO allows the memory cell to be fabricated as a metal-oxide-semiconductor (MOS) device. As the number of memory cells increase to gigabits, the available area for the capacitor decreases rapidly ($0.4mm^2$ for a 256-Mbit device and 0.2 mm^2 for a 1-Gbit device) to maintain acceptable die sizes. For maintaining sufficient storage capacitance of memory cell, manufacturers have abandoned the idea of flat integrated circuits and three-dimensional cell structures were consequently incorporated by use of deep trenches and stacked layer to offer more surface

area. So far, these structures with ONO storage dielectrics can adhere to the requirements of 256-Mbit DRAMs. The capacitor areas will be close to 0.2mm^2 and 0.1mm^2 for future 1-Gbit and 4-Gbit DRAMs, respectively, and there is a requirement that the capacitance per unit area be increased. The ONO dielectrics will not be used in these products since the capacitor area cannot be maintained constant in a cell that is still manufacturable and also the ONO dielectric thickness has reached a lower limit set by electron tunneling through the dielectric [28]. Consequently, an increasing effort has been made in search of alternative dielectric having a substantially higher permittivity. The first step in the direction of high dielectric constant materials is to consider some single metal oxide materials such as Ta_2O_5, TiO_2 , or others. The dielectric constant and critical capacitance (defined as the maximum capacitance-per-unit area that can be achieved for a film that satisfies DRAM leakage requirements) [190] for various single metal oxides that present dielectric constant values is in the range 10 – 100. On the other hand, ferroelectric materials are considered the ideal DRAM dielectrics for the Gbit era since they exhibit dielectric constants in the range 200 – 2000 range [29].

In the recent years thin film perovskite materials with high dielectric constant such as PZT, $SrTiO_3$ and (Ba,Sr)TiO_3 (BST) [30, 191–196] have been investigated as materials for future memory. The best suited dielectric material would have a low leakage current and a high dielectric constant. $SrTiO_3$ has a smaller dielectric constant than BST and PZT is in ferroelectric phase at room temperature. Hence these materials were used in the present study for possible ferroelectric memory device. Thin films of PZT and BST were deposited using PLD. BST thin films were also deposited by rf magnetron sputtering. From the study it can be seen that the films

deposited using PLD were crystalline with (100) perovskite phase. The grain size of ablated thin films were larger than that of sputtered BST films. Hence the ferroelectric properties depends on the growth temperature. Hence PLD can be considered to be the best method to deposit high quality ferroelectric thin films with high dielectric constant and low loss.

PZT thin films were successfully deposited at low temperature by PLD with ZnO buffer layer. This finds application in MEMS devices which demands a low temperature deposition of PZT for integrating with existing Si technology. A lead free ferroelectric material, BST has been successfully deposited for DRAM applications. Capacitors are fabricated and electrical properties were investigated. The oxide electrode layer favors better growth and properties for the BST thin film. The fabricated capacitors PtSi/LSCO/BST/LSCO can be used in gigabyte memory. BST thin films were deposited by rf magnetron sputtering. Rf magnetron sputtered BST showed a structure related optical and electrical properties with respect to oxygen mixing ratio (OMR). But the lower grain size of the films had caused a reduction in ferroelectric property. The rare earth doped BST thin films gives a red emission suggesting the use of BST:Eu in phosphor converter light emitting diodes converting UV and blue emission to red emission.The BST:Eu films can be used for both ferroelectric as well as for optoelectronic application.

7.2 Scope for further study

The FeRAM can be fabricated with the ferroelectric materials and films developed in the present study. After satisfying the requirements for capacitance and leakage current, another relevant issue is the reliability, in

the practical use of the BST films for memory cell capacitors. As commonly observed, leakage current gradually increases with a degradation of the insulation when applying temperature, ac and dc voltage stresses to BST capacitors for a certain time duration. The degradation process limits the lifetime and reliability of BST capacitors. Further understanding the defect formations and distribution, relaxation, conduction and breakdown of BST capacitors is required to improve the reliability.

The advancement of thin film technology and the principles of miniaturization/integration, BST thin films will remain as fertile field of research and development, full of application potential and rich in science.

Appendix A

Abbreviations used in the thesis

Table A.1: Abbreviations used in the thesis

Abbreviation	**Expansion**
AFE	Antiferroelectric Phase
AFM	Atomic Force Microscope
BCC	Body centered Cubic
BBSRAM	Battery Backed Static RAM
BST	Barium Strontium Titanate
CIE	Commission Internationale de lEclairage
C-V	Capacitance-Voltage
CVD	Chemical Vapour Deposition
CRT	Cathode Ray Tube
DC	Direct Current
DRO	Destructive Read Out
DRS	Diffuse Reflectance Spectroscopy
DUT	Device Under Test
DRAM	Dynamic Random Access Memory
EDAX	Energy Dispersive X-ray Spectroscopy

Abbreviation	**Expansion**
FCC	Face Centered Cubic
FE	Ferroelectric Phase
FED	Field Emission Devices
FeTFT	Ferroelectric Thin Film Transistor
FeRAM	Ferroelectric RAM
FWHM	Full Width at Half Maximum
Gbit	Gigabit
IC	Integrated Circuit
IDT	Interdigital Transducers
I-V	Current - Voltage
LVDT	Linear Variable Differential Transformer
MEMS	Micro Electro Mechanical Systems
MLC	Multilayer Ceramic Capacitors
MMIC	Microwave Monolithic Integrated Circuits
MOS	Metal Oxide Semiconductor
MOSFET	Metal Oxide Semiconductor Filed Effect Transistor
MOCVD	Metal Organic Chemical Vapour Deposition
MPB	Morphotropic Phase Boundary
Nd:YAG	Neodymium Yttrium Aluminium Garnet
NDRO	Non Destructive Read Out
NVRAM	Nonvolatile Random Access Memory
OMR	Oxygen Mixing Ratio
P-E	Polarization - Electric Field
PECVD	Plasma Enhanced Chemical Vapour Deposition
PL	Photoluminescence
PLE	Photoluminescence Excitation
PLD	Pulsed Laser Deposition
PVD	Physical Vapor Deposition
PT	Lead Titanate
PLZT	Lead Lanthanum Zirconium Titanate
PTC	Positive Temperature Coefficient
PtSi	$Pt/TiO_2/SiO_2/Si$
PZT	Lead Zirconium Titanate
P2ZT	Lead Zirconium Titanate 2% Pb excess

Abbreviation	**Expansion**
P10ZT	Lead Zirconium Titanate 10% Pb excess
RAM	Random Access Memory
RE	Rare Earth
RF	Radio Frequency
rpm	Rotations Per Minute
RT	Room Temperature
RTA	Rapid Thermal Annealing
SAW	Surface Acoustic Wave
SEM	Scanning Electron Microscopic
SCLC	Space Charge Limited Current
SPM	Scanning Probe Microscopy
UV	Ultraviolet
ULSI	Ultra Large Scale Integrated Circuits
VDD	Virtual Device Driver
XPS	X-ray Photoelectron Spectroscopy
XRD	X-ray Diffraction
XRF	X-ray Fluorescence Spectroscopy

Bibliography

[1] M.E. Lines and A.M.Glass. *Princilples and applications of ferroelectricsand related Materials*. Oxford University Press,New York, 1977.

[2] D.B.Chrisey and G.K.Hubler. *Pulsed laser deposition of thin films*. John Wiley and Sons, New York, 1994.

[3] J.G.Bednorz and K.A.Mueller. *Z.Phys*, B64:189, 1986.

[4] S.B.Krupanidhi, M.Sayer, K. El Assal, C.K.Jen, and G.W.Farnell. *J.can.Ceramic Soc.*, 54:28, 1984.

[5] M.Okuyama and Y.Hamakawa. *Ferroelectrics*, 63:243, 1985.

[6] H.Adachi, T.Mitsuyo, O.Yamazaki, and K.Wasa. *J.Appl Phys*, 60:736, 1986.

[7] S.Y.Wu. *Ferroelectrics*, 11:379, 1976.

[8] A.Iclinose, Y.Hirao, N.Nakamoto, and T.Tamshita. *Jpn. J.Appl Phys*, 23:462, 1985.

[9] J.F Scott. *Ferroelectric Memories*. Springer Verlag, Heidelberg, 2000.

[10] L.H.Parker and A.F.Tasch. *IEEE circuits and device magazine*, 1:17, 1990.

[11] J.F Scott. *Ann Rev Mater Sci*, 28:79, 1999.

[12] H.T. Lue and T.Y Tseng. *IEEE Trans Ultrason Ferroelectric freq control*, 48:1402, 2001.

[13] Y. Xu. *Ferroelectric Materials and their Applications*. North Holland, Amsterdam, 1991.

[14] R. Pepinsky, Y. Okaya, and F. Unterleitner. *Acta. Cryst*, 13:1071, 1960.

[15] B. Jaffe, W. R. Cook Jr, and H. Jaffe. *Piezoelectric Ceramics*. Academic Press, London, 1971.

[16] W. Jackson and W. Reddish. *Nature*, 156:717, 1945.

[17] D. F. Rushman and M. A. Strivens. *Trans. Faraday Soc.*, 42A:231, 1946.

[18] T. Matsui and W. B. Westphal. *Phys. Rev.*, 124:1354, 1961.

[19] H. Kneipkamp and W. Heywang. *Z. Angew. Phys*, 6:385, 1954.

[20] D. Hennings and G. Rosenstein. *J. Am. Ceram. Soc*, 67:249, 1984.

[21] A. J. Bell. *Proc. Int. Symp. Appl. Ferroelectrics*, 1994.

[22] S. L. Swartz. *IEEE Trans. Electrical Insulation*, 25:935, 1990.

[23] W. R. Buessem, L. E. Cross, and A. K. Goswami. *J. Am. Ceram. Soc*, 75:2927, 1966.

[24] G. Arlt, D. Hennings, and G. de With. *J. Appl. Phys*, 58:4, 1985.

[25] B.A Baumert, L.H Chang, A.Mastuda, T.L Tsai, C.Tracy, R Gregory, P.Fejas, and N.Caves. *J.Appl.Phys*, 82:2558, 1997.

[26] E.Ngo, P.C.Joshi, M.W.Cole, and C.W.Hubbard. *Appl. Phys. Lett*, 79:248, 2001.

[27] T.Y. Tseng. *IEDMS*, C2-5:89, 1996.

[28] A. I. Kingon, S. K. Streiffer, C. Basceri, and S. R. Summerfelt. *MRS Bull*, 21:46, 1996.

[29] S.Ezhilvalavan and T.Y. Tseng. *Mater.Chem.Phys*, 65:227, 2000.

[30] H. Kawano, K. Mori, and Y. Nakayama. *J. Appl. Phys.*, 73:5141, 1993.

[31] T. Horikawa, N. Mikami, T. Makita, J.Tanimura, M. Kataoka, K.Sato, and M. Nunoshita. *Jpn. J. Appl. Phys.*, 32:4126, 1993.

[32] T. Horikawa, T. Makita, T. Kuroiwa, and N. Mikami. *Jpn. J. Appl. Phys.*, 34:5478, 1995.

[33] R.E. Jones. *Appl. Phys. Lett.*, 60:1022, 1992.

[34] T. Kuroiwa, Y. Tsunemine, T. Horikawa, T. Makita, J. Tanimura, N. Mikami, and K. Sato. *Jpn. J. Appl. Phys.*, 33:5187, 1994.

[35] C.S. Hwang, S.O. Park, H-J. Cho, C.S. Kang, H.-K. Kang, S.I.Lee, and M.Y. Lee. *Appl. Phys. Lett.*, 67:2189, 1995.

[36] S.Saha and S.B.Krupanidhi. *Mater.Sci.Eng.,B*, 57:135, 1999.

[37] I.Suzuki, M.Ejima, K watanbe, Y.MXiong, and T.Saitoh. *Thin Solid Films*, 313:214, 1998.

[38] L. E. Cross. *Ferroelectric Ceramics-Tutorial Reviews, Theory, Processing and Applications*. Birkhauser Verlag, Basel, 1 edition, 1993.

[39] T. B. Weston, A. H. Webster, and V. M. McNamara. *J. Am. Ceram. Soc*, 52:253, 1969.

[40] N. Uchida and T. Ikeda. *Jap. J. Appl. Phys*, 6:1292, 1967.

[41] F. Kulcsar. *J. Am. Ceram. Soc*, 42:343, 1959.

[42] F. Kulcsar. *J. Am. Ceram. Soc*, 48:54, 1985.

[43] R. B. Atkin, R. L. Holman, and R. M. Fularth. *J. Am. Ceram. Soc*, 54:113, 1971.

[44] H. Banno and T. Tsunooka. *Jap. J. Appl. Phys*, 6:954, 1967.

[45] G. H. Haertling and C. E. Land. *Ferroelectrics*, 75:25, 1987.

[46] G. H. Haertling and C. E. Land. *J. Am. Ceram. Soc*, 54:1, 1971.

[47] G. H. Haertling. *J. Am. Ceram. Soc*, 54:303, 1970.

[48] G. H. Haertling and C. E. Land. *J. Am. Ceram. Soc*, 3:269, 1972.

[49] S.Aggarwal and R.Ramesh. *Annu.Rev.Mater.Sci*, 28:463, 1998.

[50] R.Thomas, S.Mochizuki, T.Mihara, and T.Ishida. *Mater.Sci and Eng. B,*, 95:36, 2002.

[51] G.Yi, Z.Wu, and M.Sayer. *J. Appl.Phys*, 64:2717, 1988.

[52] J.F.Wager. *Philos. Mag.A*, 67:897, 1993.

[53] L. E. Cross. *Ferroelectrics*, 76:241, 1987.

[54] S.Hirano, T.Yogo, K.Kikuta, K.Kato, W.Sakamoto, and S.Ogasahara. *Ceram.Trans*, 25:19, 1992.

[55] I. H. Pratt and S. Firestone. *J. Vac. Sci. Tech*, 8:256, 1971.

[56] S.Thakoor and A. P.Thakoor. *Appl. Opt.*, 34:3136, 1995.

[57] D.A.Barrow, T.E.Petroff, R.P.Tandon, and M.Sayer. *J.Appl.Phys*, 81:876, 1997.

[58] Q.F.Zhou, H.L.W.Chan, and C.L.Choy. *Thin Solid Films*, 375:95, 2000.

[59] Y.Ohya, T.Ito, and Y.Takahashi. *Jpn.J.Appl.Phys*, 33:5272, 1992.

[60] J.Junquera and P.Ghosez. *Nature*, 422:506, 2003.

[61] J.E.Spanier, A. M. Kolpak, J. J. Urban, I.Grinberg, L.Ouyang, W.S.Yun, A.M.Rappe, and H.Park. *Nano Lett.*, 6:735, 2006.

[62] Micron Technology, Inc., 8000, S. Federal Way, P.O. Box 6, Boise,. *Designing for High-Density DDR2 Memory*, 2005.

[63] K. Wasa, M. Kitabatake, and H. Adachi. *Thin Film Materials Technology*. Springer-Verlag, Germany, 2004.

[64] M. Ohring. *Materials Science of Thin Films: Deposition and Structure*. Academic Press, New York, 2001.

[65] L. I. Maissel and R. Glang (Eds). *Handbook of Thin Film Technology*. McGraw-Hill Inc, New York, 1970.

[66] D.L.Smith. *Thin Film Deposition*. Mc Graw Hill Inc, New York, 1995.

[67] F.L.Akkad, A.Punnose, and J.Prabu. *J.Appl.Phys A*, 71:157, 2000.

[68] B.Chapman. *Glow Discharge processess*. John Wiley and sons, 1990.

[69] B.D Cullity and S.R Stock. *Elements of x-ray diffraction*. Prentice Hall, London, 2001.

[70] V.S.Smentkowski. *Progress in Surface Science*, 64:1, 2000.

[71] R.Venkatesan and S.M.Green. *The Industrial Physicist*, 2:22, 1996.

[72] *Veeco Dektak 6M*, 2004.

[73] C.Kittel. *Introduction to solid state Physics*. Wiely Eastern Limtd, 1996.

[74] C.V.Raman and K.S.Krishna. *Nature*, 121:501, 1928.

[75] H. Richter, Z.P.Wang, and L.Ley. *Solid State Commun*, 39(625), 1981.

[76] D.K.Schroder. *Semiconductor material and device charecterisation*. Wiley Interscience, New York, 1998.

[77] P.E.J Flewit and R.K.Wild. *Physical methods for material characterization*. IOP publishing, Bristol, 2003.

[78] B.G.Streetman. *Solid state electronic devices*. Prentice hall of India private Ltd, Englewood cliffs, New York, 1995.

[79] J.Bardeen, F.J.Blatt, and L.H.Hall, editors. *Proce of Photoconductivity conf*, Atlantic city, 1954. J.Wiley and Sons.

[80] J.C.Manifacier, J.Gasiot, and J.P Fillard. *J. Phys. E: Sci. Instrum.*, 9:1002, 1976.

[81] P.Kubelka and F.Munk. *Zh.Tekh.Fiz*, 12:593, 1931.

[82] P. Kubelka. 38 (1948) 448. *J. Opt. Soc .Am*, 38:448, 1948.

[83] D.R.Vij. *Luminescence of solids*. Plenum Press, New York, 1998.

[84] M.Sheik-Bahae, A.A.Said, T.H.Wei, D.J.Hagan, and E.W.VanStryland. *IEEE J. Quantum Electron*, 26:760, 1990.

[85] *Operation manual of the RT66A from Radiant Technology, Version 2.2 (Albuquerque,NM).*

[86] Gary A Perterson, Jr, and J.R McNeil. *Thin Solid Films*, 220:87, 1992.

[87] M.H Yeh, K.S Liu, and I.N.Lin. *J.Mater.Res*, 9:2379, 1994.

[88] W.J.Lin, T.Y Tseng, Y.Z Wu, S.P Lin, S.L Tu, H.Chang, S.J.Yang, and I.N.Lin. *J.Mater.Sci:Materials in Electronics*, 7:409, 1996.

[89] O.Auciello, L.Mantese, J.Duarte, X.Chen, S.H.Rou, A.I.Kingon, A.F.Schreiner, and A.R.Krauss. *J.Appl.Phys*, 73:5197, 1993.

[90] X.Y Chen and Z.G Liu. *Appl Phys A*, 69:5523, 1999.

[91] D.Bao, Roland Scholz, Marine Alexe, and Dietrich Hesse. *J.Appl.Phys*, 101:54118, 2007.

[92] F.Cheng, H.F Wang, Q.Z Liu, Wenbin Wu, and X.G.Li. *Appl.Phys.Letts*, 90:82904, 2007.

[93] J.Wang, L.Y.Zhang, X.Yao, and J.K Li. *Ceramics International*, 30:1517, 2004.

[94] L.Zhang, M.Ichiki, J.Tsaur, Z.Wang, and R.Maeda. *Jpn.J.Appl.Phys*, 42:3986, 2003.

[95] D.P.Norton. *Materials Science and Eng.R*, 43:139, 2004.

[96] V.R.Plakar, S.C.Purandare, and R.Pinto. *J.Phys.D:Appl.Phys*, 32:R1, 1999.

[97] J.B.Goodenough. *J.Phys.Chem.Solids*, 6:287, 1958.

[98] P.M.Raccah and J.B.Goodenough. *J.Appl.Phys.*, 39:1209, 1968.

[99] R.Ramesh, H-Gilchrist, T.Sands, V.G.Keramidas, R.Haakenaasen, and D.K.Fork. *Appl.Phys.Lett.*, 63:3592, 1993.

[100] J.T.Cheung, P.E.D.Morgan, D.H.Lowndes, S-Y Zheng, and J.Breen. *Appl.Phys.Lett.*, 62:2045, 1993.

[101] R.Dat, D.J.Lichtenwalner, O.Auciello, and A.J.Kingon. *Appl.Phys.Lett.*, 64:2673, 1994.

[102] R.Ramesh, J.Lee, T.Sands, V.G.Keramidas, and O.Auciello. *Appl.Phys.Lett.*, 64:2511, 1994.

[103] Y.Furusawa and H.Doi. *Jpn.J.Appl.Phys.*, 38:6864, 1999.

[104] Y.F.Chen, L.Sun, T.Yu, J-X Chen, Y-Y Zhu, N-B Ming, X-Y Chen, and Z-G Liu. *Thin Solid Films*, 269:18, 1995.

[105] H.Han, J.Zhong, S.Kotru, P.Padmini, X.Y.Song, and R.K.Pandey. *Appl.Phys.Lett.*, 88:092902, 2006.

[106] R.W.Schwartz, M.T.Sebastian, and M.V.Raymond. *Mater.Res.Soc.Symp.Proc.*, 623:365, 2000.

[107] A.S Asha. *RF magnetron sputtered perovskite oxide electrodes for Ferroelectric RAM.* PhD thesis, Cochin University of Science and TEchnology, December 2007.

[108] Y.J. Yu, H.L.W.Chan, F.P.Wang, and L.C.Zhao. *Microelectron. eng*, 66:726, 2003.

[109] C.J.Peng and S.B.Krupanidhi. *J.Mather.Res.*, 10:708, 1995.

[110] E.Bouyssou, P.Leduc, G.Guegan, and R.Jerisian. *J. Phys. Conf. Ser.*, 10:317, 2005.

[111] X.S Wang, Y.J.Wang, J.Yin, and Z.G.Liu. *Scr Mather*, 46:783, 2002.

[112] D. Damjanovic. *Rep.Prog.Phys*, 61:1267, 1998.

[113] Im.O, Auciello, and S.K Streiffer. *Thin Solid Films*, 413:243, 2002.

[114] S.Agarwal, R. Manchanda, and G.L.Sharma. *Solid State Commun*, 119:681, 2001.

[115] C. L. Chen, H. H. Feng, Z. Zhan, A. Brazdeikis, Z. J. Huang, W. K. Chu, C.W. Chu, F. A. Miranda, F. W. Van Keuls, R. R. Romanofsky, and Y. Liou. *App Phys Lett*, 75:412, 1999.

[116] B. H. Park, Y. Gim, Y. Fan, Q. X. Jia, and P. Lu. *Appl Phys Lett*, 77:2587, 2000.

[117] C.I.Chen, J.Shen, S.Y.Chen, G.P.Luo, C.W.Chu, F.A.Miranda, F.W.VanKeuls, J.C.Jiang, and E.I.Meletis. *Appl Phys Lett*, 78:652, 2001.

[118] K. V. Saravanan, K. Sudheendran, M. G. Krishna, and K. C. James Raju. *J. Phys. D: Appl. Phys.*, 42:045401, 2009.

[119] D.Y Kim, S.E Moon, E.K Kim, S.J.Lee, J.J Choi, and H.E Kim. *Appl Phys Lett*, 82:1455, 2003.

[120] J.F Scott, A.Q Jiang, S.A.T Redfern, M. Zhang, and M. Dawer. *J Appl Phys*, 94:3333, 2003.

[121] B.Panda, A.Dhar, G.D Nigam, D. Bhattacharya, and S.K Ray. *Thin Solid Films*, 332:46, 1998.

[122] A.C Carter, W. Chang, S.W Kiechoefer, J.S Horwitz, and D.B Chrisey. *Appl Phys Lett*, 71:3353, 1997.

[123] R.Thielsch, K.Kaemmer, B.Holzapfel, and L.Schultz. *Thin solid films*, 301:203, 1997.

[124] F. Tcheliebou, H.S Ryu, C.K. Hong, W.S Park, and S.Baik. *Thin Solid Films*, 305:30, 1997.

[125] H.Rumpf. *Mater Sci Eng A*, 378:429, 2004.

[126] Asok Kumar, Sriraj.G.Madhavan, Venkataramanan Gurumurthy, Sathyaharish Jeedigunta, and Thomas Weller. *Materials Science and Engineering B*, 139:177, 2007.

[127] L. D. Rotter, M. D. Vaudin, J. E. Bonevich, D. L. Kaiser, and Soon O Park. *Thin Solid Films*, 368:41, 2000.

[128] S.Saha and S.B.Krupanidhi. *J Appl Phys*, 88:3506, 2000.

[129] Y.F. Kuo and T.Y. Tseng. *Materials Chemistry and Physics*, 61:244, 1999.

[130] K.V.Saravanana, K.Sudheendrana, M.G.Krishna, K.C.James Raju, and A.K. Bhatnagar. *Vacuum*, 81:307, 2006.

[131] T.Zhang, S.Li, B.Zhang, R.Pan, J.Jiang, and W.Huang. *Jpn.J.Appl.Phys.*, 44:8599, 2005.

[132] C.B.Samantary, A.Dhar, D.Bhattacharya, M.L.Mukherjee, and S.K.Ray. *J Mather Sci:Materials in Electronics*, 12:365, 2001.

[133] W.J.Lee, I. Park, G.E Jang, and H.G Kim. *Jpn.J Appl Phys*, 34:196, 1995.

[134] Z.Xu, M.Suzuki, and S.Yokoyama. *Jpn. J. Appl. Phys*, 44:8507, 2005.

[135] A.Hamerich, R.Wunderlich, and J. Muller. *J.Vac. Technol A*, 15:2873, 1994.

[136] J.M Grace, D.B McDonald, M.T Reiten, J.Olson, R.T Kampwirth, and K.E Gray. *J Vac Technol A*, 10:1600, 1992.

[137] J.C Tauc. *Optical Properties of Solids*. North Holland Amsterdam, 1972.

[138] G.Bauer. *Ann Phys*, 19:434, 1934.

[139] R.Jacobson. *Phys Thin Films*, 51:2873, 1975.

[140] W.L.Bragg and A.B.Pippard. *Acta Crystallogr*, 6:865, 1953.

[141] H.A.McLeod. *J Vac Sci Technol*, 4:418, 1986.

[142] J.A.Thornton. *J Vac Sci Technol*, 11:666, 1974.

[143] H.F Cheng. *J.Appl.Phys*, 79, 1996.

[144] X.H.Zhu, B.Guigues, E.Defa, C.Dubarry, and M. Ad. *J. Appl. Phys*, 105:44108, 2009.

[145] A.K.Tagantsev, V.O.Sherman, K.F.Astafiev, J.Venkatesh, and N.Setter. *J. Electroceram.*, 11:5, 2003.

[146] S.U Adikary and H.L.W Chan. *Thin Solid Films*, 424:70, 2003.

[147] O.Auciello, S.Saha, D.Y.Kaufman, S.K.Streiffer, W.Fan, B.Kabius, J.Im, and P.Baumann. *J. Electroceram.*, 12:119, 2004.

[148] M.W.Cole, W.D.Nothwang, J.D.Demaree, and S.Hirsch. *J. Appl. Phys*, 98:24507, 2005.

[149] K.P.Jayadevan and T.Y.Tseng. *J. Mater Sci.: Mater.electron*, 13:439, 2002.

[150] D.Roy and S. B. Krupanidhi. *Appl.Phys.Lett*, 62:1056, 1993.

[151] L.A Knaus, J.M.Pond, J.S.Horwitz, D.M.Chrisey, C.H.Mueller, and R.Treece. *Appl.Phys.Lett*, 69:25, 1996.

[152] E.J Tarna, E.A Hachfield, F.T Quinlan, J.S.Speck, and M.Eddy. *Appl.Phys.Lett*, 68:490, 1996.

[153] B.Panda, A.Roy, A.Dhar, and S.K.Ray. *J. Appl. Phys*, 101:64116, 2007.

[154] S.T Lee, N Fujimura, and T.Ito. *Jpn. J. Appl Phys*, 34:5168, 1995.

[155] W.J Kim, W.Chang, S.B.Qadri, J.M.Pond, S.W.Kirchoefer, J.S.Horwitz, and D.B. Chrisey. *Appl.Phys. A.:Mater.Sci.Process*, 70:313, 2000.

[156] H.Z Jim and J.Zhu. *J.Appl.Phys*, 92:4594, 2002.

[157] C.J.Peng and S.B.Krupanidhi. *Thin Solid Films*, 144:305, 1997.

[158] G.W.Dietz, M.Schumacher, R.Waser, S.K.Streiffer, C.Basceri, and A.I.Kingon. *J. Appl. Phys.*, 82:2359, 1997.

[159] V.E.Henrich, G.Dresselhaus, and R.J. Zeiger. *Phys. Rev. B*, 17:4908, 1988.

[160] L.Hafid, G.Godefroy, A. El Idrissi, and F.Michel-Calendini. *Solid State Commun*, 66:841, 1988.

[161] J.G. Simmons. *Phys. Rev*, 166:912, 1968.

[162] M.Sayer, A.Mansigh, A.K.Arora, and A.Lo. *Integrated ferroelectrics*, 1:129, 1992.

[163] A.S.Asha, M.K jayaraj, and M.T Sebastian. *J. Alloys Compd.*, 68:449, 2008.

[164] M.H.Yeh, K.S.Liu, and I.N.Lin. *J.mater.Res.*, 9:2379, 1994.

[165] M.Dawber, K.M.Rabe, and J.F.Scott. *Reviews of Modern Physics*, 77:1083, 2005.

[166] B.Nagaraj, T.Sawhney, S.Perusse, S.Aggarwal, R.Ramesh, V.S.Kaushik, S.Zafar, R.E.Jones, J.H.Lee, V. Balu, , and J. Lee. *J. Appl. Phys*, 74:3194, 1999.

[167] C.S.Hwang, B.T.Lee, C.S.Kang, J.W.Kim, K.H.Lee, H.J.Cho, H.Horii, W.D.Kim, S.I.Lee, Y.B.Roh, and M.Y.Lee. *J. Appl. Phys*, 83:3703, 1998.

[168] J.Zhou, L.Li, and Z.Gui. *Appl Phys Lett*, 76:1540, 2000.

[169] H.M Al-Allak, A.W. Brinkman, G.J Russell, and J Woods. *J Appl Phys*, 63:4530, 1988.

[170] C.B.Samantaray, M.L.Nanda Goswami, D.Bhattacharya, S.K.Roy, and H.N.Acharya. *Mater Lett*, 58:2299, 2004.

[171] S.Y. Kuo, C. S. Chen, T.Y.Tseng, S.C Chang, and W.F. Hsieh. *J Appl Phys*, 92:1868, 2002.

[172] D.Y.Kim, S.E.Moon, E.K.Kim, and S.J.Lee. *Appl Phys Lett*, 82:1455, 2003.

[173] J.F.Scott, A.Q.Jiang, S.A.T.Redfern, M.Zang, and M. Dawber. *J Appl Phys*, 94:3333, 2003.

[174] E.D.Mishina, N.E Sherstyuk, V.I. Stadnichuk, A.S.Sigov, V.M Mukhorotov, Y.I Golovoko, A.Ettenger, and Th.Rasing. *Appl Phys Lett*, 83:2402, 2003.

[175] P Shi, Xi Yao, L Zhang, X Wu, M Wang, and X Wan. *sol Stat Comm*, 134:589, 2005.

[176] S.W.Liu, J.Xu, D.Guzun, G.J.Salamo, C.L.Chen, Y.Lin, and Min Xiao. *Appl Phys B*, 82:443, 2006.

[177] A.Gedanken, R. Reisfelf, L.Somainski, Z.Zhong, Y.Koltypin, G.Panezer, M.Gaft, and H.Miniti. *Appl Phys Lett*, 77:945, 2000.

[178] M.J.Weber and R.F Schaufele. *Phys Rev A*, 138:1544, 1965.

[179] A.Patra, E.Sominska, S.Ramesh, Y.Koltypin, Z.Zong, H.Miniti, R.Reisfeld, and A.Gedanken. *J Phys Chem B*, 103:3361, 1999.

[180] N.J.Cockcroft and J.C.Wright. *Phys Rev B*, 45:9642, 1992.

[181] P. S. Pizani, E. R. Leite, F. M. Pontes, E. C. Paris, J. H. Rangel, E. J. H. Lee, E. Longo, P. Delega, and J. A. Varela. *App Phys Lett*, 77:824, 2000.

[182] F. M. Pontes, E. Longo, E. R. Leite, E. J. H. Lee, J. A. Varela, P. S. Pizani, C. E. M. Campos, F. Lanciotti, V. Mastellaro, and C. D. Pinheiro. *Mater. Chem. Phys*, 77:598, 2002.

[183] S.C Roy, M.C Bhatnagar, G.L Sharma, N. Karar, and H. Chander. *Jp. J. Appl Phys*, 44:34, 2005.

[184] Y.Wang. *Acc.Chem.Res*, 24:133, 1991.

[185] J. M. Ballesteros, R. Serna, J. Solis, C. N. Afonso, A. K. Petford-Long, D. H. Osborne, and R. F. Haglund Jr. *App Phys Lett*, 71:2445, 1997.

[186] L.W.Tutt and A.Kost. *Nature*, 356:225, 1992.

[187] J.F.Scott, C.A. Paz de Auraujo, B.M. Melnick, L.D. McMillan, and R.Zuleeg. *J. Appl. Phys.*, 70:382, 1991.

[188] R. Waser and M. Klee. *Integrated Ferroelectrics*, 2:23, 1992.

[189] P.C. Joshi and S.B. Krupanidhi. *Appl. Phys. Lett.*, 61:1525, 1992.

[190] P.C. Fazan. *Integrated Ferroelectrics*, 4:247, 1994.

[191] S. Yamamichi, T. Sakuma, K. Takemura, and Y. Miyasaka. *Jpn. J. Appl.Phys.*, 30:2193, 1991.

[192] K. Abe and S. Komatsu. *Jpn.J. Appl. Phys.*, 31:2985, 1992.

[193] X. Chen, A.I. Kingon, L. Mantese, O. Auciello, and K.Y. Hsieh. *Integrated Ferroelectrics*, 3:259, 1993.

[194] P.C. Joshi and S.B. Krupanidhi. *J. Appl. Phys.*, 73:7627, 1993.

[195] J.J. Lee, C.L. Thio, and S.B. Desu. *J. Appl. Phys.*, 78:5073, 1995.

[196] H. Hu and S.B. Krupanidhi. *J. Mater. Res.*, 9:1484, 1994.

.

Salutations to the guru and guru's sandals
Salutations to elders and their sandals
Salutations to the sandals of the teacher of perfection.
For I place this at their feets!